High-Q Multi-band Filters

by

Li Zhu

A thesis

presented to University of Waterloo

in fulfillment of the

thesis requirement for the degree of

Doctor of Philosophy

in

Electrical and Computer Engineering

Waterloo, Ontario, Canada, 2019

Examining Committee Membership

The following served on the Examining Committee for this thesis. The decision of the Examining Committee is by majority vote.

External Examiner   Xun Gong
                                                     Professor

Supervisor(s)   Raafat R. Mansour
                                                     Professor

                                                     Ming Yu
                                                     Professor

Internal Member   Safieddin Safavi-Naeini
                                                     Professor

Internal Member   Slim Boumaiza
                                                     Professor

Internal-external Member   Carolyn Liqing Ren
                                                     Professor

I hereby declare that I am the sole author of this thesis. This is a true copy of the thesis, including any required final revisions, as accepted by my examiners.

I understand that my thesis may be made electronically available to the public.

Abstract

Recent development of multifunctional communication systems capable of processing large amount of data has triggered the demand for novel payload configurations with advanced filtering functions. To increase the payload flexibility, a large number of multiplexer and filter networks with different frequency plans are usually employed for the transmitting downlink. Multi-band filters are the required function in many cases for minimizing integration complexity and reducing size and mass of space systems. The multi-band filters combine the frequency spectrums of non-contiguous channels before transmitting through antenna beams, and provide sufficient rejection to the frequency spectrums of the adjacent channels, thus maintaining a high signal-to-interference ratio especially in multi-beam frequency-reuse communication systems.

Traditional approaches to realize multi-band filters do not offer advantages in terms of size and mass reduction. Multi-mode resonators have the advantage of size reduction; however they are not often used in multi-band applications due to the challenges of operating the multiple modes in prescribed passbands simultaneously. The main research objective of this thesis is to investigate the feasibility of designing multi-band filters based on high-Q multi-mode resonators. Various multi-mode waveguide and dielectric resonators are explored to realize multi-band filters. The proposed multi-band filters do not require junctions and can achieve an equivalent performance with fewer cavities, thus significantly reducing the footprint when compared to traditional approaches. Furthermore, tunable multi-band filters with a constant absolute bandwidth and minimum performance degradation during the tuning process is investigated and developed.

A systematic design approach of designing multi-band filters based on multi-mode resonators is established in this work starting from the coupling-matrix synthesis of the multi-band network. Following that, dual-band filters based on elliptical and rectangular dual-mode resonators are proposed. The two passbands of the dual-band filter are carried by two independent cavity modes and realized by an inline direct-coupled configuration. The inline dual-band filter design can convert to a diplexer structure by modifying the output ports at the end-resonators. To improve near-band frequency selection of both channels, multiple configurations are proposed to realize quasi-elliptic dual-band filter functions.

The first quasi-elliptic design is based on a combination of dual-mode and single-mode rectangular resonators resulting in multiple transmission zeros and improved spurious response. The second structure is a side-coupled design based on dual-quadruplet configuration featuring a pair of transmission zeros on each of the passband and a very compact layout. Limitations of the quasi-elliptic design are investigated and modified structures have been proposed with improved RF performances.

Triple-band filters are realized by three types of high-Q cavity resonator structures. Each cavity resonator employs triple-modes with resonant frequencies associated with the three passbands. The first design was an elliptical waveguide triple-band filter with an in-line configuration. Each passband of the filter was controlled by a dedicated polarization and represented by an inline direct-coupled set of resonators. The second design was a rectangular-cavity triple-band filter with a folded configuration. The folded configuration overcomes a number of drawbacks from the elliptical in-line design including an improved tunability and ease of assembly. The last design was a triple-band filter design based on dielectric loaded cavity resonators. The unique dielectric resonator structure results in triple-band filters having a very compact size, high Q, and stable thermal response.

Further adding tuning capability to the multi-band filter can provide an additional degree of flexibility for the communication payload. A tunable multi-band filter with a constant absolute bandwidth is developed based on combline resonator and requiring only a single tuning element. The performance is demonstrated with an in-house-developed tuning station. It achieves a constant selectivity over a tuning range of 170 MHz and an unloaded Q better than 3000.

The novel filter configurations proposed in this thesis promise to be useful not only for satellite payload applications but also for a wide range of wireless base station applications.

Acknowledgements

TABLE OF CONTENTS

List of Figures

List of Tables

Chapter 1

Introduction

1.1   Motivation

The recent development of multifunctional communication systems capable of processing large amounts of data with high level of flexibility has triggered the demand for novel bandpass filtering structures with advanced filter functions [1]. Over the past few years, the multi-band filtering has become a required function in the communication payload for increasing the integration of complex filtering and multiplexing sub-systems [2]. For instance, the new generation of high throughput satellite (HTS) system requires a flexible allocation of the frequency bandwidth (BW) to beams. This can be achieved by employing a large number of multi-band filters to collect multiple channels that are non-continuous and transmit them to the designated geographical regions. Figure 1.1.1 illustrates an example where two spot beams, each with two non-continuous frequency bands are transmitted to different areas on the ground based on the demographical requirement. The dual-band filtering configurations collect two non-adjacent passbands for the designated spot beam while rejecting the passbands from other spot beams. Similarly in wireless system as shown in Figure 1.1.2, multi-band input/output filters can cooperate with multi-band low noise amplifiers and power amplifiers, receiving and transmitting signals of multiple wireless carries through a single antenna. Such simplified system architectures enable the transponder design with increased number of channels thus improving the system efficiency.

To cope with high power requirement while maintaining low insertion loss (*IL*), the cavity-based filters are considered the optimum solution for satellite and wireless base-station applications. Dual-band cavity filters have been realized with different technologies such as combline [3], dielectric [4], and waveguide structures [5]-[6]. However the realization of the triple-band (or more) filter has been limited to planar or multi-layer structures [7]-[9]. This is attributed to the challenge of collecting and
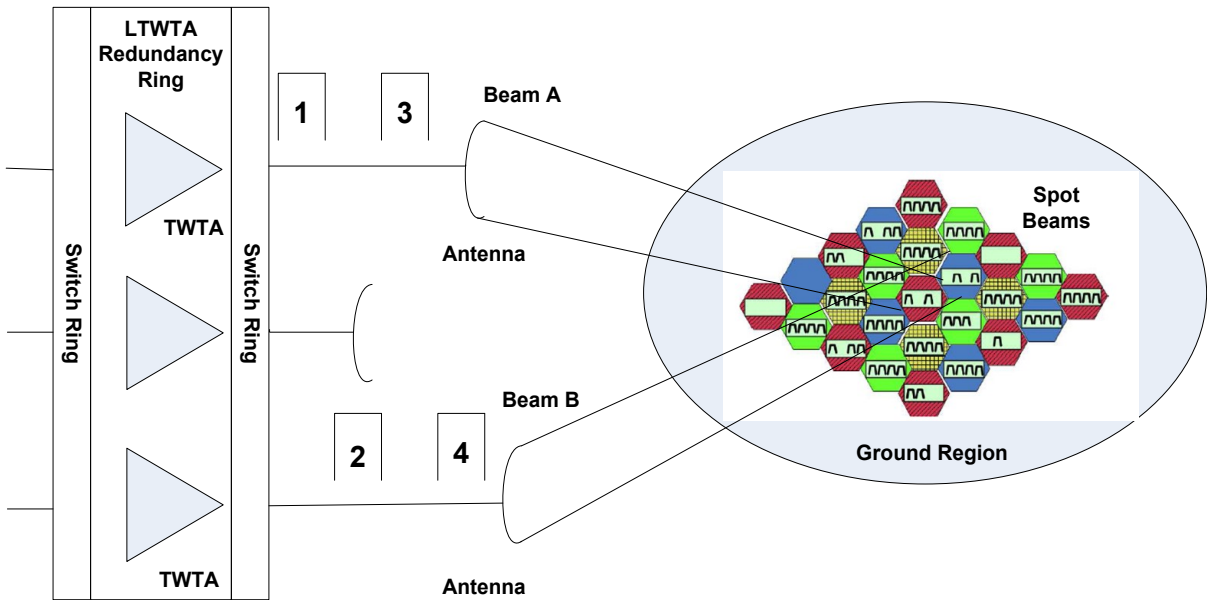
Figure 1.1.1: Multiple bandwidths distributed by multiple spot beams in HTS system.
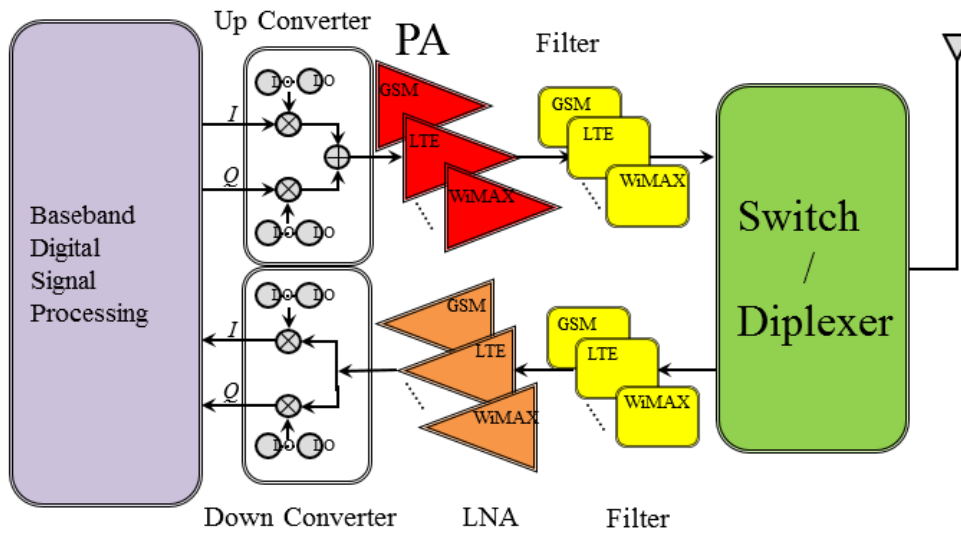
Figure 1.1.2: Multiple bandwidths carrying multiple carriers in wireless system.

controlling three distinct signal paths when dealing with cavity resonators.

In general, there are four potential approaches to realize a multi-band filter in a cavity structure:

1) Implementing the conventional approach, which can be realized either by using channel-dropping components (e.g., circulators) connecting multiple classical single-band filters as shown in Figure 1.1.3 (a) or by using a multiplexer concept as shown in Figure 1.1.3 (b). In both configurations, the signal is channelized and then combined at the output. This approach is bulky, as it requires the use of two combining junctions and one physical filter for each band.

(a)   (b)
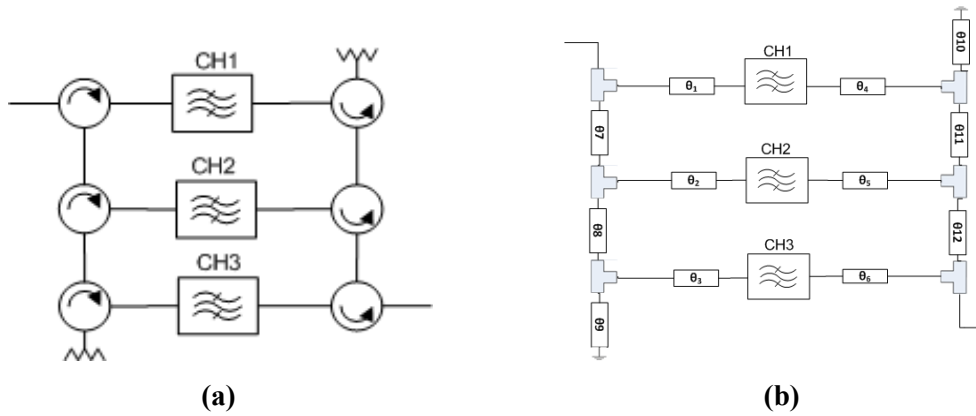
Figure 1.1.3: (a) Channel-dropping multi-band filter, and (b) Dual-manifold multi-band filter.

2) Cascading a wide-band bandpass filter with a number of narrow-band bandstop filters as shown in Figure 1.1.4. While this configuration has the advantage of modularity and simplicity of design, it is limited to the applications of narrow-passband separations between channels. The challenge is to maintain good return loss (*RL*) on both low and high passbands when having a wide stopband between the channels.
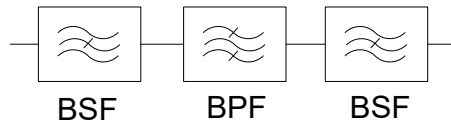
Figure 1.1.4: Multi-band filter realized by cascading bandpass and bandstop filters.

3) Creating multiple in-band transmission zeros in a high-order bandpass filter to split single band to multiple bands. The channel filter *BW* and passband separations are controlled by the position of transmission zeros, which in turn are controlled by the choice of the coupling values between the filter resonators, as shown in Figure 1.1.5. The coupling matrix for such multi-band filter designs are generated through synthesis methods reported in [3] and [6]. The topology is equivalent to combining multiple single-band lower-order filters to construct a multiple-band feature, employing the same number of resonators as using multiple single-band filters. Therefore the size saving in comparison with the conventional approaches shown in Figure1.1.3 and Figure 1.1.4 is not significant. In addition, this method is not suitable for the cases of wide frequency separations between channels because certain coupling values tend to be too large to be realized physically.

(a)   (b)
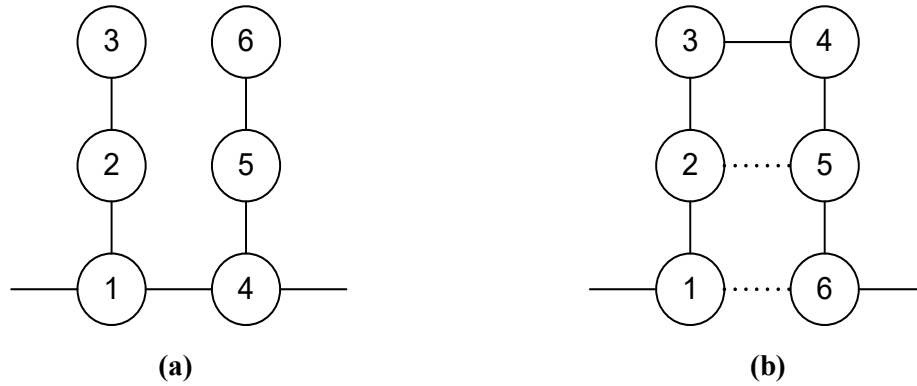
Figure 1.1.5: Multi-band filter realization by inserting in-band transmission zeros (a) bandstop resonator method, and (b) cross-coupling method.

4) The use of multi-mode resonators while controlling multiple dominant resonant modes to coincide with the center frequencies (*CF*) of the designated passbands. In Figure 1.1.6, the multiple paths of signals are carried by the corresponding designated modes and the channel paths are considered as non-interacting. A clear advantage of this approach is a dramatic saving in footprint and volume while not sacrificing the quality factor (*Q*). Since the coupling values in this case only relate to the channel *BW* instead of the overall *BW*, this method is capable to support much wider frequency separations between channels. The challenge is to properly place resonators and irises so that appropriate coupling in the structure can be established. Another challenge of this configuration is to realize subscribed transmission zeros for each passband. This is due to the complicated resonant mode distribution in the multi-mode

resonator, as well as how to dedicatedly realize and control the multiple sequential/cross coupling between resonators. The multi-band filters developed in this thesis will be all using this configuration which provides the highest degree of size saving while not sacrificing RF performances. A potential limitation of this method is when the channel passbands are closer, the interaction between the designated modes will increase, resulting undesired stray-coupling in the structure. Therefore this configuration is not ideal for the circumstances where narrow frequency separations are required between the passbands (e.g., less than one *BW*).
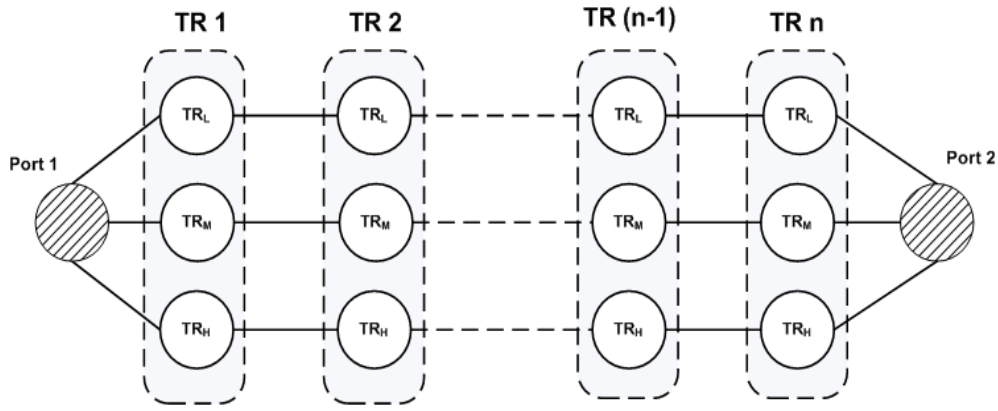
Figure 1.1.6: Multi-band filter realization by multi-mode resonator.

In addition to multi-band filters, tunable filters are also in great demand for front-end transceivers in a wide range of communication systems, from software-defined radios to reconfigurable satellite payloads. An ideal software-defined radio front end has a wide instantaneous *BW* to cover a broad range of radio system protocols and standards. This requires fast analog-to-digital convertors with high dynamic range and resolution. A tunable filter could be a premium solution [10]-[11]. In the meantime, flexible payloads capable of supporting more beams and transponders (thus having longer lifetimes) could be included in the system. The cost per satellite would be dramatically reduced because the same payload design could meet the requirements of different satellites.

To realize a flexible payload, a known approach is to employ multiple input multiplexer (IMUX) and output multiplexer (OMUX) units with different frequency plans. Extra RF switching network is required for the frequency change, resulting in extra component costs and increased mass and volume

of the satellite. A tunable filter is an alternative approach for adjusting the frequency plan of the satellite as required. In the past, this approach was considered impractical due to the significantly increased mass and volume, along with the tuning technologies and reduced reliability of the satellite. As the number of satellite beams and the output power of the traveling-wave tube continue to increase, multiport amplifiers [12] have become available for servicing multiple beams, with low-power filters defining the frequency plan of the satellite.

The generic architecture of a communication payload with tunable low-power filters is shown in Figure 1.1.7. In this configuration, the uplink beams are routed to the channel elements but the spectral filtering for the channel now occurs in the tunable channel rather than in the IMUX and OMUX, as previously mentioned. Each instance of a transponder is handled by one channel. If the *CF* and *BW* of the filter can be tuned, each channel can support any transponder need. Also, since each tunable filter is now associated with the channel amplifiers (which are already configured with redundancy, due to the failure probability of active circuits), the failure of a tunable filter does not result in a loss of capability, since a redundant channel and filter can be connected. In conventional architecture with multiple filters, the capacity would be reduced if one channel of a filter fails.

A critical feature for tunable filters is consistent selectivity over the entire tuning range while operating in a flexible satellite payload. Consistent selectivity is important due to the expensive frequency spectrum of any satellite system. Several technologies for making tunable filters have been reported in the literature and industry, such as planar tunable filters that employ solid-state and MEMS varactors [13]-[16],[26]-[48]. These have been around for several years but suffer from poor selectivity and transmission response variations over the tuning range. The switched filter bank offers discrete flexibility but suffers from large mass and size. Yttrium iron garnet filters offer a high unloaded Q, but the alignment of the magnetic field must be uniform for all yttrium iron garnet resonators in a multistage filter [17], [49]-[51]. This poses a major limitation to obtaining high-order filters with good overall performance. Mechanically tunable waveguide filters, on the other hand, offer high unloaded Q and high power handling capabilities [52]-[59]. The simplicity and low cost of the mechanically tuned implementation are well suited for high throughput satellites using spot beam technology.
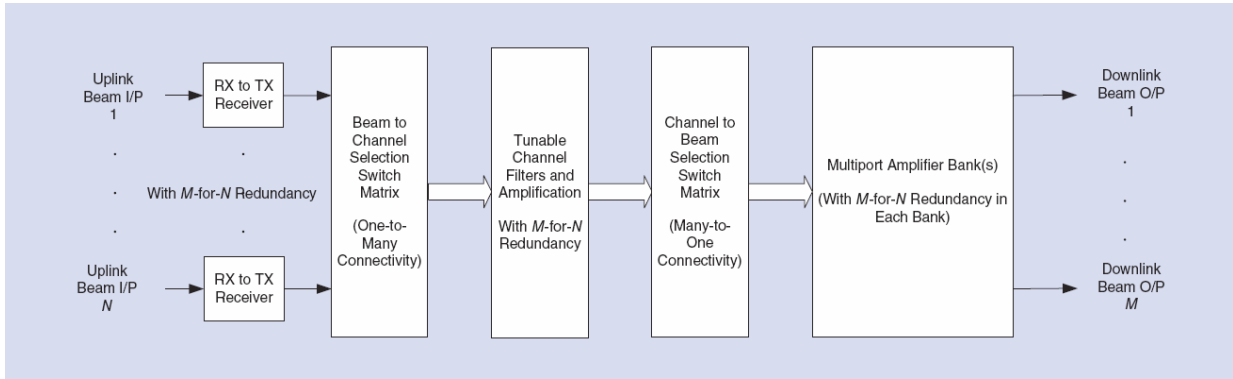
Figure 1.1.7: A generic communication satellite payload block diagram using tunable filters [23].

1.2 Objectives

This prime objective of this thesis is to develop advanced but practical configurations to realize multi-band filtering function, and to demonstrate the feasibility of realizing compact multi-band high–Q filters in waveguide and dielectric resonator realizations. In specific, the following research topics are investigated in this thesis:

- **Develop high Q multi-band filters in waveguide form.**

  Multi-mode waveguide resonators, which feature high Q along with a compact layout, will be examined to realize a multi-band filtering function with industry-standard RF performance.

- **Develop high Q multi-band filters in dielectric form.**

  High permittivity dielectric loaded resonator, which dramatically shrink the layout from the waveguide implementation, will be examined to realize a multi-band filtering function with industry-standard RF performance.

- **Develop techniques to realize advanced filter function for the multi-band filters**

  Different methodologies to realize finite transmission zeros beside each passband will be examined to improve the frequency selectivity of the multi-band filter.

- **Investigate potential use of multi-band filters in multiplexer applications.**

  Multiplexers based on multi-band filters/resonators do not require a manifold and thus effectively reduce their footprint. The side-effect of this approach is decreased channel-to-channel isolation, which will be investigated to find a solution.

- **Develop tunable or reconfigurable multi-band filters.**

  A tunable or reconfigurable multi-band filter is a solution for the advanced satellite flexible payload. Mechanical tuning circuits will be studied to be employed into multi-band filters. Typically, filter RF performances gradually degrade over the tuning range. Technologies to maintain the *RL* and *BW* during tuning will be explored in this project.

1.3　Thesis Outlines

Following the motivation and objectives presented in the previous sections, Chapter 2 reviews the literature on multi-band cavity filters, as well as different methods and technologies of tunable filters. Chapter 3 presents a generic coupling matrix model synthesis methodology for the multi-band filter using multi-mode resonators. In Chapter 4, waveguide dual-band filters and diplexers are introduced. In Chapter 5, methods to realize quasi-elliptic filter function of the waveguide dual-band filter are introduced. In Chapter 6, waveguide triple-band filters are presented. In Chapter 7, dielectric triple-band filters are presented. Chapter 8 introduces tunable multi-band filter. The conclusion and plans for future research are presented in Chapter 9.

Chapter 2

Literature Review

This chapter examines the literature on multi-band filter technologies and tunable filter technologies. Various multi-band filters have been introduced in recent years. The survey in this chapter will more focus on the realizations of the cavity-based multiple-band filters.

2.1 Multiple Band filter

As briefing introduced in the Chapter 1, there are four major technologies to realize multi-passband responses, which are introduced in the following sub-sections.

2.1.1 Channel dropping / Manifold coupled

The most conventional approach of realizing a multi-band filter is to connect single-band filters with circulators or other channel dropping element (e.g. command directional filter, hybrid…). In Figure 2.1.1.1, three single-band 10-pole dual-mode filters are connected back to back by three pairs of waveguide circulators. An outstanding advantage of this configuration is its amenability to module integration and ease of design and assembly as a result of the directional property of the circulators. There is no limit of the number of channels, and the design difficulty does not accumulate with the increase of the channels. However the price is the extra insertion loss, footprint and cost from the circulators and other associated hardware. An N-channel multi-band filter would require $2N$ of circulators (or other channel dropping elements) for this configuration.

Another conventional approach is to use a pair of manifolds to connect multiple single-band channel filters [21]. As shown in Figure 2.1.1.2, three 6-pole dual-mode filters are connected back to back by two E-plane manifolds. The layout is relatively more compact compared to the circulator channel

dropped approach. This configuration is also capable of providing optimum RF performance in terms of *IL* and *GD* responses. However the design process is more complicated since all the channels are presented simultaneously thus interacting each other. Moreover, each channel (plus junction) must have the same length, and input/output waveguide ports must have the same orientation. Therefore the design difficulty will accumulate with the increase of the channels although there is no limit of the number of channels to be connected with manifolds.

In general, both approaches support any number of channels but pay the price of increased footprint, mass and cost.

(a)   (b)
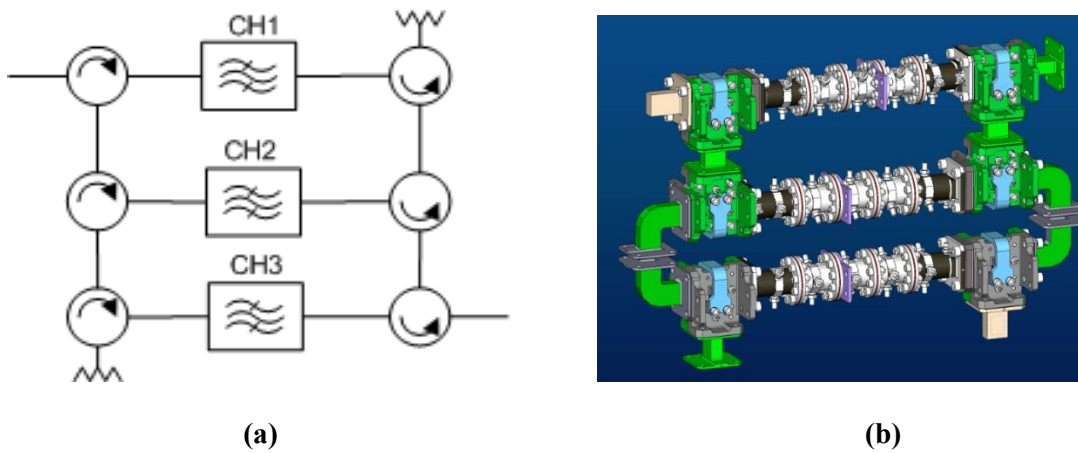
Figure 2.1.1.1: Conventional circulator coupled dual-band filter realization: (a) block diagram and (b) waveguide component realization.

(a)   (b)
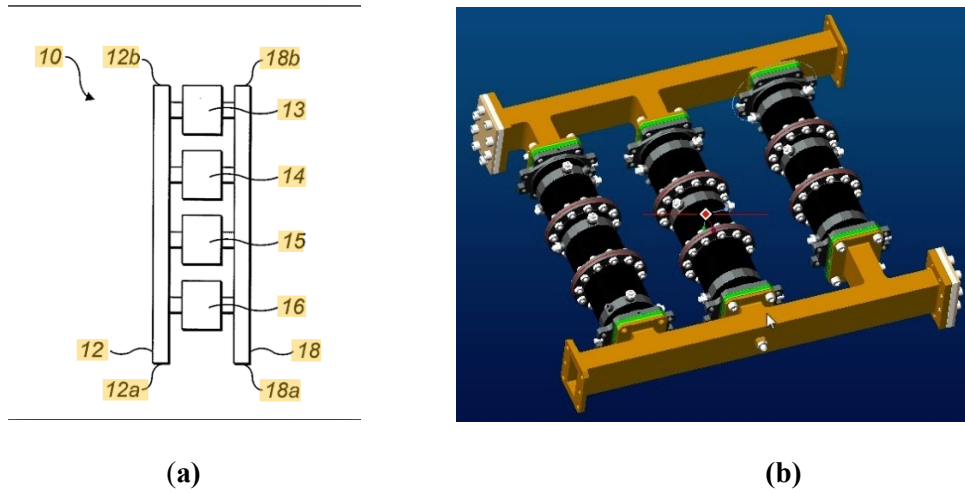
Figure 2.1.1.2: Conventional junction coupled triple-band filter realization: (a) block diagram [21] and (b) H-plane filter model

2.1.2 Cascaded structure of Bandpass and Bandstop filters

A multi-passband response can be achieved by combining a broadband bandpass filter and multiple bandstop filters. The bandpass and bandstop filters can be synthesized and designed separately, then cascaded to fulfill the requirement of multi-passband characteristics. The electrical phase among the filters needs to be optimized to achieve the optimum filtering performances of the multiple passbands. Similar to the circulator-coupled configuration, this approach also provides amenability to a modular concept.

An example of a dual-band filter response is shown in Figure 2.1.2.1 [20]. Figure 2.1.2.2 illustrates a dual-band filter consisting of a bandstop filter and a bandpass filter. The bandstop filter is implemented by using a coupled-serial-shunted line structure, while the bandpass filter is constructed by using a serial-shunted line configuration. The bandwidth of each passband of the dual-band filter is controllable by adjusting the responses of both the bandpass filter and the bandstop filter. The measurement results are compared by simulations, as shown in Figure 2.1.2.3.

This approach also results in increased footprint, mass and cost due to the employment of multiple individual filters.

11

(a)   **(b)**   **(c)**
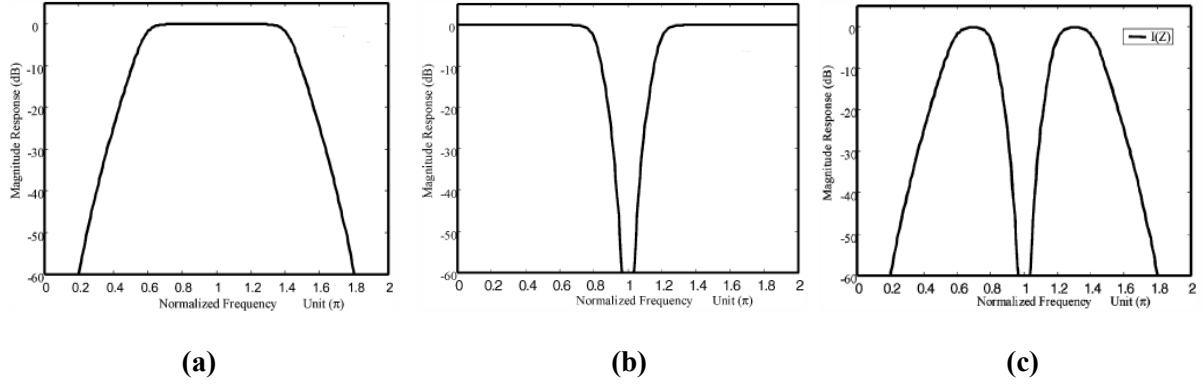
Figure 2.1.2.1: (a) bandpass response, (b) bandstop response, and (c) dual-band response [20]
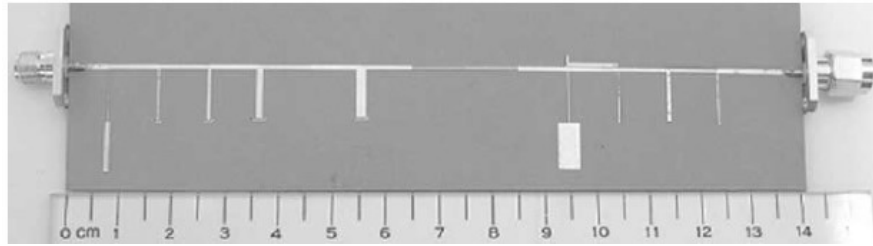
Figure 2.1.2.2: The fabricated dual-band filter [20].
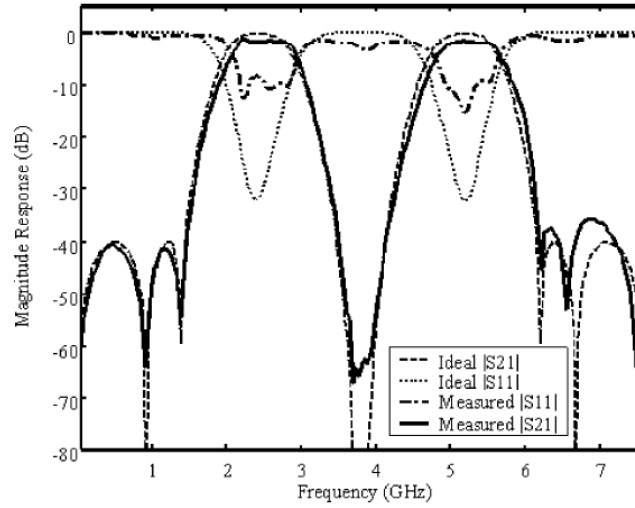
Figure 2.1.2.3: Measured and simulated S-parameters of the dual-band filter [20]

12

2.1.3   Transmission zeros inside the passband

A multi-passband response can be generated by adding transmission zeros inside a single passband. In most cases, the transmission zeros are produced either by cross-coupling or bandstop resonators.

For topologies with cross-coupling, a single wideband filter whose bandwidth covers the entire bandwidth of the multi-passband filter is first synthesized as the initial filter. The numerator and denominator of its characteristic function are then optimized to determine the prototype function and the locations of the reflection and transmission zeros of the multi-band filter. An alternative way to apply cross-coupling topology into a multi-band filter is to separately synthesize the characteristic function of each multi-individual filter, after which a generalized coupling matrix of the multi-band filter can be extracted by optimization. The design parameters of coupling coefficients, resonant frequencies, and external quality factors can then be obtained by de-normalizing the generalized coupling matrix [3].

Figure 2.1.3.1 (a) illustrates the topology of a 12-pole dual-band design example with cross-coupled resonators. Such a configuration is realized by a combline filter design, as shown in Figure 2.1.3.1 (b). The four transmission zeros generated by the negative cross-coupling M_{14} and M_{912} are uniformly displaced in the stopband. The attenuation of the inner stopband can easily be controlled by changing the position of the transmission zeros. Figures 2.1.3.2 (a) and (b) show two cases of normalized responses with different locations of transmission zeros. Another practical way to implement cross-coupled resonator is with cylindrical dual-mode cavities [6]. The inline architecture connecting multiple dual-mode cavities has the convenience of realizing both positive and negative cross-couplings. An 11-pole, 4-transmission zero, dual-band filter example and its performances are shown in Figure 2.1.3.3.

(a)   (b)
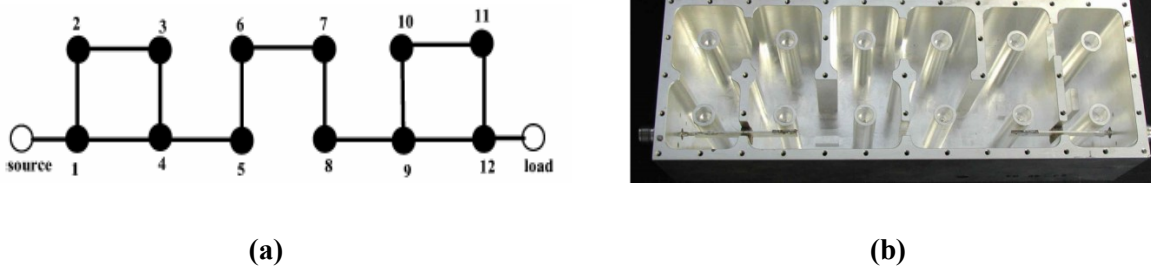
Figure 2.1.3.1: (a) Topology and (b) realization of the dual-band filter with cross coupling [3]
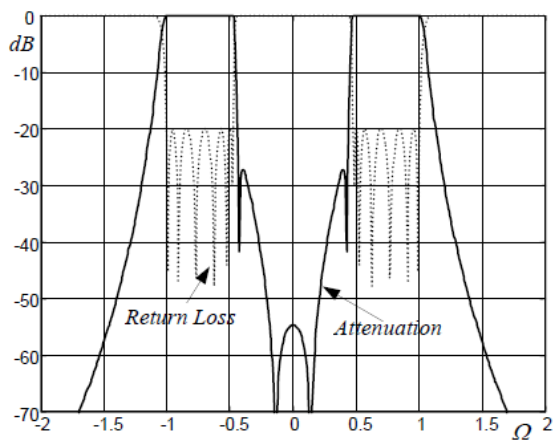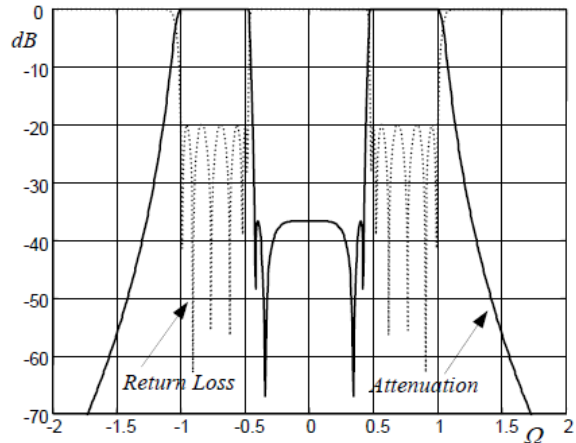
(a)   (b)

Figure 2.1.3.2: Dual-band prototype response (Ω domain) with (a) un-equirippled stopband, and (b) equirippled stopband [3].
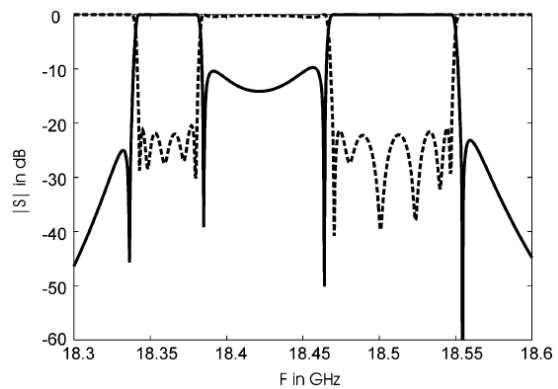
(a)   (b)

Figure 2.1.3.3:   Realized 11-pole 4-zero dual-band filter with dual-mode cavities, and (b) Simulated S-parameters [3].

14

The topology with transmission zeros generated by bandstop resonators can be analytically synthesized from the generalized low-pass prototype with Chebyshev or quasi-elliptic responses [9] [22]. The design parameters of coupling coefficients, external quality factor, and resonant frequencies can then be obtained. In this topology, the bandstop resonators are properly coupled to the bandpass resonator, which comprises the inverter-coupled resonator section. This section can be used as the basic unit for the dual-passband and multi-passband filters, in which every band has the same in-band and out-of-band responses.

Figure 2.1.3.4 shows the topologies of inverter-coupled resonator sections consisting of one bandpass resonator and one or two bandstop resonators. The bandstop resonators are coupled to the bandpass resonator through the admittance inverters in order to achieve dual- and triple-passband filtering responses. Figure 2.1.3.5 shows the transmission responses of the inverter-coupled resonator sections for the dual- and triple-passband filters. The frequency is normalized to that of the transmission zero for the dual-passband filter, while the frequency is normalized to that of the middle reflection zero for the triple-passband filter. These two types of sections can be used, respectively, as basic building blocks for the construction of dual- and triple-passband filters.

(a) (b)
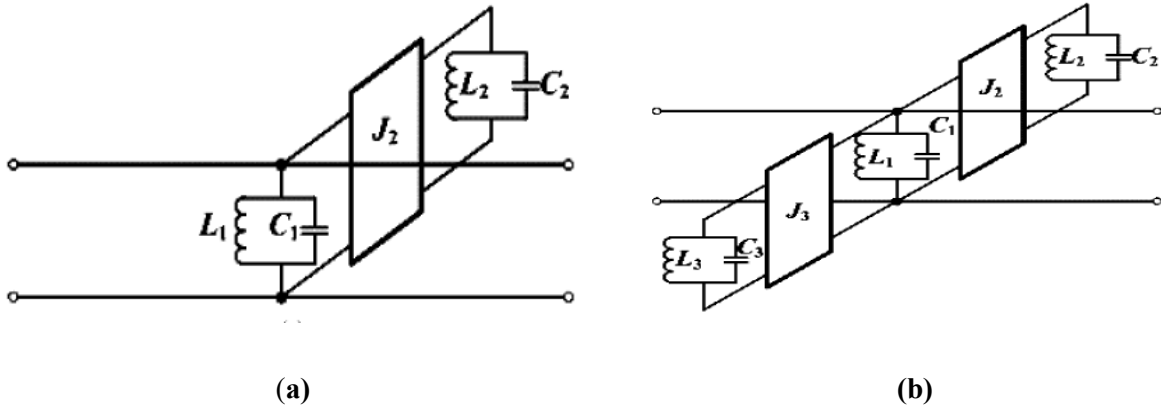
Figure 2.1.3.4: Topologies of inverter coupled resonator sections for: (a) dual- and (b) triple-band filter [9].
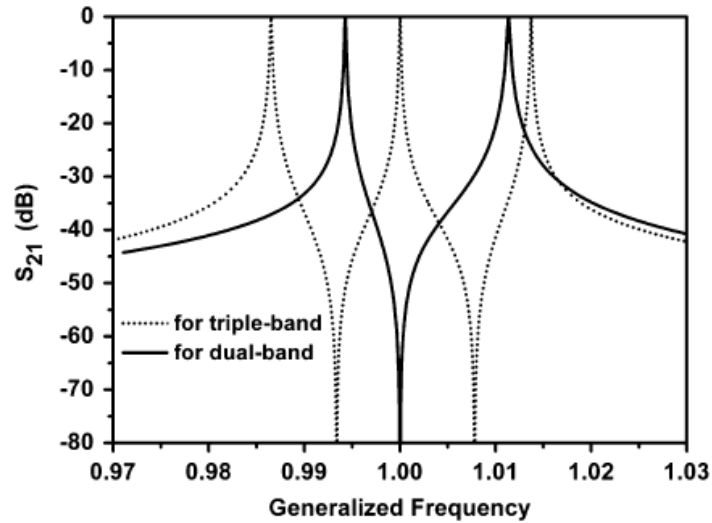
Figure 2.1.3.5: Transmission responses of the inverter coupled resonator sections for dual-band and triple-band filters [9].

In [9], the inverter coupled resonator is realized by a substrate-integrated waveguide that features low-cost and high-integration capabilities. Figure 2.1.3.6 (a) shows a geometrical structure of the dual-passband substrate-integrated waveguide filter with a Chebyshev response. A substrate-integrated waveguide cavity bandstop resonator is coupled with a substrate-integrated waveguide cavity bandpass resonator through a post-wall iris in the common post wall, which consists of the inverter-coupled resonator section. Both bandpass and bandstop resonators operate in fundamental TE_{101} mode. The couplings between two substrate-integrated waveguide cavity bandpass resonators are also realized by the post-wall iris in the common post wall. The first/last substrate integrated waveguide cavity bandpass resonators are directly excited by 50-ohm microstrip lines with coupling slots. The measurement and simulation responses of the dual-band filter are shown in Figure 2.1.3.6 (b). Similarly, a triple-band substrate-integrated waveguide filter is shown in Figure 2.1.3.7 (a). Two substrate-integrated waveguide bandstop resonators are coupled to a substrate-integrated waveguide bandpass resonator by the post-wall irises in the common walls. The measurement and simulation responses of the triple-band filters are shown in Figure 2.1.3.7 (b).

16
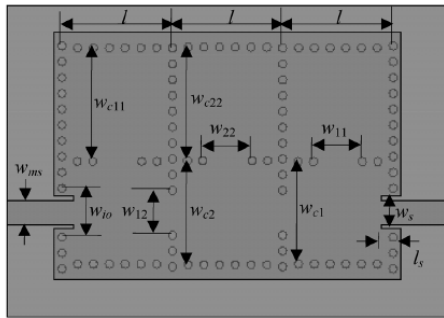
Symbol	Value (mm)	Symbol	Value (mm)
w_{ms}	1.55	w_{c22}	7.19
w_s	2.07	w_{12}	2.82
w_{io}	3.1	w_{11}	3.11
w_{c1}	6.48	w_{22}	3.14
w_{c2}	6.57	l	7
w_{c11}	7.19	l_s	1.22
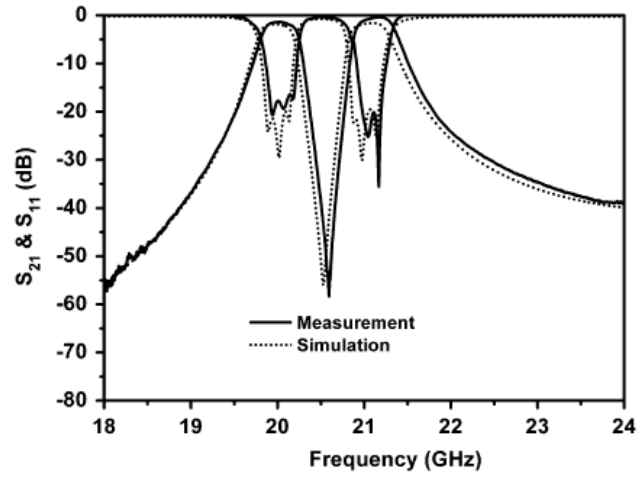
(a)   (b)

Figure 2.1.3.6: (a) SIW realization of the dual-band filter, and (b) measurement and simulation responses [9].
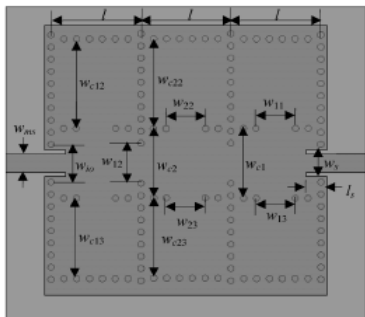
Symbol	Value (mm)	Symbol	Value (mm)
w_{ms}	1.55	w_{c23}	6.59
w_s	2.15	w_{12}	3.31
w_{io}	3.1	w_{11}	3.09
w_{c1}	5.74	w_{22}	3.08
w_{c2}	5.7	w_{13}	3.03
w_{c12}	7.35	w_{23}	3.02
w_{c22}	7.38	l	7.0
w_{c13}	6.61	l_s	1.64
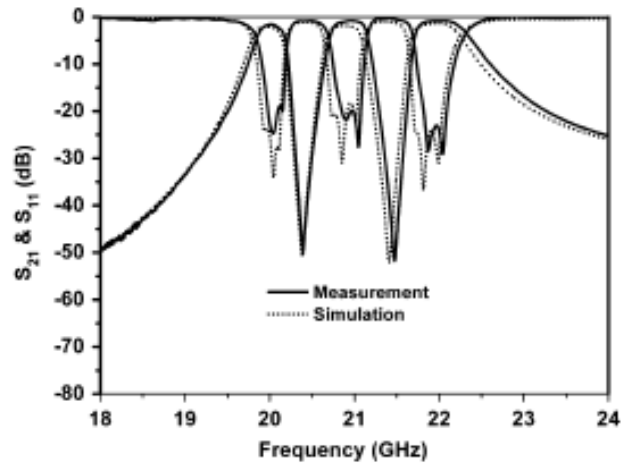
(a)   (b)

Figure 2.1.3.7: (a) SIW realization of the triple-band filter, and (b) measurement and simulation responses [9].

17

In [3], the inverter-coupled resonator section is realized by the combline structure working in quasi-TEM mode. Note that the resonant frequency is achieved by a combination of the length of the inner conductor, the cavity dimension, and tuning screws. The positive couplings are realized by the common wall of the adjacent cavities, and the input and output couplings are obtained with a tap in the inner conductor of the cavity. The layout and RF responses are shown in Figure 2.1.3.8.

(a)   (b)
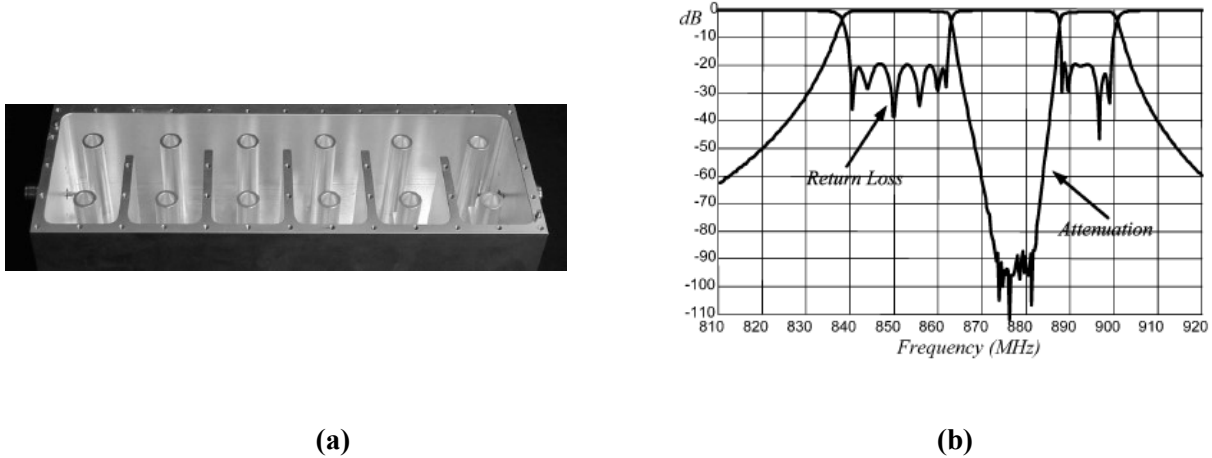
Figure 2.1.3.8: (a) Combline dual-band filter, and (b) measurement responses [3].

2.1.4   Multi-mode resonators

Multi-mode resonators are used for designing multi-passband filters when their dominant resonances coincide with the *CF*s of multiple designated passbands. A clear advantage of this approach is a dramatic savings in footprint and volume while not sacrificing the quality factor. The challenge is to properly place resonators and the associated coupling structure so that appropriate coupling in the filter can be established. This topology can be analytically synthesized, and an optimization scheme is required to design these filters. A potential limitation of this method is when the channel passbands are closer, the interaction between the three modes will increase, resulting undesired stray-coupling in the structure. Therefore such a configuration is not preferable to the circumstances where the guard-band between the passbands are narrow (e.g., less than one BW). Another challenge of this configuration is to realize cross-coupling for each passband due to the complicated self- and sequential- coupling mechanisms in or between resonators.

18

In [23], a composite resonator consisting of three split-ring resonators is designed as the basic block of the triple-band filter. Figure 2.1.4.1 shows a fabricated 6-pole triple-band filter and its S-parameters. The split ring resonators are asynchronously tuned, i.e., with different self-resonant frequencies, to meet filter specifications.

(a)   (b)
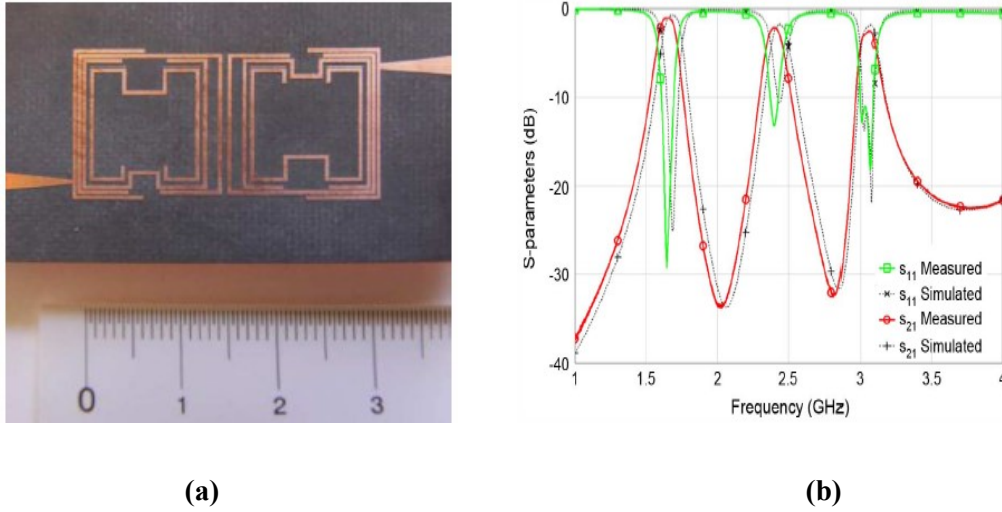
Figure 2.1.4.1: (a) Photograph of manufactured filter and (b) Simulated and measured Responses [23]

A dual-band dielectric resonator constructed from high-K ceramic substrate is presented in [4]. The dual-band dielectric resonator shown in Figure 2.1.4.2 (a) is employed to implement dual-band filters. The two rectangular slots through the dielectric material are intended to shift the spurious mode to a higher frequency. The mode distribution is listed in Figure 2.1.4.2 (b), showing a spurious-free window of about 800 MHz. The center frequencies and bandwidths of the first and second passbands can be controlled independently. Figures 2.1.4.3 and 2.1.4.4 illustrate the realization of the inter-resonator coupling and external coupling of the dual-band filter. Both filters are compact in size with a great simplicity in assembly and integration. They also offer high Q in comparison with microstrip dual-band filters. The dual-band filter layout and measured S-parameters are shown in Figure 2.1.4.5.
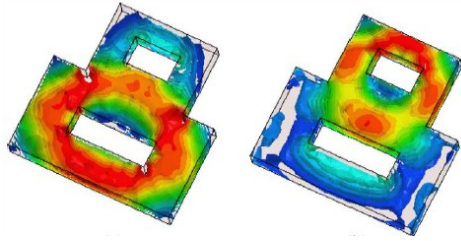
	Mode 1	Mode 2	Mode 3	Mode 4
Frequency (GHz)	5.00	5.60	6.39	6.40

(a)   **(b)**

Figure 2.1.4.2:   (a) Electric-field distribution of the first and second mode and (b) resonant frequencies of the dual-band resonator [4]
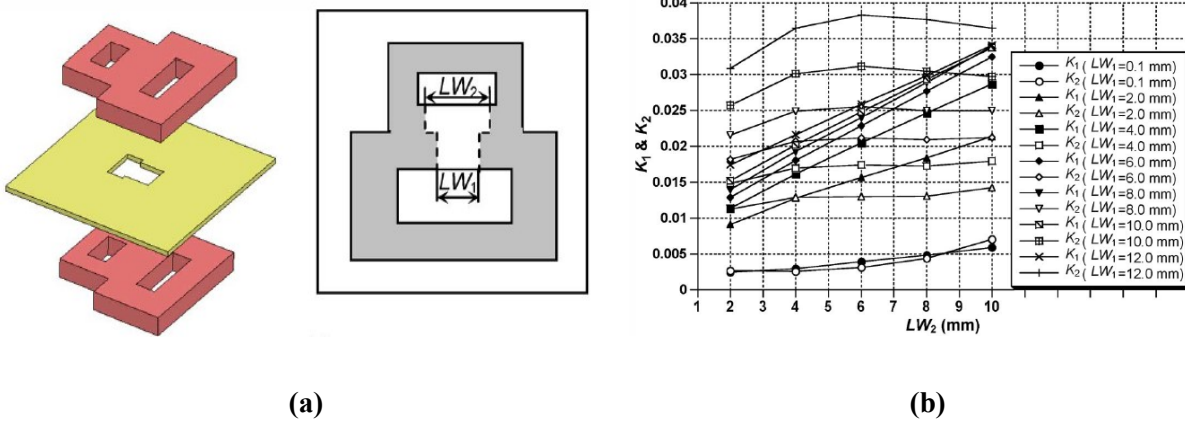
(a)   **(b)**

Figure 2.1.4.3:   (a) Inter-resonator coupling structure with the open windows at the center of the resonator and (b) Corresponding coupling coefficient of the first and second passband [4].

20
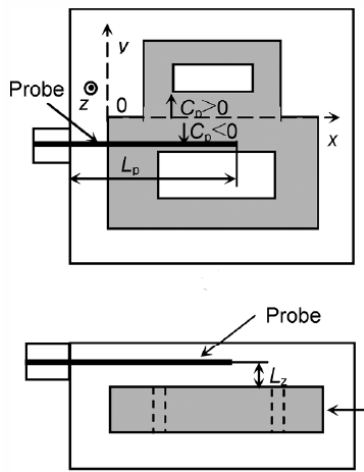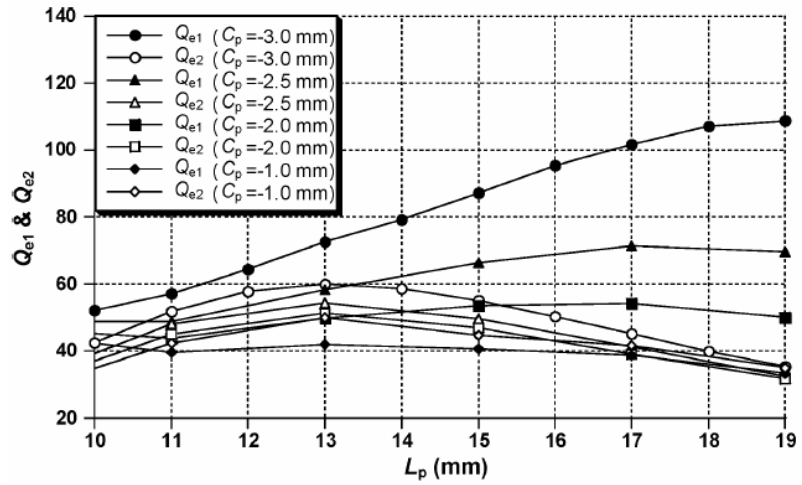
(a)   **(b)**

Figure 2.1.4.4: **(a) External coupling structure with the open windows at the center of the resonator and (b) Corresponding coupling coefficient of the first and second passband [4].**
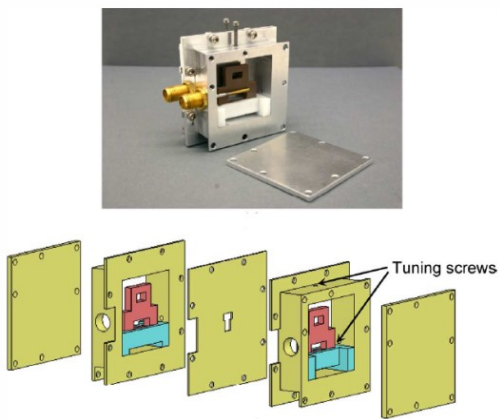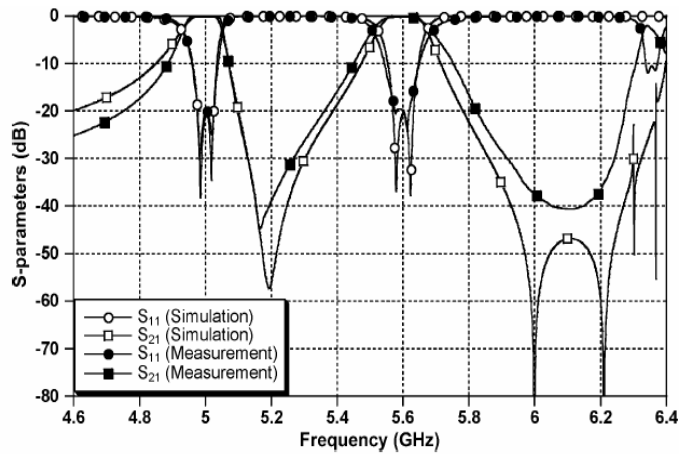
(a)   **(b)**

Figure 2.1.4.5: **(a) Photograph and assembly of the dual-band filter and (b) measured and simulated responses [4].**

21

Dual-band filter structures are also implemented by waveguide structures. In [5], dual-band filters are realized by rectangular dual-mode resonators. Each passband is controlled by a dedicated polarization inside the dual-mode resonator in order to reduce the sensitivity of the filter. By switching the orientations of the feeding waveguides between in-parallel and in-perpendicular, a transmission zero is generated between the two passbands. The layout and S-parameters are shown in Figure 2.1.4.6.

<div align="center">(a)   (b)</div>
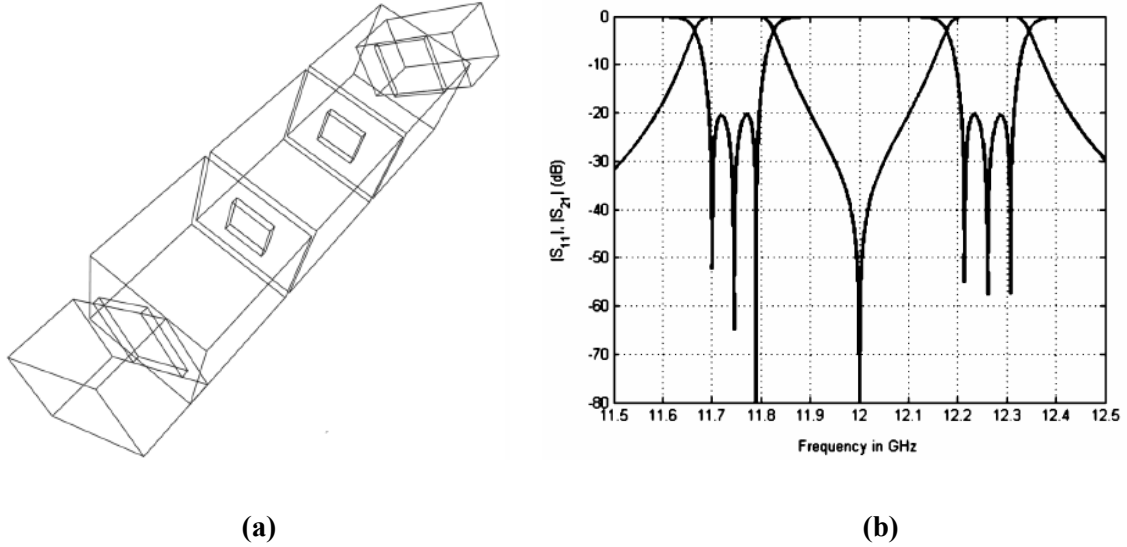
Figure 2.1.4.6: (a) Layout of a 3rd-pole dual-band filter by rectangular resonators and (b) simulated responses [5].

In [24] a combline resonator with dual-band characteristics was reported. The combline resonator is comprised of three levels of metallic conductors, as shown in Figure 2.1.4.7 (a). This structure provides two asynchronous resonant modes (see Figure 2.1.4.7 (b)) that are used for realizing compact microwave dual-band filters. Such dual-band filters offer the low cost, compact size, and ease of manufacturing of traditional combline resonator filters, with additional size reductions due to the fact that a single physical cavity provides two electrical resonators. In addition, the new cavity introduces a transmission zero in the guard-bands, enhancing the filter selectivity while keeping compact inline topology. To show the concept, simulations and experimental results of a tenth-order dual-band filter with a measured rejection level in excess of 100 dB in the guard-band are presented in Figure 2.1.4.8.
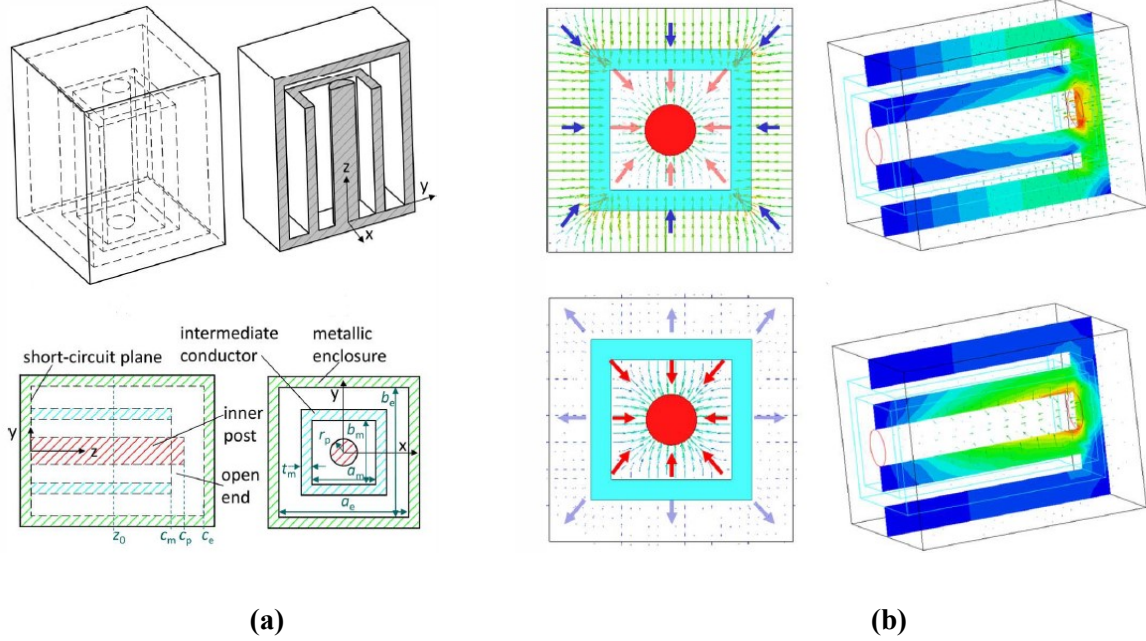
Figure 2.1.4.7: (a) Layout of the combline resonators with three metallic conductors, and (b) electric field pattern of the first and second modes of the dual-band resonators [24].
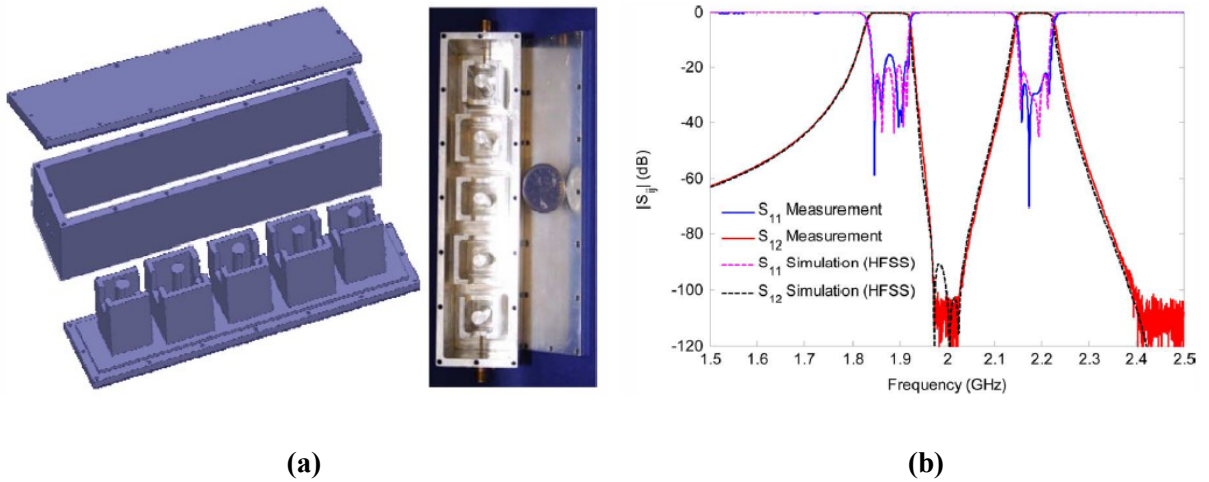
Figure 2.1.4.8: (a) Layout of the 10th pole dual-band filter, and (b) Experimental results of the dual-band filter [24].

23

In [25], an in-line design of a dual-band filter based on a hybrid resonator with widely separated passbands is proposed. The hybrid resonator combines a waveguide cylindrical cavity and a resonant slot, as shown in Figure 2.1.4.9 (a). The resonant slot inside the cavity produces a resonance at a low frequency compared to cavity TE_{11m} resonance, as can be seen in Figs. 2.1.4.9 (b) and (c). The two widely separated resonances can be tuned independently in the resonator. Furthermore, the dual-mode structure offers a good rejection of unwanted resonances, producing a widely separated dual-band response. The concept is experimentally verified by a four-pole filter in Figure 2.1.4.10.

(a)   (b)
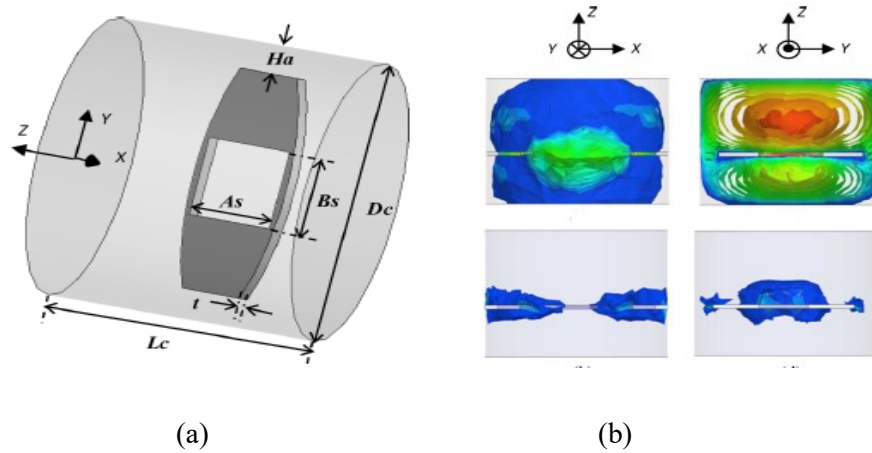
RESONANT MODES IN THE HYBRID DUAL-MODE RESONATOR

Frequency (GHz)	Unloaded Q	Mode
4.96	2169	TE_{108} in the resonant slot
5.62	2042	TE_{118} in the resonant slot
5.87	5330	TM_{010} in the cavity
7.35	1541	Resonance due to openings
8.05	1806	Resonance due to openings
8.70	4966	TE_{111} in the cavity

(c)

Figure 2.1.4.9: (a) Hybrid dual-mode structure composed by a rectangular slot inserted within a cylindrical cavity and (b) (c) resonant modes of the hybrid resonator [25].

24
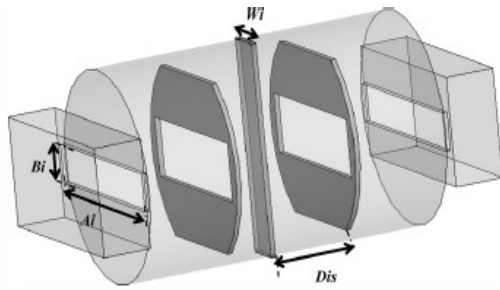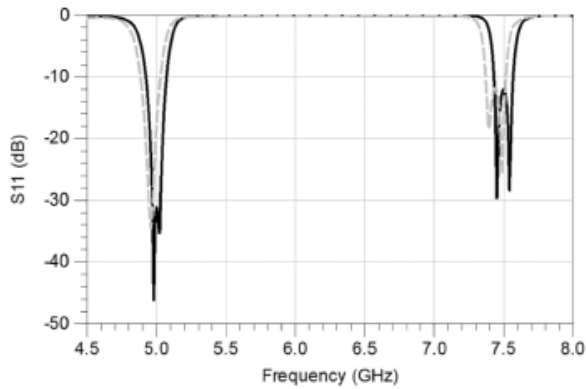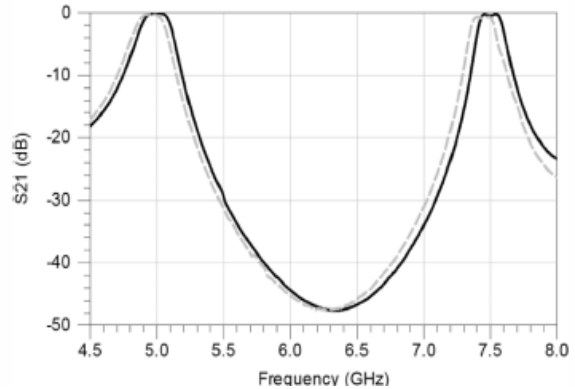
Figure 2.1.4.10: (a) 4-pole Dual-band filter, (b) fabricated filter parts of the filter, (c) comparison of simulated and measured RL for the four-pole filter, and (d) comparison of simulated and measured IL for the four-pole filter [25].

2.1.5   Comparison

The approaches introduced above have their pros and cons and shall be employed accordingly to different requirements and scenarios. A compassion of their characteristics are listed in the table 2.1. As can be observed, in spite of more limitations compared to other approaches, the multi-band filtering realization using multi-mode resonator will provide the highest saving on footprint, mass, size and cost. All the proposed design in this work are based on this configuration.

Table 2.1 Comparison of Approaches to Realize N-band filter

Approach	RF Characteristics	Design Difficulty	Size and Mass	Cost
N× BPF (Channel dropping)	• No interaction between channels • Advanced channel filter function • No limit for # of passband • High Insertion Loss	Low	Large	High
N× BPF (Manifold)	• Advanced channel filter function • No limit for # of passband • Optimum RF response	High	Large / Medium	Large / Medium
1× BPF + (N-1) × BSF	• Modular concept • No limit for # of passband • High Insertion Loss • Limit to narrow guard-band	Low	Large	High
Creating (N-1) transmission zero inside the passband	• Coupling Matrix representation • Advanced channel filter function • Passband # ≤ 4 • Limit to narrow guard-band	High	Medium	Medium
Employing N-mode Resonators	• Coupling Matrix representation • Passband # ≤ 3 • Mostly with Chebyshev function • Limit to wide guard-band • Limit to bandwidth <2%	High	Small	Low

Chapter 3

Coupling Matrix Synthesis of the Multi-band Filter

3.1 Introduction

Coupling matrix [60] model is an efficient tool to represent RF characteristics (e.g. filter order, RL, rejections) of the filter. The coupling matrix parameters are able to link with the physical parameters of the filter hardware, especially for the cavity-based coupled structures. The coupling matrix also enables us to account for electrical characteristics of each element, such as the Q values for each resonator cavity and different dispersion characteristics of the various types of sequential and stray coupling within the filter. All these are difficult or even impossible to achieve by a polynomial representation. Moreover, operations on coupling matrix can be applied, such as inversion, similarity transformation, and partitioning. Such operations simplify the synthesis and performance simulation of complex circuit topologies, and provide the feasibility to extend the coupling matrix from single passband to multiple passbands.

In this chapter, the procedure of synthesizing coupling matrix of single-band filter is first reviewed and detail steps of transferring single-band coupling matrix to multi-band coupling matrix are introduced. The synthesized coupling matrix of the multi-band filter provides the circuit model responses which are the guidance for the various hardware implementation in the following sections.

3.2   Coupling Matrix for Multi-band Filter Network

The coupling matrix synthesis of a single-band filter is explained in detail in [60]. With a given filter order, passband ripple and prescribed zero position, the $N+2$ coupling matrix can be determined. The coupling matrix can be performed similarity transforms (rotations), eliminating the unwanted coupling matrix entries and only remaining the ones that can be realized by filter resonators in preferred configurations.

An equivalent circuit of proposed multi-band filters, in terms of inverters and resonators is shown in Figure 3.2.1. In each multi-mode cavity, there are N resonant modes arranged to carry the signal of P designated passbands, and the P resonant modes in each cavity can be designed with no (or minimum) mutual coupling. The input and output ports directly couple to all P modes in the first and last resonator. Such configuration results a minimum interaction between any two paths when the channel frequencies are considerably far apart from each other. Therefore each path can be treated nearly as a single filter.
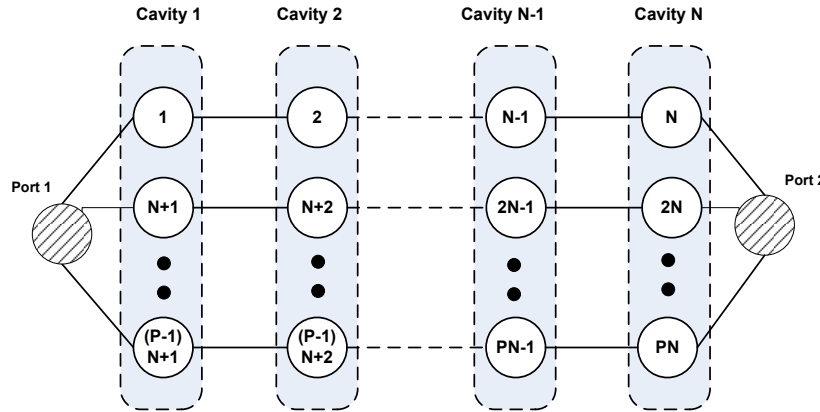
Figure 3.2.1: Equivalent circuit of the P-band filter based on multi-mode Resonator

Because of the non-interaction feature among the signal paths, the coupling matrix of the equivalent circuit in Figure 3.2.1 to yield a specific response can be determined by an extension of the single-band filter synthesis technique with numerical optimizations. Assuming a P-band filter, the CF of all the channels are $f_1, f_2 \ldots f_P$, and the BW of all the channels are BW_1, $BW_2 \ldots BW_P$. If all the channels have the same RL requirement and filter order N, the coupling matrix parameters (normalized) of each channel

would be the same. The coupling matrix of the full multi-band filter can then be generated by following the steps below:

1) Perform coupling matrix synthesis approach as in section 3.2 to all the channels as single-band filter. The parameters in coupling matrix M_k, $k=1,2…P$, should be identical for all the channels, with respective f_k and BW_k.

$$M_k = \begin{bmatrix} 0 & M_{S1} & 0 & 0 & 0 & 0 & 0 \\ M_{S1} & M_{11} & M_{12} & 0 & 0 & 0 & 0 \\ 0 & M_{12} & M_{22} & \ddots & & 0 & 0 \\ 0 & 0 & \ddots & \ddots & \ddots &) & 0 \\ 0 & 0 & 0 & \ddots & N-1 & M_{N-1N} & 0 \\ 0 & 0 & 0 & 0 & M_{N-1N} & M_{NN} & M_{NL} \\ 0 & 0 & 0 & 0 & 0 & M_{NL} & 0 \end{bmatrix} \quad \text{with } f_k \text{ and } BW_k, k=1,2…P \quad (3.1)$$

2) Normalize all channels to f_0 and BW_0 using equations (3.2) and (3.3). Note that f_0, BW_0 and M_{ij_0} could be arbitrary or from any pre-synthesized channel.

$$M_{ii\_k} = -\frac{f_0}{BW_0} \times \left(\frac{f_k}{f_0} - \frac{f_0}{f_k} \right) \quad (3.2)$$

$$M_{ij\_k} = M_{ij\_0} \times \frac{f_0}{f_k} \times \frac{BW_0}{BW_k} \quad (3.3)$$

3) Combine P normalized $N+2$ coupling matrices from step 2 and achieve a large-scale $PN+2$ coupling matrix (3.4) for the P-band filter. Resonators 1~N, $N+1$~$2N$, … $(P-1)N+1$~PN in the combined matrix are corresponding to the resonators for all P channels.

$$(3.4)$$

The S parameters corresponding to the coupling matrix in (3.4) with $CF = f_0$ and $BW = BW_0$ are described in terms of its coupling elements by

$$S_{11} = 1 + 2jRs[\lambda I_{NP} - jR + M]_{11}^{-1} \tag{3.5}$$

$$S_{21} = -2j\sqrt{R_s R_L}[\lambda I_{NP} - jR + M]_{N1}^{-1}, \tag{3.6}$$

Where R is the $NP \times NP$ normalized impedance matrix with all entries zero except for $[R]_{11}=R_{S1\_1}$ and $[R]_{NN}=R_{NL\_P}$. I_{NP} is the $NP \times NP$ identity matrix. M is the $NP \times NP$ symmetric coupling matrix and λ is the normalized frequency variable which is obtained from

$$\lambda = \frac{f_0}{BW_0}(\frac{f}{f_0} - \frac{f_0}{f}) \tag{3.7}$$

4) Based on the initial S-parameter, perform a numerical optimization to the initial $PN+2$ coupling matrix towards the required RF responses.

To demonstrate the above approach, we consider a 9-pole triple-band filter with CFs of 3.8, 4.0 and 4.2 GHz as an example. The BW is 20 MHz and the RL is 30 dB for all channels. The synthesis of single-band 3-pole filter is first performed, and followed by the normalization to $CF = 4.0$ GHz and $BW = 20$ MHz. The three $N+2$ ($N=3$) coupling matrixes are obtained as below,

$$M_{low} = \begin{bmatrix} 0 & 1.402 & 0 & 0 & 0 \\ 1.402 & 50.53 & 1.532 & 0 & 0 \\ 0 & 1.532 & 50.53 & 1.532 & 0 \\ 0 & 0 & 1.532 & 50.53 & 1.402 \\ 0 & 0 & 0 & 1.402 & 0 \end{bmatrix} \quad M_{mid} = \begin{bmatrix} 0 & 1.366 & 0 & 0 & 0 \\ 1.366 & 0 & 1.455 & 0 & 0 \\ 0 & 1.455 & 0 & 1.455 & 0 \\ 0 & 0 & 1.455 & 0 & 1.366 \\ 0 & 0 & 0 & 1.366 & 0 \end{bmatrix}$$

$$M_{high} = \begin{bmatrix} 0 & 1.333 & 0 & 0 & 0 \\ 1.333 & -49.52 & 1.386 & 0 & 0 \\ 0 & 1.386 & -49.52 & 1.386 & 0 \\ 0 & 0 & 1.386 & -49.52 & 1.333 \\ 0 & 0 & 0 & 1.333 & 0 \end{bmatrix} \tag{3.8}$$

The three $N+2$ coupling matrixes in (3.8) are combined and a large-scale $3N+2$ coupling matrix (3.9) for the triple-band filter. Resonators 1~3, 4~6, and 7~9 in the combined matrix are corresponding to the resonators for the low, middle and high channels. The performance of the initial $3N+2$ coupling matrix is as shown in Figure 3.2.2.

$$M = \begin{bmatrix} 0 & 1.402 & 0 & 0 & 1.366 & 0 & 0 & 1.333 & 0 & 0 & 0 \\ 1.402 & 20.53 & 1.538 & 0 & 0 & 0 & 0 & 0 & 0 & 0 & 0 \\ 0 & 1.538 & 20.53 & 1.538 & 0 & 0 & 0 & 0 & 0 & 0 & 0 \\ 0 & 0 & 1.538 & 20.53 & 0 & 0 & 0 & 0 & 0 & 0 & 1.402 \\ 1.366 & 0 & 0 & 0 & 0 & 1.455 & 0 & 0 & 0 & 0 & 0 \\ 0 & 0 & 0 & 0 & 1.455 & 0 & 1.455 & 0 & 0 & 0 & 0 \\ 0 & 0 & 0 & 0 & 0 & 1.455 & 0 & 0 & 0 & 0 & 1.366 \\ 1.333 & 0 & 0 & 0 & 0 & 0 & 0 & -19.52 & 1.386 & 0 & 0 \\ 0 & 0 & 0 & 0 & 0 & 0 & 0 & 1.386 & -19.52 & 1.386 & 0 \\ 0 & 0 & 0 & 0 & 0 & 0 & 0 & 0 & 1.386 & -19.52 & 1.333 \\ 0 & 0 & 0 & 1.402 & 0 & 0 & 1.366 & 0 & 0 & 1.333 & 0 \end{bmatrix}$$

$$\tag{3.9}$$

It is observed in Fig.3.2.2, the filtering performances of all three channels have certain degrees of distortion after combining the three sub-matrices to a full matrix. The distortion is expected because the three channels are connected through the source and load thus interacting with each other. For each filter, the other two filters represent the physical loading through the source and load. The further the filters are far apart, the less loading impact are expected. In this case, the middle channel receives the

loading impacts from both low and high channels and these impacts tend to cancel each other, thus the performance of middle channel has the least distortion compared to the low and high channels. Given the fact that the interaction between channel only (or mostly) happens at the source and load, it becomes possible to achieve equal-ripple responses by only adjusting the value of M_{S1} and M_{3L} for all the filters.
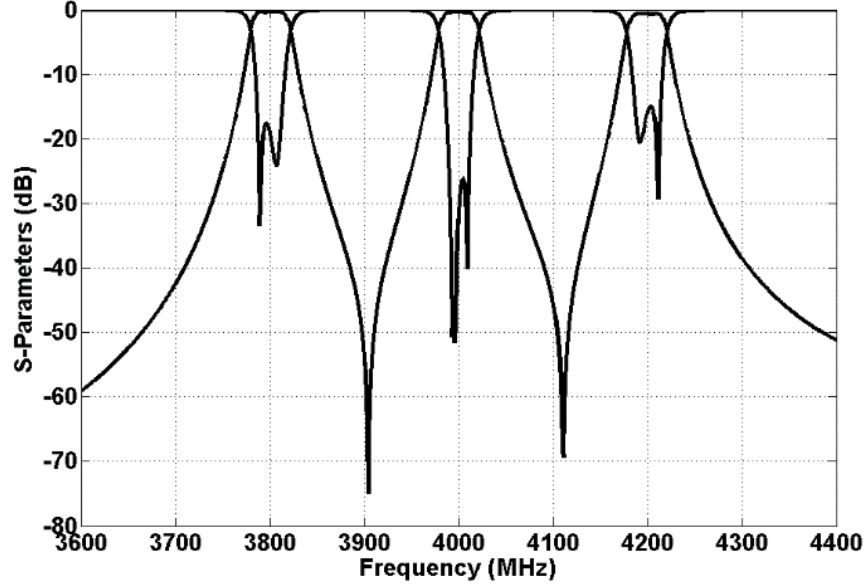
Figure 3.2.2. S-parameter of the initial coupling matrix for the triple-band filter

A MATLAB optimization on the non-zero elements of the initial $3N+2$ coupling matrix (3.9) is performed towards the required RF responses. The optimized $3N+2$ coupling matrix and S-parameters are shown in (3.10) and Figure 3.2.3. It is observed that since the initial coupling matrix parameters and RF performances are numerically close to those from final coupling matrix, thus only minor optimization is required on the initial matrix. As expected, only the external couplings (i.e. M_{S1}, M_{S4}, M_{S7}, M_{3L}, M_{6L} and M_{9L}) of all the filters have relatively larger change while all other coupling parameters almost maintain the same. The simplicity of the optimization process is attributed to the minimum channel-to-channel interaction from the proposed structure in Figure 3.2.1.

$$M = \begin{bmatrix} 0 & 1.426 & 0 & 0 & 1.351 & 0 & 0 & 1.353 & 0 & 0 & 0 \\ 1.426 & 20.77 & 1.568 & 0 & 0 & 0 & 0 & 0 & 0 & 0 & 0 \\ 0 & 1.568 & 20.50 & 1.568 & 0 & 0 & 0 & 0 & 0 & 0 & 0 \\ 0 & 0 & 1.568 & 20.77 & 0 & 0 & 0 & 0 & 0 & 0 & 1.426 \\ 1.351 & 0 & 0 & 0 & -0.01 & 1.438 & 0 & 0 & 0 & 0 & 0 \\ 0 & 0 & 0 & 0 & 1.438 & 0.00 & 1.438 & 0 & 0 & 0 & 0 \\ 0 & 0 & 0 & 0 & 0 & 1.438 & -0.01 & 0 & 0 & 0 & 1.351 \\ 1.353 & 0 & 0 & 0 & 0 & 0 & 0 & -19.77 & 1.409 & 0 & 0 \\ 0 & 0 & 0 & 0 & 0 & 0 & 0 & 1.409 & -19.51 & 1.409 & 0 \\ 0 & 0 & 0 & 0 & 0 & 0 & 0 & 0 & 1.409 & -19.77 & 1.353 \\ 0 & 0 & 0 & 1.426 & 0 & 0 & 1.351 & 0 & 0 & 1.353 & 0 \end{bmatrix}$$

$$(3.10)$$
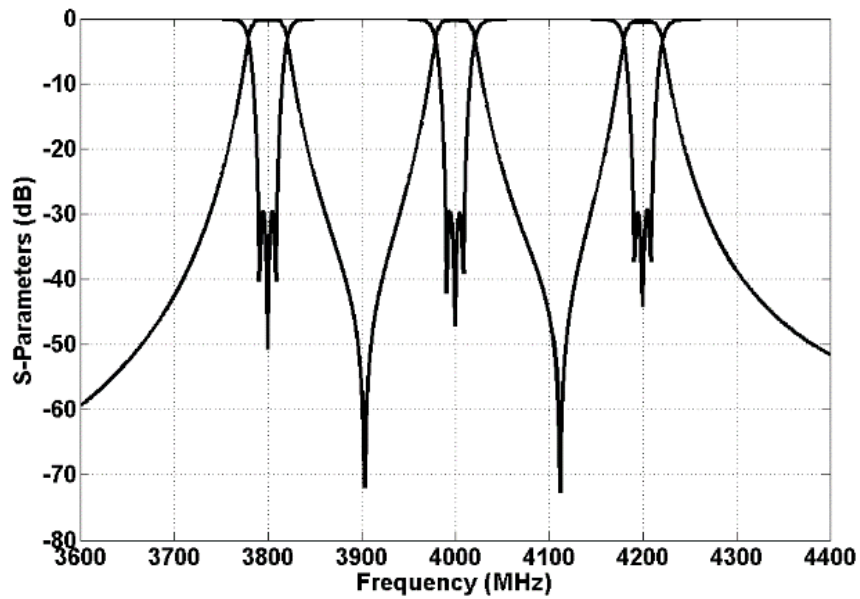
Figure 3.2.3. S-parameter of the final coupling matrix for the triple-band filter

Note that the optimized $3N+2$ coupling matrix can be readily divided into three new $N+2$ sub-coupling matrices. Each sub-matrix is considered as new ideal matrix model targeted by the EM design and optimization of each individual channel.

33

$$M_{low} = \begin{bmatrix} 0 & 1.426 & 0 & 0 & 0 \\ 1.426 & 20.77 & 1.568 & 0 & 0 \\ 0 & 1.568 & 20.50 & 1.568 & 0 \\ 0 & 0 & 1.568 & 20.77 & 1.426 \\ 0 & 0 & 0 & 1.426 & 0 \end{bmatrix} \quad M_{mid} = \begin{bmatrix} 0 & 1.351 & 0 & 0 & 0 \\ 1.351 & -0.01 & 1.438 & 0 & 0 \\ 0 & 1.438 & 0 & 1.438 & 0 \\ 0 & 0 & 1.438 & -0.01 & 1.351 \\ 0 & 0 & 0 & 1.351 & 0 \end{bmatrix}$$

$$M_{high} = \begin{bmatrix} 0 & 1.353 & 0 & 0 & 0 \\ 1.353 & -19.77 & 1.409 & 0 & 0 \\ 0 & 1.409 & -19.51 & 1.409 & 0 \\ 0 & 0 & 1.409 & -19.77 & 1.353 \\ 0 & 0 & 0 & 1.353 & 0 \end{bmatrix}$$

$$(3.11)$$

In Figure 3.2.3, two transmission zeros are located between the adjacent channels. This is due to the phase-reversal between the signals going through the adjacent paths corresponding to the coupling matrix (3.10). In (3.10) all the coupling values are positive, which could be interpreted to all inductive couplings. Considering a 9-pole triple-band filter structure having only inductive coupling between ports and resonators, the phase shift of all the components are shown in Figure 3.2.4. The relationship between the phase shift and different coupling structures is well demonstrated in [61]. The generation of the first transmission zero is mainly contributed by the low and middle channels since the high channel has a much lower S_{21} magnitude response at the frequency of the first transmission zero making minimum contribution to the response. Similarly the generation of the second transmission zero is mostly contributed by the middle and high frequency bands. Table 3.1 example 1 shows the results that the transmissions zeros are generated from the two adjacent out-of-phase paths. The frequencies of the transmission zeros are almost exactly coincident with the frequencies at which the individual single filter responses cross each other. In practice, the coupling inside the filter could have different sign resulting in-phase condition thus diminishing certain transmission zero. For instance only changing the input coupling on path 2 from -90° to +90°, results in-phase condition on both frequencies between passband as shown in Table 3.1 example 2. Figure 3.2.5 shows the corresponding frequency responses with two transmission zeros diminished.
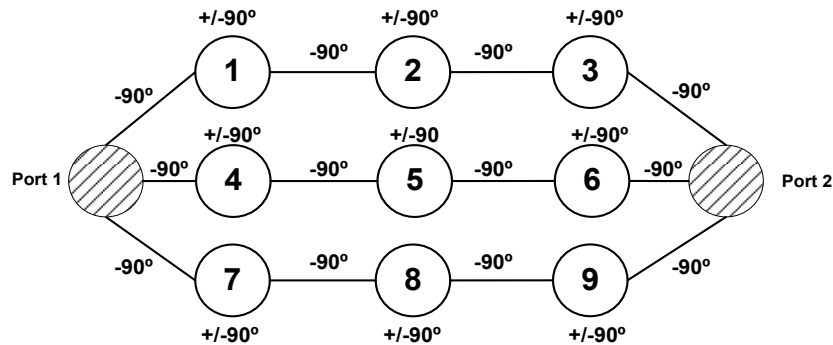
Figure 3.2.4. Phase shift distribution of the components in the three signal paths.

Table 3.1 Phase Shift Calculation for the Three Paths of Triple-band Filter

		@ Frequency of 1st Transmission Zero	@ Frequency of 2nd Transmission Zero
Ex. 1	Low Frequency Path (Resonator 1-2-3)	-90°-90°-90°-90° -90°-90°-90° = -270°	Not Contributed
	Mid. Frequency Path (Resonator 4-5-6)	-90°+90°-90°+90° -90°+90°-90° = -90°	-90°-90°-90°-90° -90°-90°-90° = -270°
	High Frequency Path (Resonator 7-8-9)	Not Contributed	-90°+90°-90°+90° -90°+90°-90° = -90°
	Result	**Out of phase**	**Out of phase**
Ex. 2	Low Frequency Path (Resonator 1-2-3)	-90°-90°-90°-90° -90°-90°-90° = -270°	Not Contributed
	Mid. Frequency Path (Resonator 4-5-6)	**+90°**+90°-90°+90° -90°+90°-90° = +90°	+90°-90°-90°-90° -90°-90°-90° = -90°
	High Frequency Path (Resonator 7-8-9)	Not Contributed	-90°+90°-90°+90° -90°+90°-90° = -90°
	Result	**In phase**	**In phase**
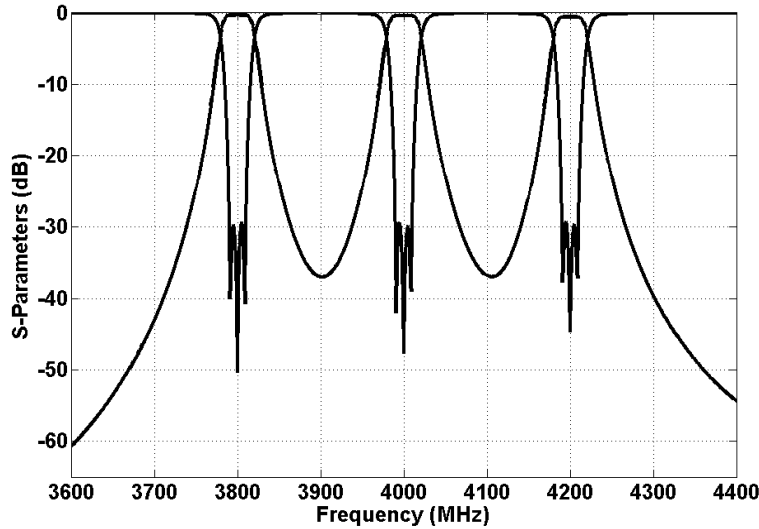
Figure 3.2.5. S-Parameter of the triple-band filter (transmission zeros diminished)

After achieving the coupling matrix of the multi-band filter, the electromagnetic (*EM*) design of the multi-band filter configuration can start from the design method of single channel filters introduced in [60], with specific requirements of each design parameters reflected by the sub-channel coupling matrix. The critical design procedures include:

1) Define the multi-mode resonator with desired realization (waveguide or dielectric) having the multiple operating modes resonate at the designated frequencies. At the meantime a sufficient spurious-free window need to be verified for a proper targeted filter bandwidth.

2) Realization of inter-resonator coupling. The internal coupling of each signal path needs to be individually controlled and yields the coupling coefficients associated with the three resonant nodes. A minimum interaction among adjacent paths is required.

3) Realization of input/output coupling. The input/output configuration must be able to couple to the three modes simultaneously with a pre-defined coupling amount to each mode.

4) An iterative optimization of each channel need to be performed after achieving the initial responses to compensate the unavoidable channel-to-channel interference.

Chapter 4

Compact Waveguide Dual-band Filters and Diplexers

4.1   Introduction

The development of multiple services and the need to use several frequency bands has triggered the demand for highly integrated dual-band filters to improve the RF/microwave front-ends. In the payload system of a high throughput satellite, the multi-band filtering configuration can be employed after the high power amplifier to collect multiple non-adjacent passbands for the designated spot beam while rejecting the passbands from other spot beams. Those multi-band filters require high power handling and low IL, narrowing the realization to metallic cavity / waveguide structures.

4.2   Elliptical Dual-mode Resonator

Cylindrical dual-mode bandpass filters [62]–[63] have been developed over several decades and have become a popular solution for satellite transponders because of their compact size and ability to realize advanced filtering functions. The conventional dual-mode filters mostly operate in TE_{11m} mode. In [64]-[65], elliptical cavities have also been used to design dual-mode filters with improved Q and ease of manufacturing. In this section, the elliptical cavity is employed to realize a dual-mode resonator for the dual-band application, as shown in Figure 4.2.1. The operating modes in the elliptical cavity are based on TE_{11n} mode degeneracy, similar to the cylindrical cavity. The dual resonators are tuned at independent frequencies by the cavity diameter difference along the two elliptical axes. The two orthogonally polarized modes are intrinsically isolated and can be designed to carry two passband signals. For our application, the dual-band structure has to be dimensioned to produce two resonances at frequencies of

f11m_v and f_{11m_H}. The dual resonant frequencies of a dual-band cavity can be approximately calculated by equations (4.1) and (4.2).

$$f_{11m\_V} \approx \frac{c}{2\pi}\sqrt{(\frac{p'_{11}}{a})^2 + (\frac{m\pi}{l})^2} \, , \tag{4.1}$$

$$f_{11m\_H} \approx \frac{c}{2\pi}\sqrt{(\frac{p'_{11}}{b})^2 + (\frac{m\pi}{l})^2} \, , \tag{4.2}$$

where p'_{11} represents the first zero of the derivative of the one-order first kind Bessel function J_m, c represents the speed of light in the waveguide, and a and b represent cavity radius along the horizontal and vertical axes, respectively. From the equations, the frequency differentiation between the two polarized modes is determined by the ratio of a and b. A larger ratio offers less interaction between the two bands. In cases of applications with small guard-band, the ratio will be close to 1. In these situations, tuning screws are essential for splitting the two polarized frequencies.

By performing an eigenmode analysis with full-wave EM software, resonant modes can be calculated in the elliptical dual-band cavity. For cavity dimensions of a = 0.44", b = 0.488", and l = 0.68", and considering a structure made of copper, the resonant frequencies and the unloaded quality factors are listed in Table 4.1. In this case, only the TE_{111} modes are of interest. The adjacent modes TM_{010} and TM_{011} are nearly 1500 MHz lower and higher, respectively, yielding an acceptable spurious-free window. Moreover the spurious TM mode has no H-field distribution along the plane of end wall, which can be effectivity decoupled by using inductive coupling irises. Therefore the spurious-free window is further improved.

In the elliptical cavity, two pairs of tuning screws are located along vertical and horizontal axes, providing the flexibility to adjust the resonant frequencies of each band. Unlike the dual modes, which are excited one by one along the signal path in a conventional dual-mode cylindrical cavity, the dual TE_{11m} modes in the elliptical cavity are not coupled. Intra-coupling only happens between adjacent cavities by modes with the same E-field orientation. For instance, the horizontal TE_{11m} in cavity 1 will only couple with the horizontal TE_{11m} in cavity 2. The input and output waveguide excites the two orthogonal modes simultaneously at the end cavities. The details on the coupling structure will be introduced in the next section.
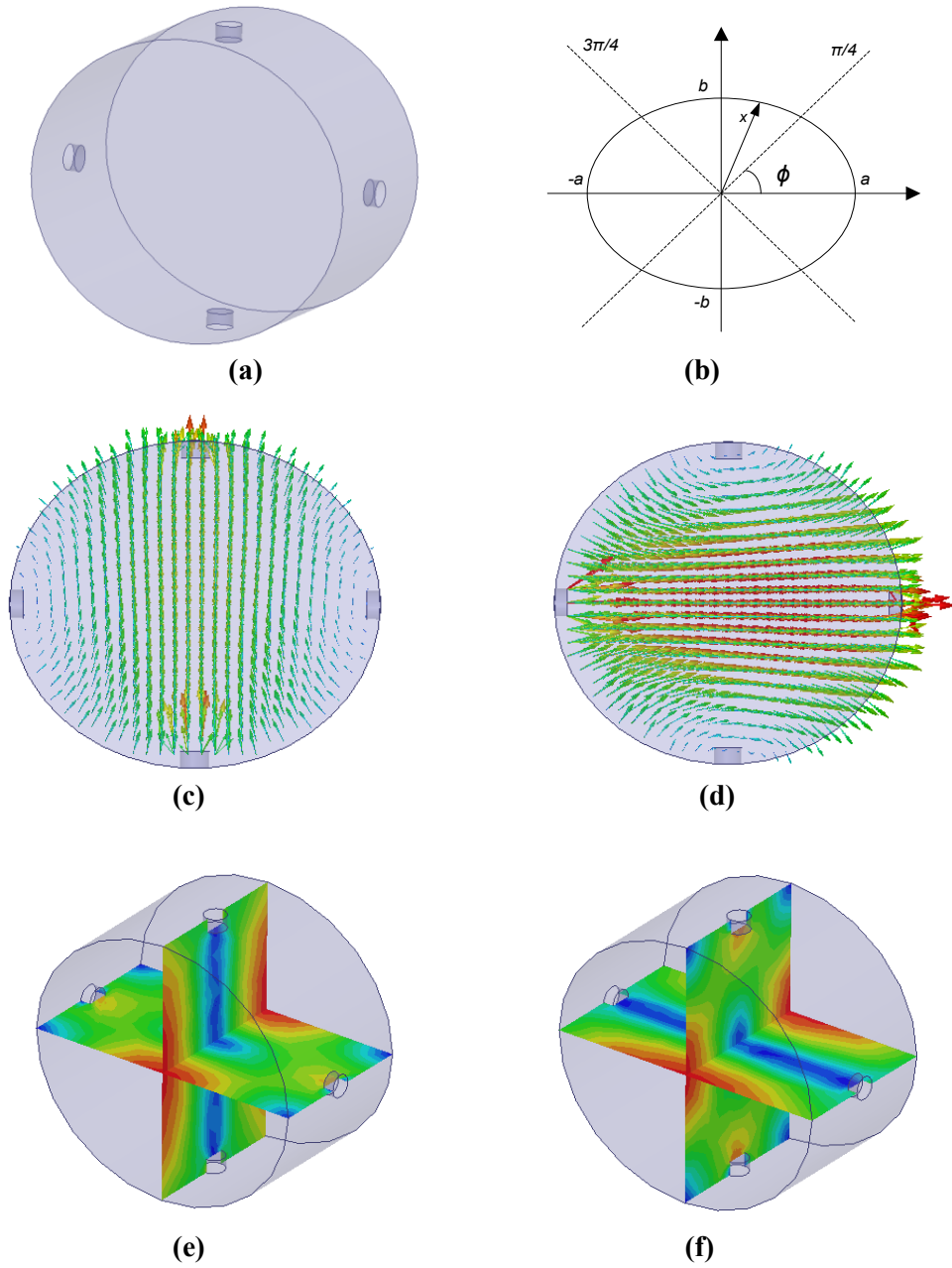
Figure 4.2.1 (a) Elliptical dual-mode resonator layout, (b) Transversal cross-section of the Elliptical cavity, (c-d) Electrical field vector of two orthogonal TE$_{111}$ resonant modes, and (e-f) Magnetic field of two orthogonal TE$_{111}$ resonant modes.

Table 4.1 Resonant Modes in the Elliptical Dual-Band Cavity

Mode	Frequency (GHz) from Eigen-mode Simulation	Frequency (GHz) from Equation (1) and (2)	Unloaded Q
TM_{010}	9.91	-	10314
TE_{111_V}	**11.28**	**11.25**	**11311**
TE_{111_H}	**11.75**	**11.71**	**11899**
TM_{011}	13.17	-	8513
TE_{211}	15.14	-	11670

4.3 Elliptical Dual-band Filter and Diplexer

4.3.1 Equivalent Circuit

The equivalent circuit of the proposed dual-band filters and diplexers, in terms of inverters and resonators, is shown in Figs. 4.3.1(a)–(c). The rectangles with a dashed boundary represent the dual-mode resonators carrying the signals of two paths. If N cavities are used, each path contains N resonators that are directly coupled by inverters. Because the two modes in the dual-band cavities are orthogonally polarized, the equivalent circuits consist of two parallel non-interacting paths except the common input/output section. As a result, the coupling matrix parameters of this class of dual-band filter and diplexer can be extracted almost as single filters without considering manifold and phase factors, as is the case with traditional designs. For the dual-band filter, the two paths are connected to the input and output nodes. For the diplexer case in Figure 4.3.2(b), the two paths split at the last cavity, resulting in two channels with the same filter order. In Figure 4.3.2(c), additional single-band resonators can be added after the group of dual-mode resonators, offering flexibility in channel filter order and improved channel-to-channel isolation. The proposed concept is applicable to most dual-mode resonators.
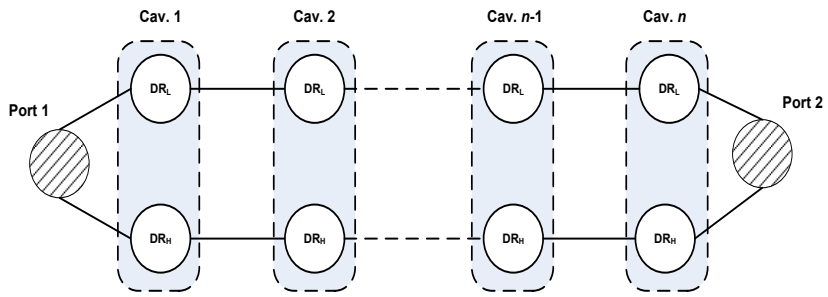
(a)
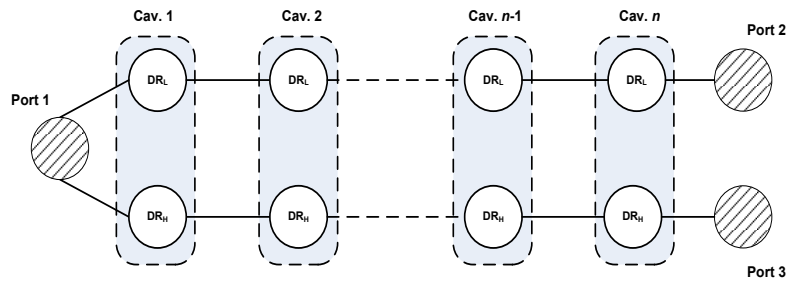
(b)
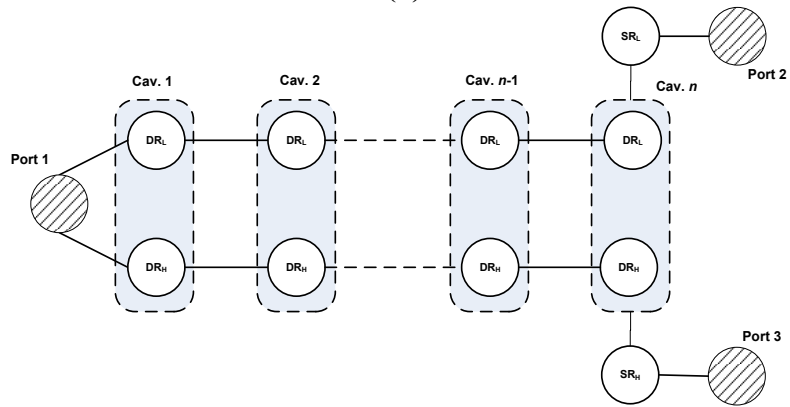
(c)

Figure. 4.3.1 Equivalent Circuit of (a) dual band filter, (b) diplexer with dual-mode resonators, and (c) diplexer with dual-band and single-band resonators.

4.3.2 Input Coupling

The input coupling coefficients are related to the maxima of the group delay of the input reflection coefficient S_{11} [60]. For dual-band filter and diplexer applications, there will be two group delay peaks corresponding to the higher and lower bands. The iris and resonator dimensions are tuned until the two resonance peaks fit the desired values. As shown in Figure 4.3.2.1(a), the feeding waveguide is rotated by angle φ to excite two orthogonal modes simultaneously with a round iris. Both angle φ and the iris dimensions determine the couplings to the two modes. Figure 4.3.2.1(c) shows the group delay response with different angles of φ from 0° to 90°. When φ equals 0°, the feeding waveguide is horizontal and couples only to the vertical TE_{11m} mode; when φ equals 90°, the feeding waveguide is vertical and only excites the horizontal TE_{11m}; and when φ is close to 45°, the input coupling could be evenly distributed

(a)   (b)

(c)
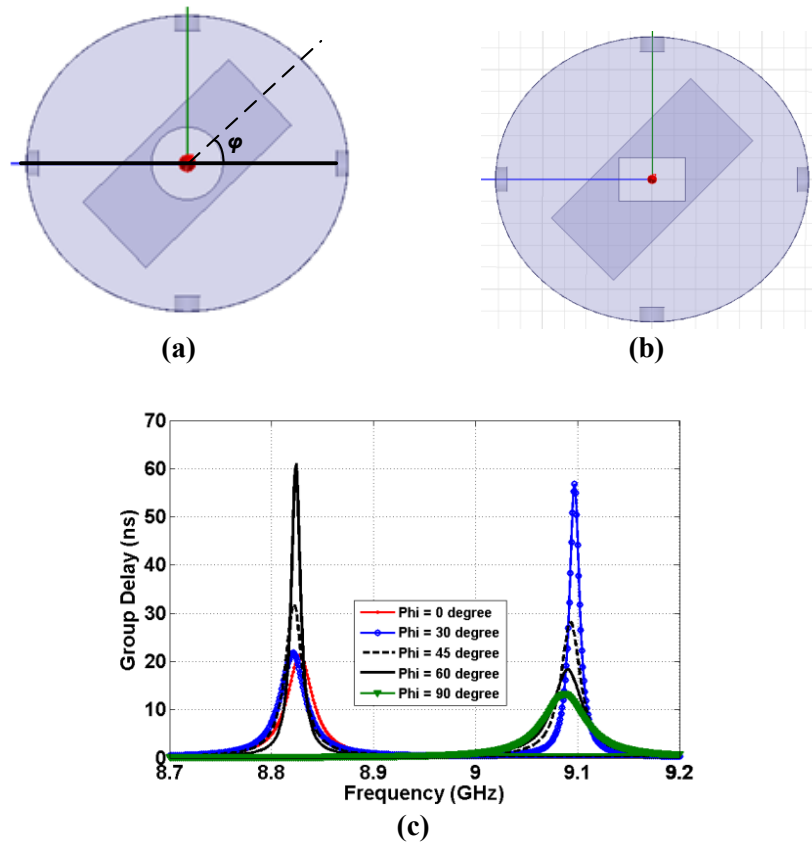
Figure 4.3.2.1 (a) Input coupling with round iris, (b) input coupling with rectangular iris, and (c) group delay response with different angle φ.

in both directions. The input iris could also be an asymmetrical shape, e.g., rectangular, as shown in Figure 4.3.2.1(b). The ratio of length to width of the iris adds an extra degree of freedom to control the coupling distribution to the two polarizations.

It is worth noting that the reflected group delay method [60] for computing the input couplings of multi-bands has higher accuracy when the resonant frequencies of the two bands are well separated, with a mutual distance that is greater than the coupling bandwidth. This is because the intrinsic coupling between the two orthogonal modes in the dual-mode cavity becomes considerable when their frequencies are close. Figure 4.3.2.2 (a) shows a circuit model of the input coupling to two resonant modes with a mutual coupling K_{12} between them. Figure 4.3.2.2(b) shows the group delay response with different K_{12}. When the mutual coupling equals 0, the two group delay peaks are balanced; when the mutual coupling increases the two group delay peaks deviates from the nominal values in opposite directions. In this case, the waveguide angle φ or rectangular iris ratio need to be re-adjusted to achieve the desired input coupling value for the two channels.

| (a) | (b) |
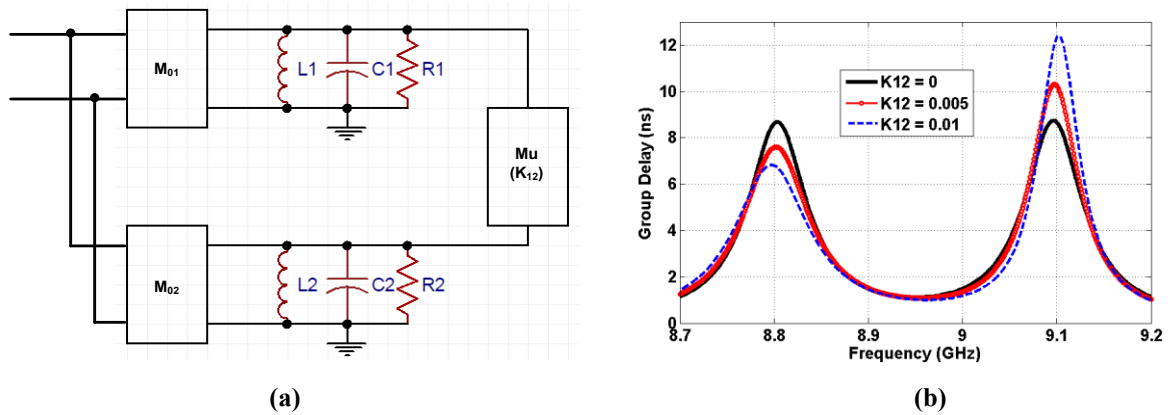
Figure 4.3.2.2 (a) circuit model of input coupling with mutual coupling between two resonators, and (b) group delay response with different mutual coupling K_{12}.

4.3.3 Intra-cavity Coupling

As mentioned above, the signals in dual-band filters and diplexers are transmitted along two parallel non-interacting paths; hence, inter-cavity coupling only occurs between resonant modes with the same orientation. In this case, irises with cross-slots in Figure 4.3.3.1 are proved to be the optimum solution to couple both polarizations with minimum interaction and are thus suitable for wide-band designs with relatively small guard-band. Each branch of the cross-slot couples the energy at one polarization, which is proportional to the branch length L_1 or L_2 respectively. Using eigenmode simulation by placing an electric and magnetic wall along the symmetry plane [19], four resonant frequencies are calculated as shown in Table 4.2. The coupling coefficients are then computed by the equations (4.3),

$$k_i = \frac{f_{2i}^2 - f_{2i-1}^2}{f_{2i}^2 + f_{2i-1}^2}, \quad i = 1, 2 \tag{4.3}$$

where $f_1 \sim f_4$ are the two pairs of eigenmodes of the two adjacent dual-mode resonators.

| (a) | (b) |
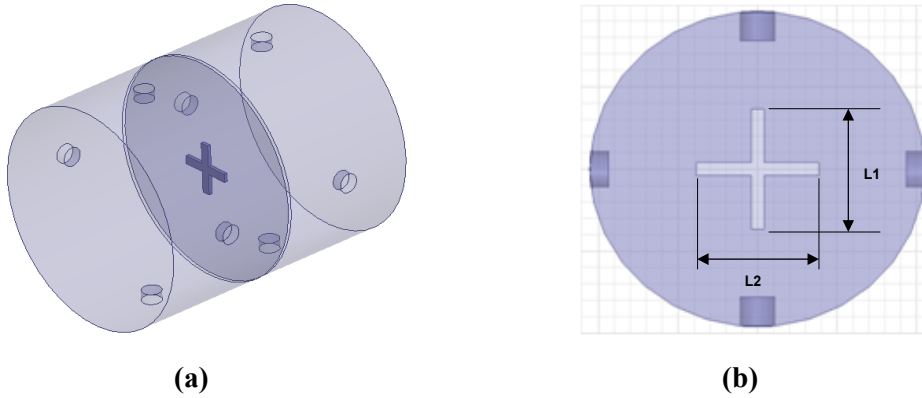
Figure 4.3.3.1. Configuration of (a) intra-cavity coupling with cross-slot iris, and (b) transverse view of the cross-slot iris.

Table 4.2

Eigenmode simulation results for intra-cavity Coupling when $L_1 = 0.3$ inch and $L_2 = 0.3$ inch

Mode	Eigenmode Freq. (GHz)	Coupling Coefficients. by (4.3)
$TE_{111\_V\_Cav1}$	$f_1 = 8.831$	$k_1 = 0.0037$
$TE_{111\_V\_Cav2}$	$f_2 = 8.864$	
$TE_{111\_H\_Cav1}$	$f_3 = 9.090$	$k_2 = 0.0034$
$TE_{111\_H\_Cav2}$	$f_4 = 9.121$	

Figure 4.3.3.2 shows the relationship between the branch length and the inter-cavity coupling coefficients. The results indicate this configuration has a capability of controlling the coupling along the two signal paths individually. Similar to the limitation of the input coupling, the accuracy of equation (4.3) decreases when the frequencies of the two bands are close, due to a non-negligible mutual coupling between the two modes in the same cavity.

(a) (b)
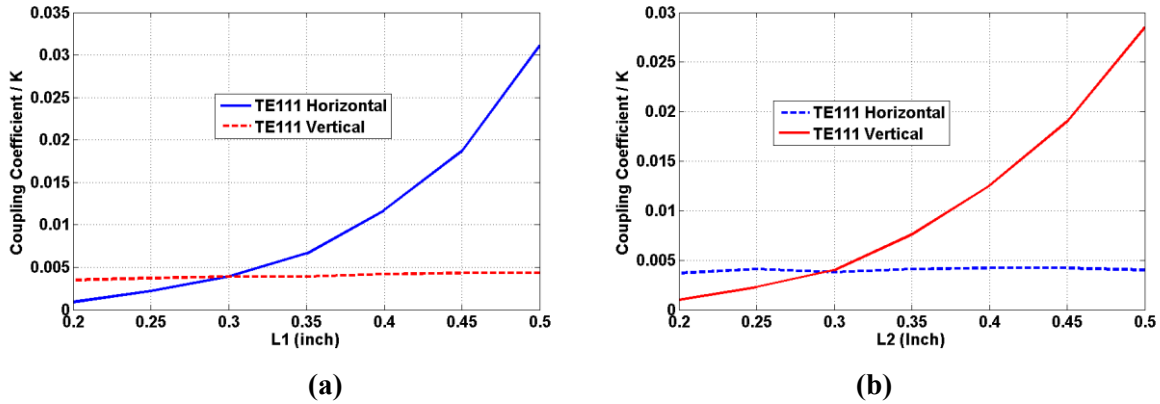
Figure 4.3.3.2(a) Relationship between the branch length (L1 and L2) of the cross iris and inter-cavity coupling coefficients.

4.3.4 Output Coupling

For the dual-band filter design, the configuration of the output coupling is identical to that of the input coupling. For the diplexer design, the output ports are positioned perpendicularly on adjacent sides of the last dual-band cavity, correspondingly coupled to the two orthogonal polarized TE_{111} modes. The perpendicular outputs provide extra isolation between two channels. The design of the output irises is similar to that of the input iris, the only difference being that the two maxima group delays are achieved by two paths separately.

4.3.5 Elliptical Dual-band Filter Design

In order to prove the feasibility of the proposed approach, an 8th order Ku-band dual-band filter has been designed to implement the equivalent circuit in Figure. 3.3.1(a). The RF specifications of the filter are shown in Table 4.3.

Table 4.3 Ku Dual-band Filter specifications

Parameter	RF Specifications
Passband	
Band 1	10962 – 11062 MHz
Band 2	11488 – 11688 MHz
Insertion Loss at CF	0.4 dB
Rejections	
CF ± 118.8 MHz	10.5 dB
CF ± 129.6 MHz	20.5 dB
Gain Flatness	
CF±85.5 MHz	0.3 dB
CF±97.2 MHz	0.55 dB
Group Delay Variation	
CF±97.2 MHz	11.0 ns
Return Loss	
CF±85.5 MHz	24 dB
CF±97.2 MHz	22 dB

Using the filter synthesis approach in chapter 3, the coupling matrix of the 16-pole dual-band filter is as follows in (4.4),

$$
M = \begin{bmatrix}
0.00000 & 1.22213 & 0.00000 & 0.00000 & 0.00000 & 0.00000 & 0.00000 & 0.00000 & 0.00000 & 1.22200 & 0.00000 & 0.00000 & 0.00000 & 0.00000 & 0.00000 & 0.00000 & 0.00000 & 0.00000 \\
1.22213 & 2.45000 & 0.99750 & 0.00000 & 0.00000 & 0.00000 & 0.00000 & 0.00000 & 0.00000 & 0.00000 & 0.00000 & 0.00000 & 0.00000 & 0.00000 & 0.00000 & 0.00000 & 0.00000 & 0.00000 \\
0.00000 & 0.99750 & 2.00000 & 0.65540 & 0.00000 & 0.00000 & 0.00000 & 0.00000 & 0.00000 & 0.00000 & 0.00000 & 0.00000 & 0.00000 & 0.00000 & 0.00000 & 0.00000 & 0.00000 & 0.00000 \\
0.00000 & 0.00000 & 0.65540 & 2.00000 & 0.59300 & 0.00000 & 0.00000 & 0.00000 & 0.00000 & 0.00000 & 0.00000 & 0.00000 & 0.00000 & 0.00000 & 0.00000 & 0.00000 & 0.00000 & 0.00000 \\
0.00000 & 0.00000 & 0.00000 & 0.59300 & 2.00000 & 0.57980 & 0.00000 & 0.00000 & 0.00000 & 0.00000 & 0.00000 & 0.00000 & 0.00000 & 0.00000 & 0.00000 & 0.00000 & 0.00000 & 0.00000 \\
0.00000 & 0.00000 & 0.00000 & 0.00000 & 0.57980 & 2.00000 & 0.59300 & 0.00000 & 0.00000 & 0.00000 & 0.00000 & 0.00000 & 0.00000 & 0.00000 & 0.00000 & 0.00000 & 0.00000 & 0.00000 \\
0.00000 & 0.00000 & 0.00000 & 0.00000 & 0.00000 & 0.59300 & 2.00000 & 0.65540 & 0.00000 & 0.00000 & 0.00000 & 0.00000 & 0.00000 & 0.00000 & 0.00000 & 0.00000 & 0.00000 & 0.00000 \\
0.00000 & 0.00000 & 0.00000 & 0.00000 & 0.00000 & 0.00000 & 0.65540 & 2.00000 & 0.99750 & 0.00000 & 0.00000 & 0.00000 & 0.00000 & 0.00000 & 0.00000 & 0.00000 & 0.00000 & 0.00000 \\
0.00000 & 0.00000 & 0.00000 & 0.00000 & 0.00000 & 0.00000 & 0.00000 & 0.99750 & 2.45000 & 0.00000 & 0.00000 & 0.00000 & 0.00000 & 0.00000 & 0.00000 & 0.00000 & 0.00000 & 1.22200 \\
1.22200 & 0.00000 & 0.00000 & 0.00000 & 0.00000 & 0.00000 & 0.00000 & 0.00000 & 0.00000 & -2.45000 & 0.99750 & 0.00000 & 0.00000 & 0.00000 & 0.00000 & 0.00000 & 0.00000 & 0.00000 \\
0.00000 & 0.00000 & 0.00000 & 0.00000 & 0.00000 & 0.00000 & 0.00000 & 0.00000 & 0.00000 & 0.99750 & -2.00000 & 0.65540 & 0.00000 & 0.00000 & 0.00000 & 0.00000 & 0.00000 & 0.00000 \\
0.00000 & 0.00000 & 0.00000 & 0.00000 & 0.00000 & 0.00000 & 0.00000 & 0.00000 & 0.00000 & 0.00000 & 0.65540 & -2.00000 & 0.59300 & 0.00000 & 0.00000 & 0.00000 & 0.00000 & 0.00000 \\
0.00000 & 0.00000 & 0.00000 & 0.00000 & 0.00000 & 0.00000 & 0.00000 & 0.00000 & 0.00000 & 0.00000 & 0.00000 & 0.59300 & -2.00000 & 0.57980 & 0.00000 & 0.00000 & 0.00000 & 0.00000 \\
0.00000 & 0.00000 & 0.00000 & 0.00000 & 0.00000 & 0.00000 & 0.00000 & 0.00000 & 0.00000 & 0.00000 & 0.00000 & 0.00000 & 0.57980 & -2.00000 & 0.59300 & 0.00000 & 0.00000 & 0.00000 \\
0.00000 & 0.00000 & 0.00000 & 0.00000 & 0.00000 & 0.00000 & 0.00000 & 0.00000 & 0.00000 & 0.00000 & 0.00000 & 0.00000 & 0.00000 & 0.59300 & -2.00000 & 0.65540 & 0.00000 & 0.00000 \\
0.00000 & 0.00000 & 0.00000 & 0.00000 & 0.00000 & 0.00000 & 0.00000 & 0.00000 & 0.00000 & 0.00000 & 0.00000 & 0.00000 & 0.00000 & 0.00000 & 0.65540 & -2.00000 & 0.99750 & 0.00000 \\
0.00000 & 0.00000 & 0.00000 & 0.00000 & 0.00000 & 0.00000 & 0.00000 & 0.00000 & 0.00000 & 0.00000 & 0.00000 & 0.00000 & 0.00000 & 0.00000 & 0.00000 & 0.99750 & -2.45000 & 1.22213 \\
0.00000 & 0.00000 & 0.00000 & 0.00000 & 0.00000 & 0.00000 & 0.00000 & 0.00000 & 1.22200 & 0.00000 & 0.00000 & 0.00000 & 0.00000 & 0.00000 & 0.00000 & 0.00000 & 1.22213 & 0.00000
\end{bmatrix}
$$

(4.4)

Figure 4.3.5.1 shows the structure of the 16-pole dual-band filter comprised of six TE_{112} mode and two TE_{113} mode elliptical cavities, to meet the requirement of Q_u and the spurious-free window. The filter was manufactured from invar alloy with silver plating. The ratio of the horizontal and vertical axis length of the elliptical cavity is around 1.15. An average Q_u of 18000 and a spurious-free window from 10 to 12.5 GHz is achieved. In this design, step-transformer portions are added between the interface waveguide and the input/output iris to increase the coupling to both resonant modes for a relatively wide fractional BW (about 2%). Figure 4.3.5.2 (a) shows the measured performance compared with the simulation. The filter is tuned to show all sixteen poles in return loss peaks and the response well matches with simulation. The measured *RL* is better than 24 dB and the *IL* is 0.38 dB instead of 0.35 dB, as simulated. All other RF parameters are compliant with the specification, with sufficient thermal margins.

A method to generate a transmission zero between the two bands is introduced in [5]. Based on the order of each band, the orientation of the feeding waveguides is parallel or perpendicular to each other. This creates a phase-reversal between the signals going through the two orthogonal polarizations. At a frequency between the two bands, one polarization is capacitive and one is inductive, thus each dual-band cavity introduces a phase difference of 180° between the two polarizations. For an 8th order filter design, an eight multiple of 180° is resulted at the output. No transmission zeros are generated unless the output is rotated by 90° to introduce phase reversal. Figure 4.3.5.2 (b) shows a comparison of *S*-parameters before and after rotating the output port of the 16-pole dual-band filter.
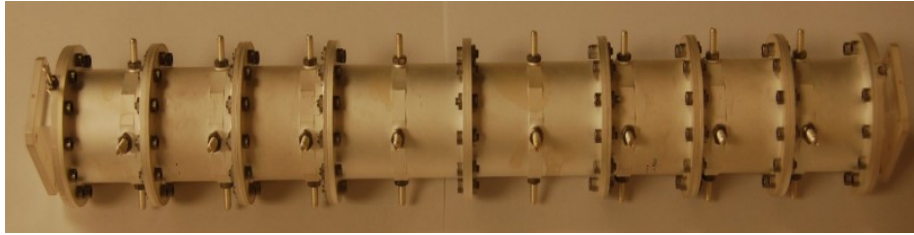
Figure 4.3.5.1: Fabricated 16-pole dual-band filter with elliptical cavities.

<div align="center">(a)</div>

<div align="center">(b)</div>
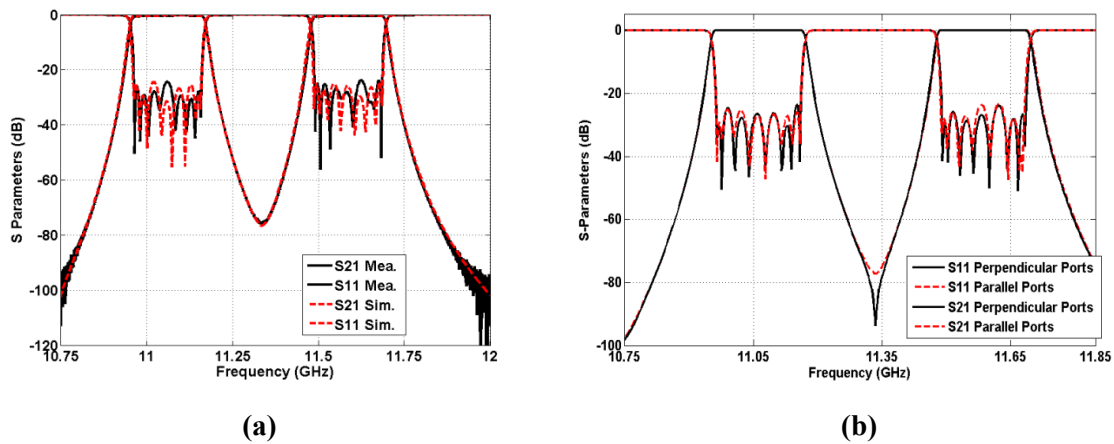
Figure 4.3.5.2. (a) Measured and simulated S-parameters of the 16-pole dual-band filter, and (b) comparison of the S-parameters with different orientations of input and output ports.

4.3.6 Elliptical Diplexer Design

A 16-pole diplexer design based on the elliptical cavity is shown in Figure. 4.3.6 (a) to implement the equivalent circuit in Figure. 4.3.1.1 (b). The design approach of the diplexer is similar to that of the dual-band filter, except for the output configuration. Both channels are operated with TE_{111} mode. The two output ports are positioned perpendicularly on adjacent sides of the last dual-band cavity. The diplexer response is shown in Figure. 4.3.6 (b). The diplexer CFs are at 8.8 and 9.05 GHz, and the BWs are both 25 MHz. The rejection between two paths is greater than 50 dB and the RL is better than 20dB. An S_{21} hump is observed in each channel locating at the frequency of passband of its adjacent channel,

representing the interaction between the two paths. The hump is intrinsic from this type of diplexer because the two outputs share the same resonator and isolation between channels is only provided by the orthogonal polarization. In this case the hump level is lower than 60dB, thereby maintaining sufficient isolation between the two channels. The hump level can be reduced by increasing the filter order or by adding extra single mode resonators after the last dual mode resonator as shown in Figure 4.3.1.1(c). It is worth to note that the single mode resonator has flexibility of other realization, i.e. not restricted with elliptical cavity resonator.

(a) (b)
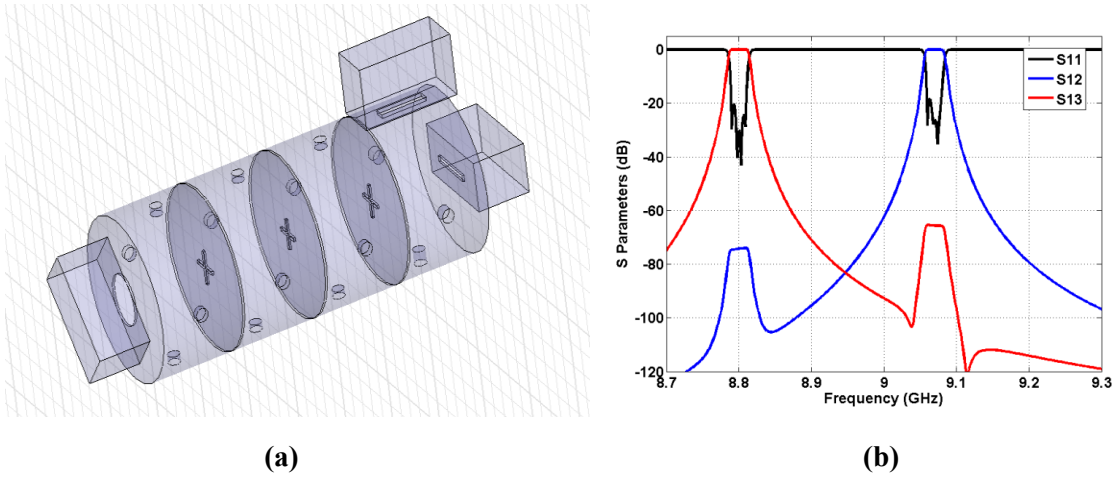
Figure 4.3.6 (a) Layout of the 8-pole elliptical cavity diplexer, and (b) simulated S-parameters.

4.4 Conclusion

The chapter has presented dual-band filters using elliptical dual-mode resonators. Each passband of the dual-band filter is controlled by a dedicated polarization and can be represented by an inline direct-coupled set of resonators, thereby allowing a simple design process. The detailed design approach for each parameter of the proposed structure has been discussed and verified by a Ku-band 16-pole dual-band filter. The dual-band structure can be easily transfer to diplexer structure by modify the output ports at the last resonators.

Chapter 5

Quasi-Elliptic Waveguide Dual-band bandpass filters

5.1 Introduction

The development of space telecommunications requires filters with transmission zeros for improving the selectivity and/or flattening the group delay. In the last chapter, the approach of using the dual-mode resonator to implement dual-band filtering functions provides a dramatic saving in footprint and volume while maintaining high Q of each resonator. However this type of waveguide dual-band filter structure has two drawbacks: 1) filter functions with cross-couplings cannot be readily implemented thus mostly realizing Chebyshev filter functions; 2) The in-line configuration with a high-order filter function could lead to a long filter, especially in the waveguide design. To the best of authors' knowledge, [66] is the only reported work using purely multi-mode resonators while featuring symmetric finite transmission zeros. However the use of the quadruple-mode resonators limits the dual-band filter to applications of very narrow bandwidth (BW<0.5%). In this chapter, several configurations are proposed to overcome the limitations thus improving the performance of the dual-band cavity filter.

5.2 Rectangular Dual-band Filter with Transmission Zeros

In this section, a new class of dual-band filter and diplexer structures are proposed by a combination of dual-band and single-band resonators. The equivalent circuits of the dual-band filter and diplexer are shown in Figure 5.2.1. The single-band resonators are located between any two dual-mode resonators realizing tri-section structures to offer transmission zeros. Similar to the circuits in Figure.4.3.1.1, the

dual-mode resonators carry both channel signals with orthogonal polarizations, while the single-mode resonators transmit one channel. Because the two modes in the dual-band cavities are orthogonally polarized, the two parallel paths are non-interacting. The elliptical dual-band cavity introduced earlier is not an ideal candidate for the tri-section topology due to the layout difficulty and high manufacturing cost. A rectangular dual-mode resonators were introduced in [5] to generate dual-band filtering performances, however only realizing Chebyshev responses. The technology introduced in this section dramatically improves the selectivity of the dual-band filters and diplexers by using a "dual-trisection" structure while still maintaining a compact layout.
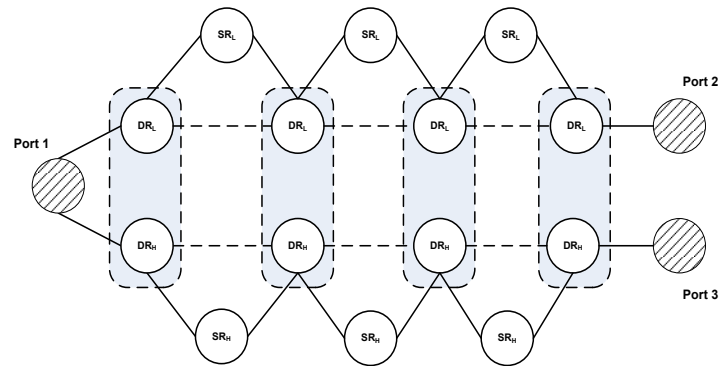
(a)
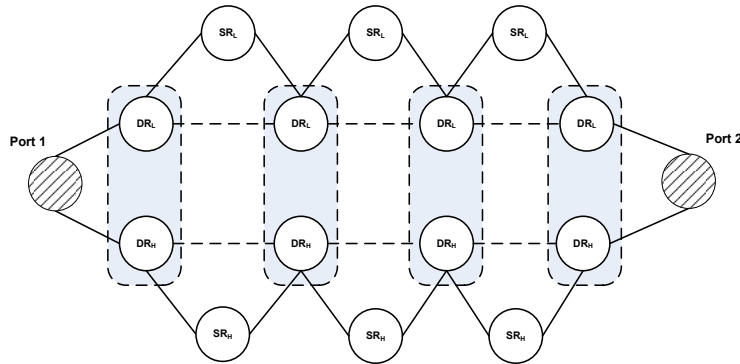
(b)

Figure 5.2.1. Equivalent circuit of (a) diplexer, and (b) dual-band filter with combination of dual-band and single-band resonators.

5.2.1 Rectangular Dual-mode Resonator

The rectangular dual-mode cavities with orthogonal modes TE_{10m} and TE_{01m} were introduced to realize dual-band filters with Chebyshev function. The resonant frequency of the TE_{10m} mode is determined by the cavity width a and length l, while the resonant frequency of TE_{01m} is determined by the cavity height b and length l, as stated in (5.1),

$$f_{10m} = \frac{c}{2\pi}\sqrt{(\frac{\pi}{a})^2 + (\frac{m\pi}{l})^2}, \quad f_{01m} = \frac{c}{2\pi}\sqrt{(\frac{\pi}{b})^2 + (\frac{m\pi}{l})^2}, \tag{5.1}$$

where c represents the speed of light in the waveguide. The ratio of a/b reflects the frequency differentiation between the two polarized modes.

One unique feature of the rectangular dual-band cavity is potential Q improvement from the conventional rectangular filter design. For TE_{10n} mode, the Q can be calculated as (5.2)

$$Q_u = \frac{(kad)^3\eta}{2\pi^2 R_s} \times \frac{1}{(2n^2a^3 + 2d^3 + \frac{n^2a^3d + ad^3}{b})}. \tag{5.2}$$

Thus increasing "b" dimension of a rectangular waveguide resonator can effectively improve the quality factor of the TE_{10m} mode, but will suffer from the cut-off frequency of TE_{01} mode (*i.e.* the first spurious mode after increasing "b") shifting closer to the passband, decreasing the spurious-free window. In the proposed structure, the original spurious-mode TE_{011} is employed in parallel with TE_{101} mode as two pass-bands frequencies, hence the "b" dimensions are dramatically increased with respect to both polarizations in the dual-band cavities resulting a higher Q for both channels without sacrificing the spurious-free window.

5.2.2 Dual Tri-section Unit

A compact dual tri-section is realized by positioning two single-band TE_{101} resonators between the two adjacent dual-band TE_{101} / TE_{011} resonators, as shown in Figure 5.2.2. This configuration generates two transmission zeros, one on either side of each passband. If a structure contains N dual-mode resonators, a maximum total of $2(N-1)$ transmission zeros can be achieved in the RF response. Each dual-band

cavity is attached with two sequential coupling irises and two cross coupling irises. The top and side vertical irises are for one channel, while the front and side horizontal irises are for the other. The signal paths of the two channels inside the structure are also illustrated in Figure 5.2.2. All inner coupling irises are designed in along rectangular shape, aiming to minimize the cross-talk between the polarized modes. The dimensions of the irises are determined by the coupling matrix parameters from both channels. Another interesting feature of the dual tri-section unit is the resonator dimension offset. The "*a*" and "*b*" dimensions of the single-band resonator is offset from those of dual-mode resonators. This results in the same over-modes resonating at different frequencies therefore suppressing each other to lower the far-band spurious level. The dual-band filter and diplexer employing the dual tri-section unit is expected to feature smaller size but higher *Q,* and improved rejections at both near-band frequencies (because of transmission zeros) and far-band frequencies (because of dimensions offset).
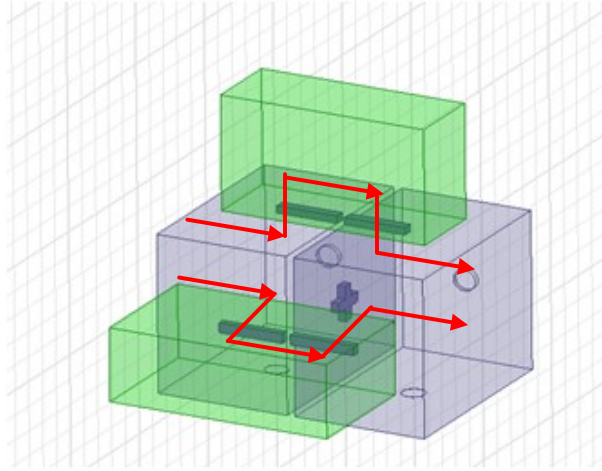
Figure 5.2.2. Layout of a dual-trisection unit with signal paths of dual polarizations.

5.2.3 Rectangular Dual-band Filter and Diplexer Design

Rectangular dual-band filters and diplexers can be developed on the basis of the dual tri-section unit. Besides the coupling configuration included in the dual-trisection module, other couplings are similar to those presented in chapter 4. A layout of a 6-pole dual-band filter based on the dual-trisection structure is shown in Figure 5.2.3.1. Each channel has a 3-1-0 filter function. Similar to the elliptical dual-band

filter, the input and output ports are rotated to couple both TE_{101} and TE_{011} modes. The simulated dual-band response with a pair of transmission zeros at the near band is shown in Figure 5.2.3.2.
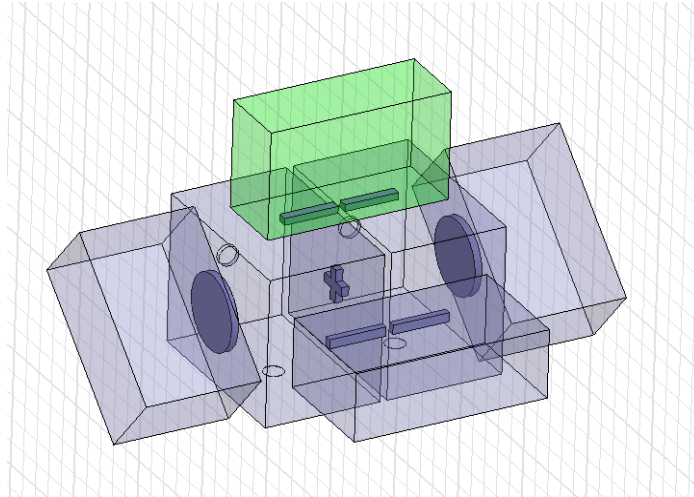
Figure 5.2.3.1. Layout of a 6-pole dual-band filter based on dual-trisection module.
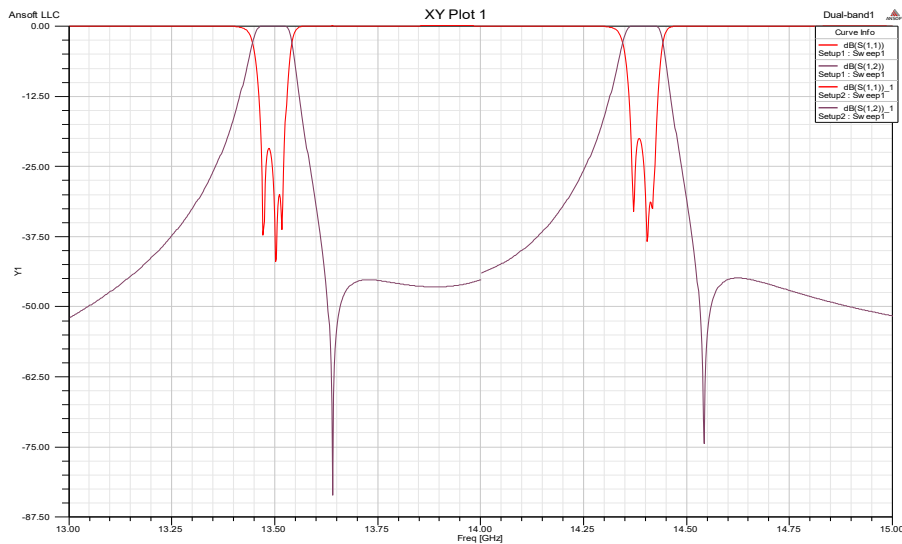
Figure 5.2.3.2. Simulated *S*-parameter of the 6-pole dual-band filter.

Similarly, the dual-band filter can be extended to diplexer by positioning the output ports perpendicularly on adjacent sides of the last dual-band cavity. In Figure 5.2.3.3, an 8-pole Ku-band

diplexer has been designed using *HFSS*. In the front and top view of the proposed diplexer, electric field flows are illustrated at each channel's operating frequencies, demonstrating the non-interacting feature between the two paths. Except for the input portion, each channel of the diplexer is designed separately. One transmission zero is added at each path for a better selectivity. The *N+2* coupling matrix for the lower channel can be considered as

$$M = \begin{bmatrix} 0 & 1.2679 & 0 & 0 & 0 & 0 \\ 1.2679 & 0.0505 & 1.1548 & 0.3026 & 0 & 0 \\ 0 & 1.1548 & -0.3393 & 0.8217 & 0 & 0 \\ 0 & 0 & 0.8217 & 0.0913 & 1.1938 & 0 \\ 0 & 0 & 0.3026 & 1.1938 & 0.0505 & 1.2679 \\ 0 & 0 & 0 & 0 & 1.2679 & 0 \end{bmatrix} \tag{5.3}$$

The coupling matrix for the higher channel has the same value with opposite signs. The diplexer center frequencies are at 13.71 and 14.0 GHz, the bandwidths are both 100 MHz, the rejection between two paths is greater than 25 dB, and the *RL* is better than 20dB. As discussed earlier, the increase of the "*b*" dimension considerably improves the *Q* of both channels in the dual-band cavities. Table 5.1 shows an unloaded *Q* comparison between the proposed design and the traditional design. The overall unloaded *Q* improvement is expected to be over 10% from the proposed structure.
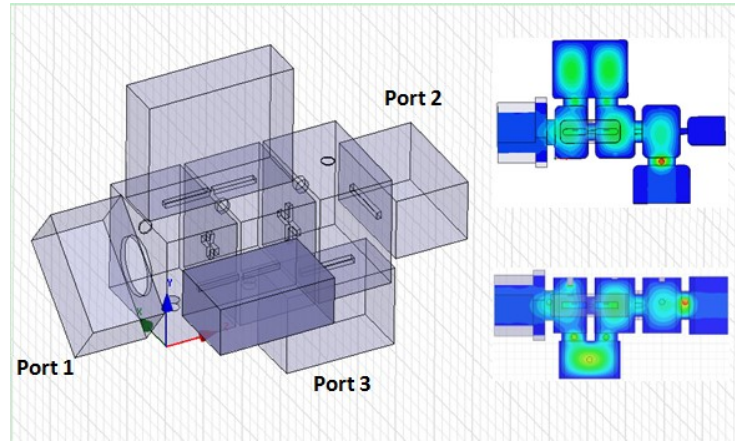
Figure 5.2.3.3. Internal layout of an 8-pole diplexer and its front and top view of *E*-field flows.

Table 5.1 Unloaded Q Comparison

		Proposed Diplexer	Traditional Diplexer
Unloaded Q	TE_{101} Mode	8700	7500
	TE_{011} Mode	9100	-
	TE_{102} Mode	9600	9600
	Overall	8800	7750

The designed diplexer was manufactured from two halves of copper, as can been seen in Figure 5.2.3.4(a). Tuning screws are added for independent control of frequency and coupling parameters. Figure 5.2.3.4 (b) shows the measured performance compared with the simulation. The measured *RL* is better than 25 dB, and rejection at adjacent channels is more than 30 dB. The measured *IL* is 0.48 dB instead of 0.39 dB, as simulated. The tuned performance is slightly off from the simulation due to the machining tolerance and metal roughness. To obtain a sufficient frequency margin for thermal drift, both channels were not tuned to achieve equal-rippled response. Two humps are observed near the transmission zeros, representing the interaction between the two channels but do not impact the design specifications. It is worth noting that the proposed diplexer is not recommended for cases with small guard-band (e.g., less than channel bandwidth) due to high level of humps caused by a stronger interaction between two channels. Although the hump level can be reduced by increasing the filter order or by adding extra single mode resonators after the last dual-mode resonator, it dramatically increases the size and mass of the diplexer thus reducing its efficiency. Meanwhile, the strong interaction of the two perpendicular polarized modes in the dual-band cavities dramatically increases the diplexer sensitivity during design and tuning process.

In Figure 5.2.3.5 (a), the layout of the proposed diplexer is compared with a traditional H-plane diplexer designed to the same specifications. The traditional diplexer is operating in TE_{101} and TE_{102} modes, and was manufactured from silver plated aluminum. The proposed design achieved a footprint saving over 50% and a volume saving over 30% from the traditional H-plane design. The *IL* of the proposed diplexer is measured to be 0.48 dB. The *IL* will be improved after silver plating, resulting in better than the *IL* (0.47dB) of the traditional design. Figure 5.2.3.5 (b) shows a comparison of the out-of-band performance of the two diplexers, where the dashed line is the traditional diplexer and the solid

trace is the proposed diplexer. The proposed diplexer improved the rejection performance by more than 20 dB.
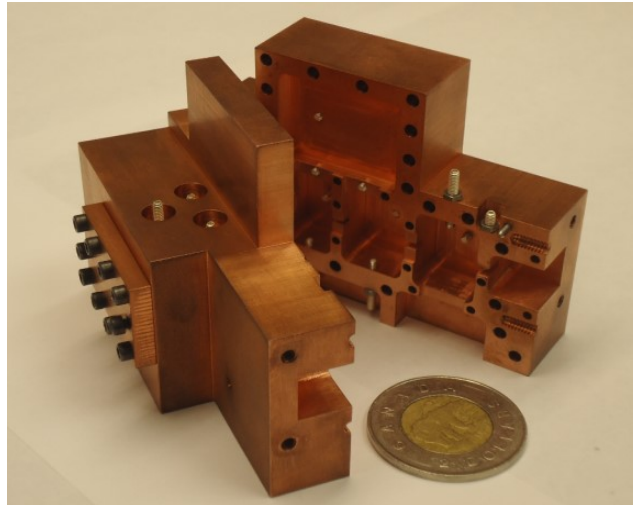
(a)
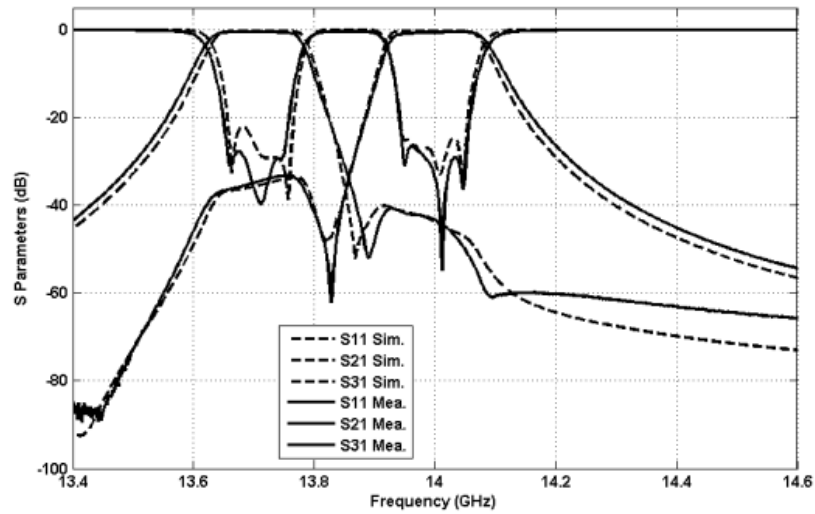
(b)

Figure 5.2.3.4: (a) Fabricate diplexer structure, and (b) measurement (Solid) and simulation (dashed) comparison of the 4-order diplexer
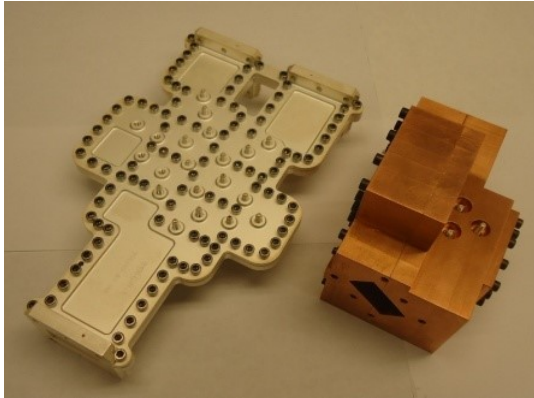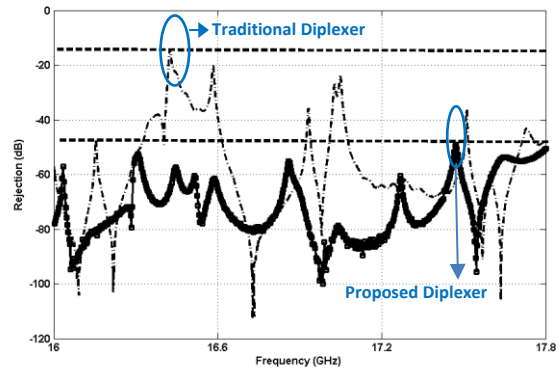
Figure 5.2.3.5: (a) Layout comparison between the proposed diplexer (brown) and the conventional diplexer (white), and (b) spurious comparison between the proposed diplexer and the traditional design.

5.3 Side-Coupled Dual-band Filter with Elliptical Cavity

In the above section, the transmission zeros are realized by combining single-mode and dual-mode resonators. The dual-trisection module is compact however only realizes one transmission zero for each of the passband. To realize a pair of transmission zeros on either side of each passband, at least 5 resonators (2 single-mode resonators and 3 dual-mode resonators) on each path are required. In addition, the center dual-mode resonator requires to couple with 4 single-mode resonators simultaneously thus not a practical solution. Further, the stacked resonators would have a complicated layout increasing the difficulty of manufacturing.

In this section, a side-coupled configuration is proposed to realize the dual-band filter and implemented in elliptical waveguide resonators for the first time. The new configuration leads to a significant reduction in the filter footprint compared to the design in 4.3 and 5.2, and facilitates cross-coupling to realize a pair of transmission zeros at either side of each passband. The dual-band filter structure allows independent control of each frequency and coupling parameters of the two channels.

The design approach and experimental results are presented for a prototype filter to validate the proposed concept.

5.3.1 Dual Quadruplet Configuration

Figure 5.3.1.1 illustrates the equivalent circuit of the proposed "dual quadruplet" configuration. The dashed rectangles represent the dual-mode resonators. The fixed and dashed line represent sequential and cross coupling respectively, establishing a dual 4-2-0 quadruplet configuration. In each resonator, the two modes are orthogonally polarized and each mode carries the signal of a passband. The two signal paths do not interact with each other, with the exception of the input/output section of the filters. Thus each channel can be designed individually as similar to a single filter.

The circuit model in Figure 5.3.1.1 can be realized by elliptical cavity dual-mode resonators as shown in Figure 5.3.1.2. The four elliptical resonators are operating in dual TE_{112} modes and are side-coupled to form a quadruplet configuration. The intra-cavity coupling is comprised of two sub-sections and each sub-section corresponds to the coupling to one signal path. The section can be either a rectangular iris or an electrical probe depending on the sign of the coupling parameter. It is worth noting that the negative coupling (i.e. probe coupling) could be set between any adjacent cavities to ease the manufacturing of the filter structure. The features of resonator and coupling configurations will be discussed in the following subsections.
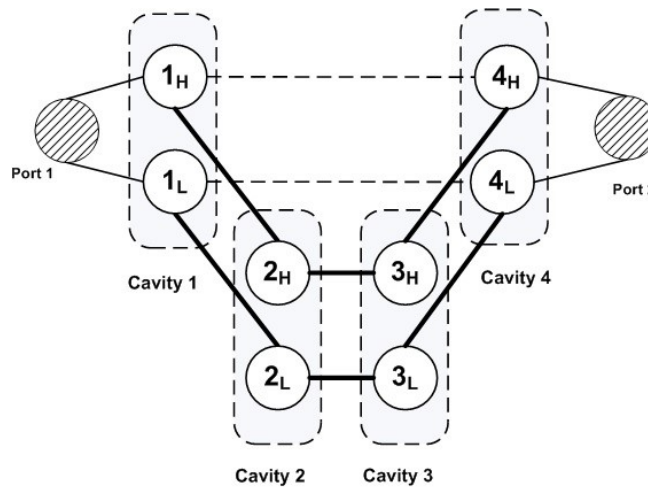
Figure 5.3.1.1: Equivalent circuit of dual quadruplet configuration.

59
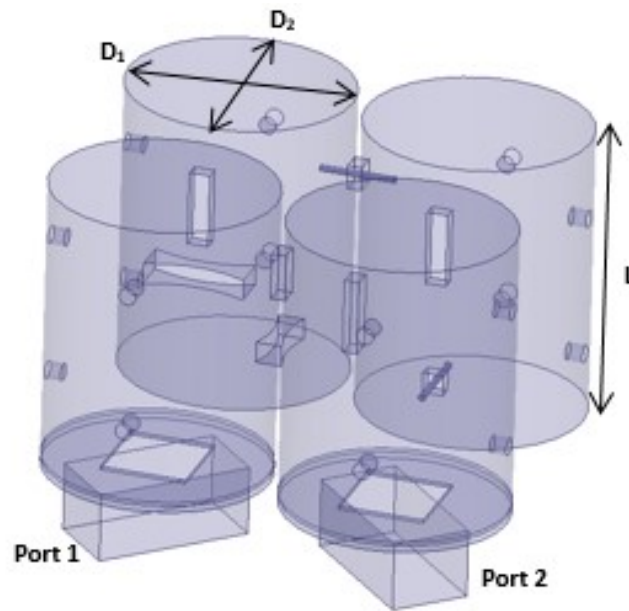
Figure 5.3.1.2: Realization of dual quadruplet configuration by elliptical dual-mode resonator.

5.3.2   *TE*112 Dual-mode Elliptical Resonator

For each elliptical resonator, the diameters (D_1 and D_2) along the major and minor axis are selected to achieve the widest spurious-free window and at the meantime control the frequency offset between the two degenerated TE_{112} modes. Two pairs of tuning screws in each resonator provide additional control of the degenerated TE_{112} resonant frequencies. The spurious mode distribution is determined by the elliptical cavity dimensions and can be approximately predicted by the mode chart of the cylindrical cavity. Figure 5.3.2.1 and Figure 5.3.2.2 show two mode charts of the cylindrical cavity having the operational TE_{112} frequencies 3.435 and 3.565 GHz respectively. The diameters (D_1=86.4 mm and D_2 =78.7 mm) along the major and minor axis of the elliptical cavity are selected respectively from the mode charts in order to maximize the spurious-free window. From the eigen-mode simulation result as shown in Table 5.2, the closest adjacent spurious modes of the elliptical resonator are TM_{011} and TE_{211} locating at the frequencies at least 200 MHz away from the operational frequencies 3.435 and 3.565 GHz of TE_{112} modes. The unloaded Q is around 23000 based on copper surface, which is close to that of the cylindrical dual-mode resonator at the same frequency. .
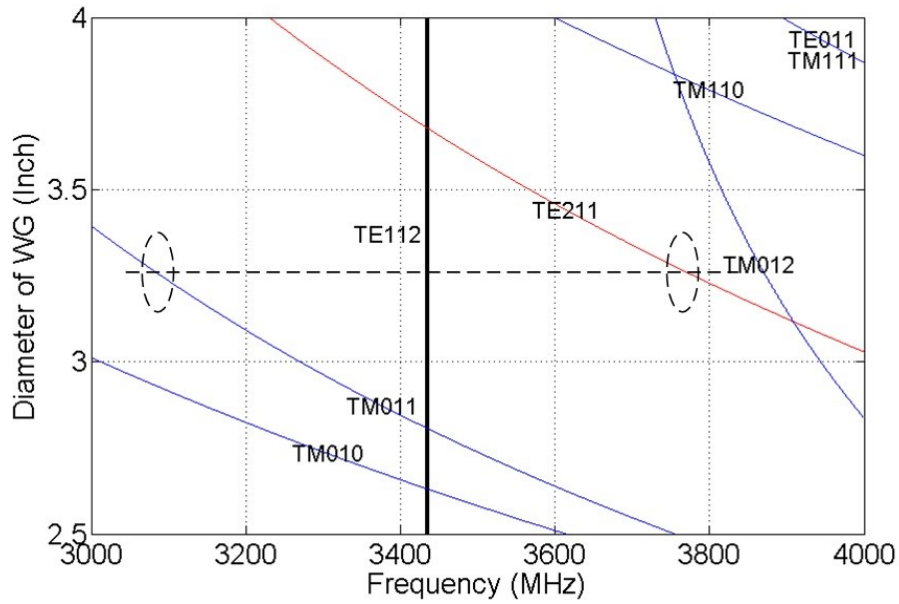
Figure 5.3.2.1: Mode chart of cylindrical cavity with *TE*₁₁₂ mode at 3.435 GHz.
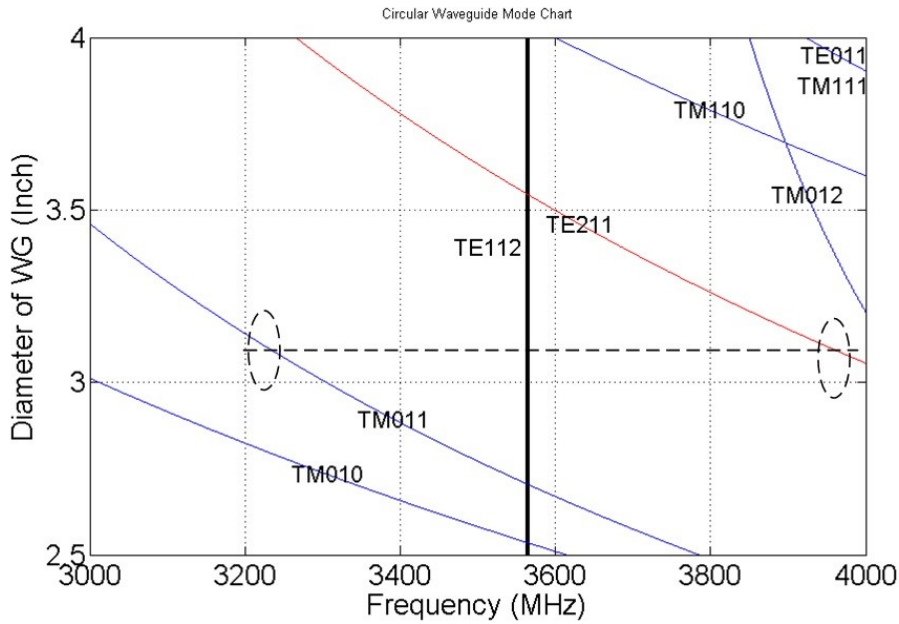
Figure 5.3.2.2: Mode chart of cylindrical cavity with *TE*₁₁₂ mode at 3.565 GHz.

Table 5.2. Eigen-mode simulation of elliptical resonator

Dimensions (mm)	Mode	Frequencies (GHz)	Unloaded Q (Copper surface)
D_1 = 86.4 D_2 = 78.7 L = 107.7	TM_{011}	3.223	18681
	TE_{112}	3.435	22784
	TE_{112}	3.565	23717
	TE_{211}	3.784	17479

5.3.3 Coupling Configuration

To achieve the independent control of intra-cavity couplings along the two signal paths, two sets of coupling configuration are shown in Figure 5.3.3 (a) and (b). As shown in Figure 5.3.3(c)-(e), the vertical iris along the Z orientation locates at one-quarter/three-quarter height (i.e. maximum H-field) of the resonator and aims to only couple the Y-oriented (E-field) TE_{112} mode. For the X-oriented (E-field) TE_{112} mode, two options can be chosen: 1) a horizontal iris located at the center of the resonator (i.e. maximum H-field) to provide magnetic (positive) coupling, and 2) an electric probe located at one-quarter/three-quarter height of the resonator (i.e. maximum E-field) to provide electric (negative) coupling. The dimensions of the irises and probes are determined by the coupling matrix parameters of the dual-band filter. Using eigen-mode simulation by placing an electric and magnetic wall along the symmetry plane [60], four eigen-mode frequencies $f_1 \sim f_4$ can be achieved and the de-normalized coupling coefficients k_1 and k_2 are then computed by (5.4),

$$k_i = \frac{f_{2i}^2 - f_{2i-1}^2}{f_{2i}^2 + f_{2i-1}^2}, \quad i = 1, 2 \tag{5.4}$$

The input/output coupling of the proposed filter are realized by rectangular irises, similar to the structure in chapter 4. The ratio of length to width of the iris controls the coupling distribution to the two polarizations. The waveguide interface is rotated by an angle to excite the two orthogonal TE_{112} modes simultaneously. The input/output coupling coefficients are related to the maxima of reflected group delay at the input and output which can be achieved through EM simulation [60]. It is noted that the TM_{011} mode does not have magnetic field along the cross-section, thus the TM_{011} mode can hardly propagate inside the filter structure through the input/output coupling window.

(a)

(b)

(c)

(d)

(e)
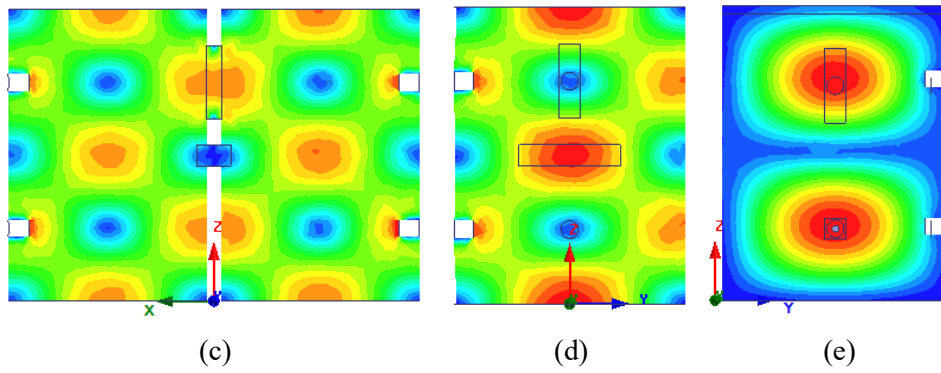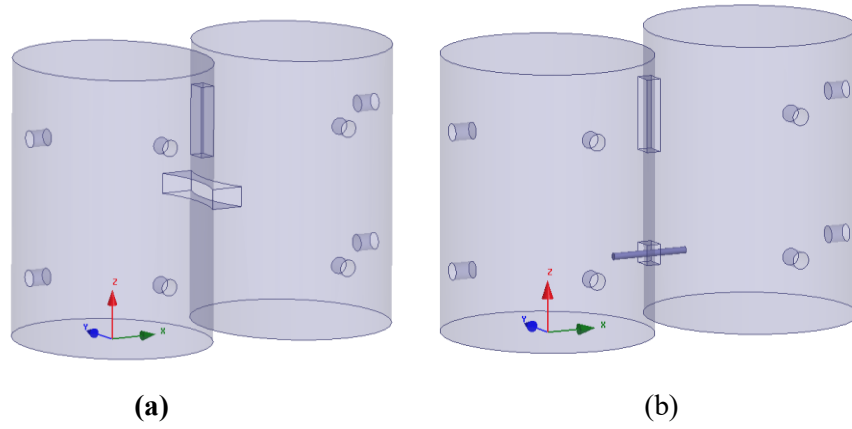
Figure 5.3.3 (a) Iris-iris configuration, (b) iris-probe configuration, (c-d) *H*-field of iris-iris configuration, and (e) *E*-field of iris-probe configuration.

5.3.4 Initial Dual-Band Filter Design

In order to prove the feasibility of the proposed approach, an 8-pole C-band dual-band filter is designed using *HFSS*. The center frequencies of the two pass-bands are at 3.435 and 3.565 GHz respectively and the BW of both bands is 36 MHz. The coupling matrix of the dual-band filter is synthesized as (5.5) based on the approach reported in chapter 3. Both channels are normalized to 3.50 GHz in the matrix.

$$
M = \begin{bmatrix}
0 & 1.138 & 0 & 0 & 0 & 1.145 & 0 & 0 & 0 & 0 \\
1.138 & -3.48 & 0.979 & 0 & -0.132 & 0 & 0 & 0 & 0 & 0 \\
0 & 0.979 & -3.22 & 0.812 & 0 & 0 & 0 & 0 & 0 & 0 \\
0 & 0 & 0.812 & -3.22 & 0.979 & 0 & 0 & 0 & 0 & 0 \\
0 & -0.132 & 0 & 0.979 & -3.47 & 0 & 0 & 0 & 0 & 1.138 \\
1.145 & 0 & 0 & 0 & 0 & 3.54 & 1.009 & 0 & -0.132 & 0 \\
0 & 0 & 0 & 0 & 0 & 1.009 & 3.28 & 0.842 & 0 & 0 \\
0 & 0 & 0 & 0 & 0 & 0 & 0.842 & 3.28 & 1.009 & 0 \\
0 & 0 & 0 & 0 & 0 & -0.132 & 0 & 1.009 & 3.53 & 1.145 \\
0 & 0 & 0 & 0 & 1.138 & 0 & 0 & 0 & 1.145 & 0
\end{bmatrix}
\tag{5.5}
$$

The designed dual-band filter assembly is comprised of 4 major parts and was manufactured with copper material as shown in Figure 5.3.4.1. Figure 5.3.4.2 shows the measured near-band responses of the proposed filter compared with the HFSS simulation. The measured *RL* is better than 24 dB. The measured rejection is over 35dB at the low and high side of the passbands, and is over 30dB between the passbands. The measured *IL* at center frequencies of the two channels is 0.55 and 0.65 dB worse than the simulated *IL* 0.25 and 0.30 dB. The degradation of *IL* is mostly due to the imperfect surface finishing and the use of un-plated screws for tuning. The measured out-of-band responses are shown in Figure 5.3.4.3. The low side TM_{011} mode is located at around 3.24 GHz and has a spurious level lower than 35dB. The high side degenerated TE_{211} mode spurious start rising at 3.75 GHz. The spurious level can be suppressed by modifying the cavity configuration or adding a cover filter.
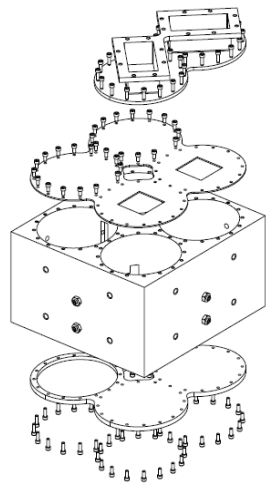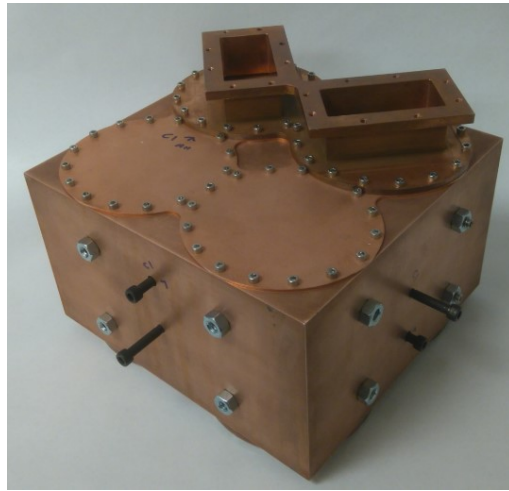
| (a) | (b) |

Figure 5.3.4.1. (a) Explosive view, and (b) integrated assembly of the 8-pole elliptical cavity dual-band filter.
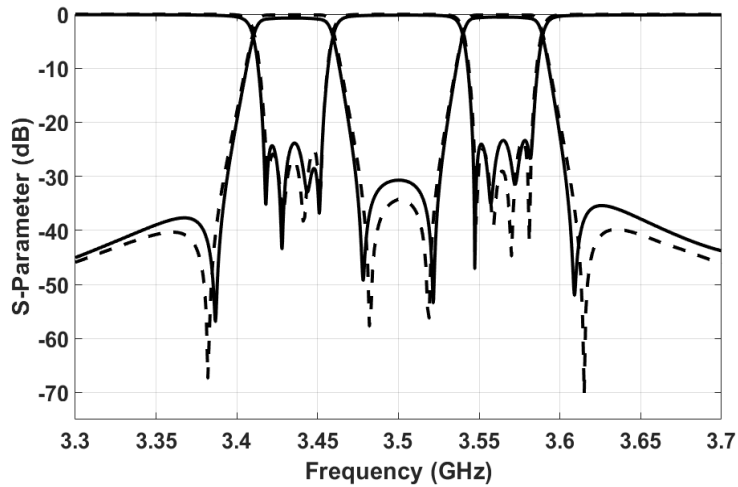
Figure 5.3.4.2. Near-band responses of the 8-pole dual-band cavity filter (fixed line: measurement; dash line: simulation).
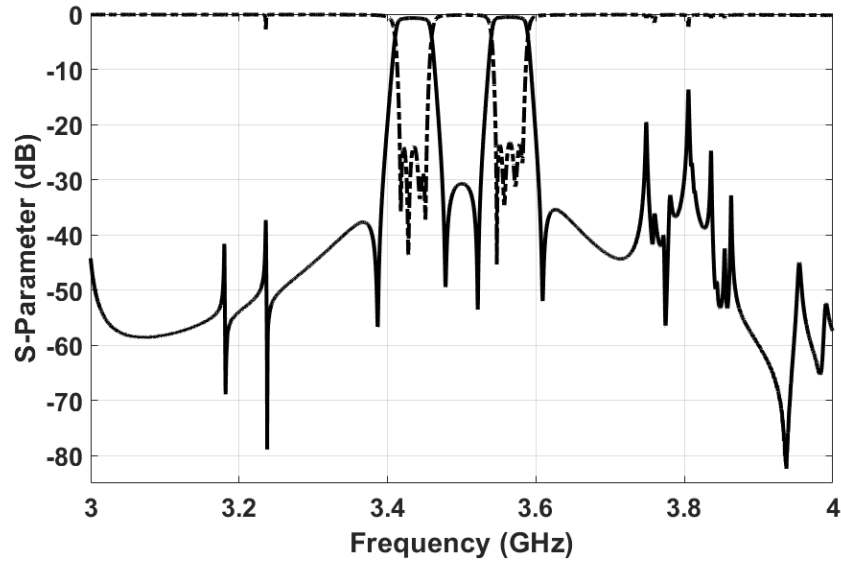
Figure 5.3.4.3. Measured out-of-band responses of the 8-pole dual-band cavity filter (fixed line: S_{21}; dash line: S_{11}).

5.3.5 All-Iris Dual-Band Filter Design

The use of metallic probe (with Teflon support) increases complexity of the assembly and difficulty for tuning. It also raises high power related concern. In Figure 5.3.5.1 (a), the metallic probe produces electrical coupling that has a different coupling sign from that of the irises. The iris slot is referred as short iris since the length of the iris is less than half the free-space wavelength (below resonance). In [67], the concept of long iris was reported having a length longer than half of the free-space wavelength (above resonance). The long iris can provide a different coupling sign from the short iris (i.e. the same coupling sign as the electrical probe) thus providing possibility to realize the all-iris design for the proposed dual-band filter.

Figure 5.3.5.1 (a) shows the original iris-probe combination for the intra-cavity side-coupling of the dual-band filter. The vertical iris along the Z orientation locates at one-quarter / three-quarter height (i.e. maximum H-field) of the resonator and aims to couple the Y-oriented (E-field) TE_{112} mode. The electric

probe along with X orientation also locates at one-quarter / three-quarter height of the resonator (i.e. maximum E-field) to provide electric coupling for the X-oriented (E-field) TE_{112} mode.

Figure 5.3.5.1 (b) shows the proposed long-iris coupling configuration. The long iris is located near the half height of the cavity. In this case, the length of the long iris is ~90 mm and the width is 7.4 mm. The long iris could be straight, or bent from both ends (form a "C" shape) to minimize the stray-coupling leakage to other cavities. The de-normalized coupling values for both cases are summarized in Table 5.3. It is clear from the table that the long iris has the same coupling sign and the all iris configuration provides the same coupling strength as the iris-probe configuration. It is worth to note that due to the different loading effect from long iris and probe, the dimensions of the cavities and the short iris need to be adjusted to realign the resonant frequencies.

The 8-pole filter employing long and short irises is designed in HFSS as shown in Figure 5.3.5.2. The long irises are realizing negative couplings M_{34} in the first channel and M_{23} in the second channel respectively. The simulated response of the all-iris design is compared with that of the initial iris-probe design in Figure 5.3.5.3. The in-band and out-of-band performances of the two designs match well with slight variations. This is due to different frequency dispersion and loading impact between the metallic probes and the long irises.

<p align="center">(a)   (b)</p>
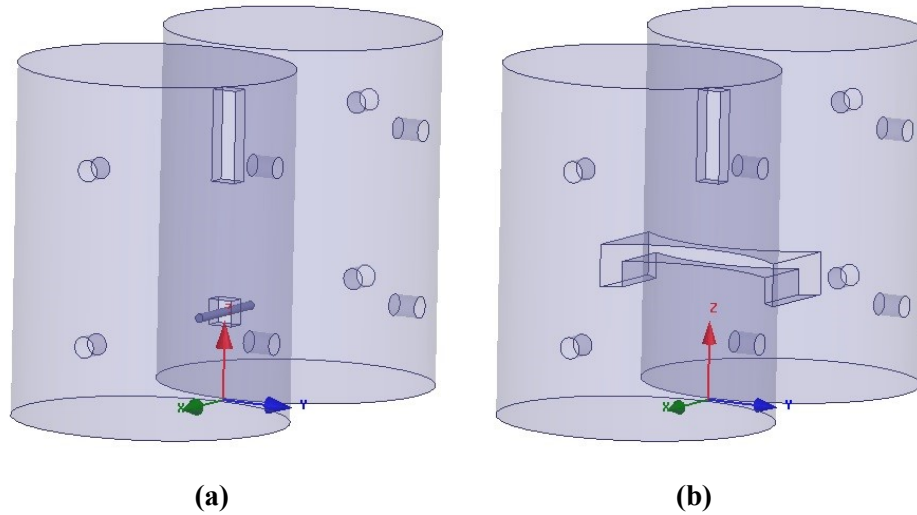
Figure 5.3.5.1. Intra-cavity coupling by (a) iris-probe configuration and (b) all-iris configuration.

Table 5.3 Intra-cavity Coupling Coefficient

Items	Iris-probe configuration (Figure 4(a))	All-iris configuration (Figure 4(b))
Short iris dimensions	29.5×7.6 mm^2	29.1×7.6 mm^2
Probe length	29.5 mm	-
Long iris dimensions	-	89.4×7.4 mm^2
f_i (GHz)	$f_1 = 3.545$ $f_2 = 3.509$ $f_3 = 3.576$ $f_4 = 3.613$	$f_1 = 3.588$ $f_2 = 3.551$ $f_3 = 3.577$ $f_4 = 3.614$
k_i	$k_1 = -0.010$ $k_2 = 0.010$	$k_1 = -0.010$ $k_2 = 0.010$
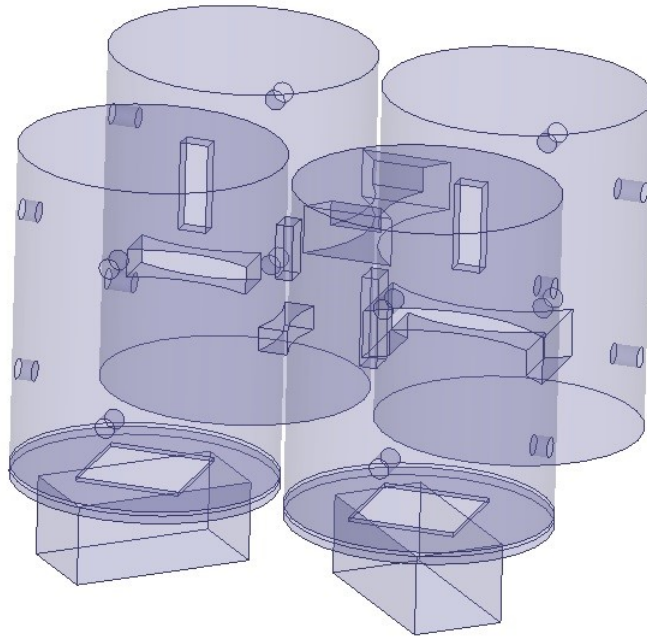
Figure 5.3.5.2. Internal layout of the proposed all-iris 8-pole dual-band filter.
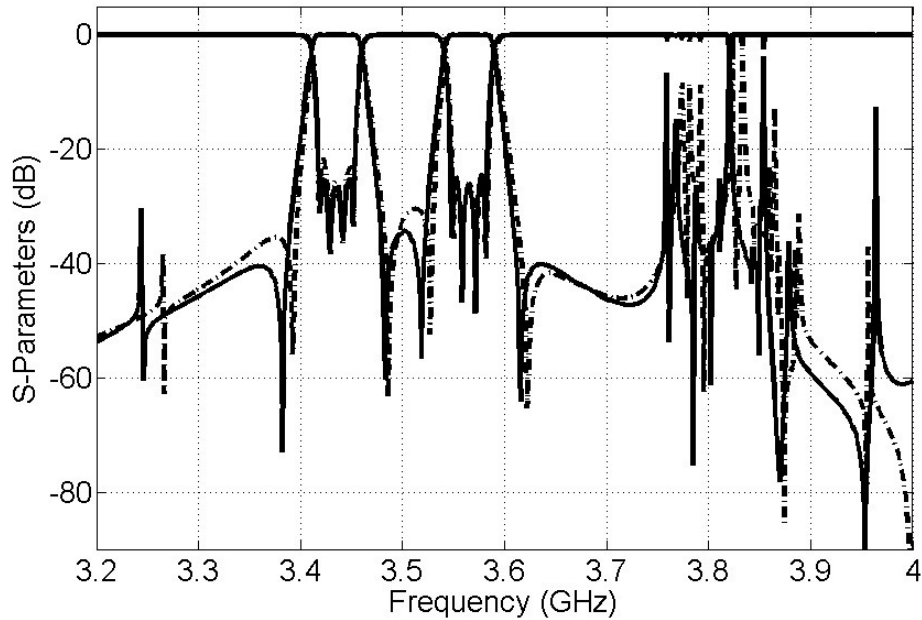
Figure 5.3.5.3. Comparison of out-of-band responses of the 8-pole dual-band cavity filters (fixed line: all-iris configuration; dash line: probe-iris configuration).

5.3.6 All-Iris Dual-Band Filter Design with Spurious Suppression

As can be seen from Figure 5.3.5.3, the high-side TE_{221} spurious is close to the passband, degrading the out-of-band performances. A modification of the cavity is proposed to further improve the spurious-free window. As shown in Figure 5.3.6.1, an elliptical ring with a width W and depth D is undercut from the center of the cavity. Figure 5.3.6.2 illustrates the frequency drift of the TM_{011}, TE_{112} and TE_{211} modes with the change of D. It is observed that with the increase of D, the TM_{011} mode frequency decreases and the TE_{211} mode frequency increases. The ring depth D has relatively small impact on the dual TE_{112} modes because of their low E-field density near the center of the cavity. The spurious-free window is expected to extend after implementing the cavity modification.
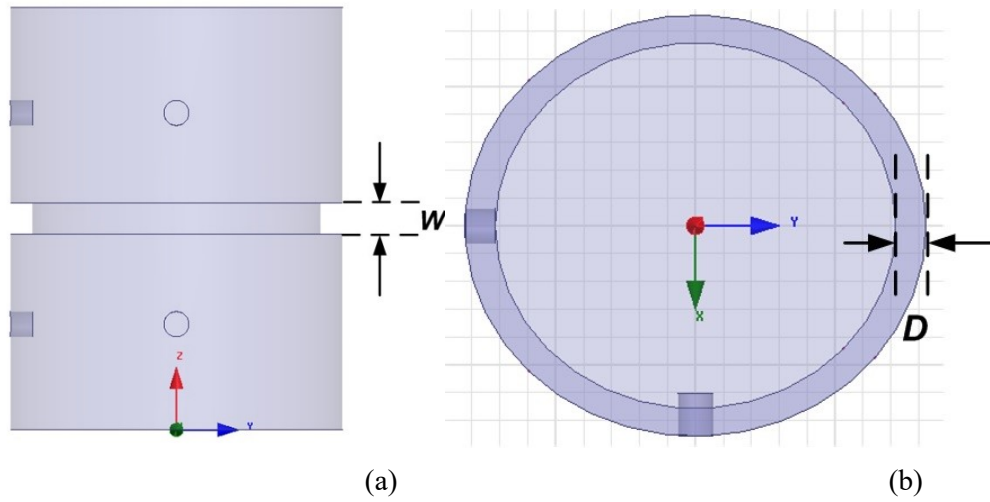
Figure 5.3.6.1. (a) Front view and (b) top view of the modified elliptical cavity.
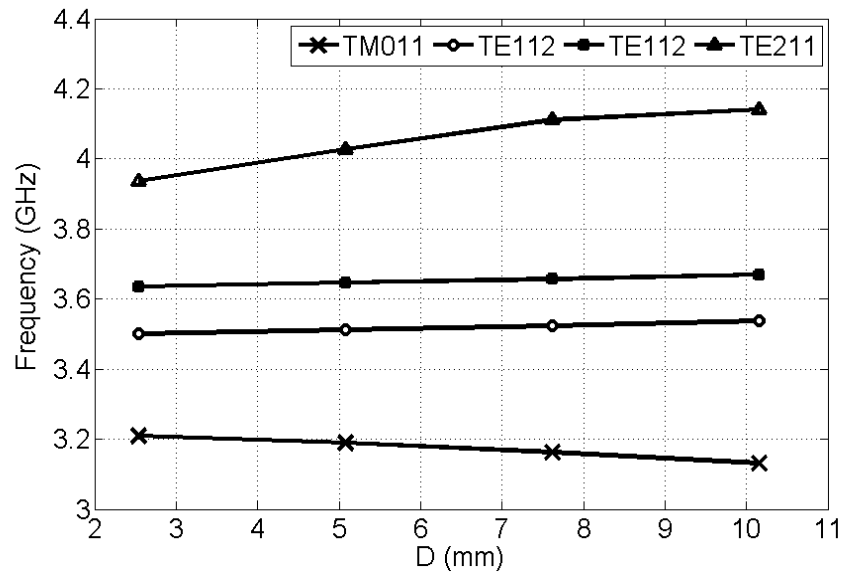
Figure 5.3.6.2. Frequency variation of *TM*$_{011}$, *TE*$_{112}$ and *TE*$_{211}$ modes with change of *D*.

As mentioned earlier, the TM_{011} mode can hardly propagate inside the filter structure through the input/output coupling window, however a small spike can still be noticed at the lower side of the passband in Figure 5.3.5.3, which might deteriorate the stop band performance. A method in [68] is presented the high order spurious can be suppressed by setting the spurious resonating at different frequencies. The approach can be applied in the proposed filter structure by inserting tuning screws through the end-cavity wall. With different penetration of the tuning screw in the cavities, the TM_{011} mode in each cavity resonates at different frequencies thus suppressing each other to achieve improved stop-band responses. The end-cavity screws have minimum impact to the TE_{112} mode.

The degenerated dual TE_{211} modes operate at different frequencies and are semi-orthogonal in the elliptical cavity. The electrical vector (x-y plane) and magnetic field (y-z plane) of the TE_{211} mode 1 and TE_{211} mode 2 are shown in the Figure 5.3.6.3. At the center of cavity where the side-coupling iris located, the TE_{211} mode 1 has minimum magnetic field density while TE_{211} mode 2 has maximum magnetic field density with the magnetic vector along Z-axis, thus the horizontal side-coupling iris at the cavity center has minimum coupling to the both TE_{211} modes. On the other hand, the vertical iris located at one or three-quarter of the cavity (see Figure 5.3.6.3 (a) and (c)), has minimum coupling to TE_{211} mode 1, while having no rejection to the TE_{211} mode 2. In [69], a pair of peripheral iris locating at 135° and 225° (see Figure 5.3.6.3 (b) and (d)) in azimuthal direction was introduced to suppress the TE_{211} mode 2; however they have no rejection to TE_{211} mode 1. Figure 5.3.6.4 shows the proposed coupling configuration with a combination of peripheral vertical iris pair and center vertical single iris. The two pairs of peripheral irises are applied between cavity 1~2 and cavity 3~4, while the single vertical iris are set between cavity 2~3 and 1~4. Such design can effectively suppress both degenerated TE_{211} modes while still being able to transmit the operational TE_{112} modes.

The new iris configuration from Figure 5.3.6.4 and the cavity modification from Figure 5.3.6.1 are implemented in the side-coupled filter structure. Figure 5.3.6.5 illustrates a comparison of the out-of-band responses between the original structure and the structure with the spurious suppression fixtures. An obvious improvement of the stop-band rejection is noticed from the updated structure.

(a)   **(b)**

(c)   **(d)**
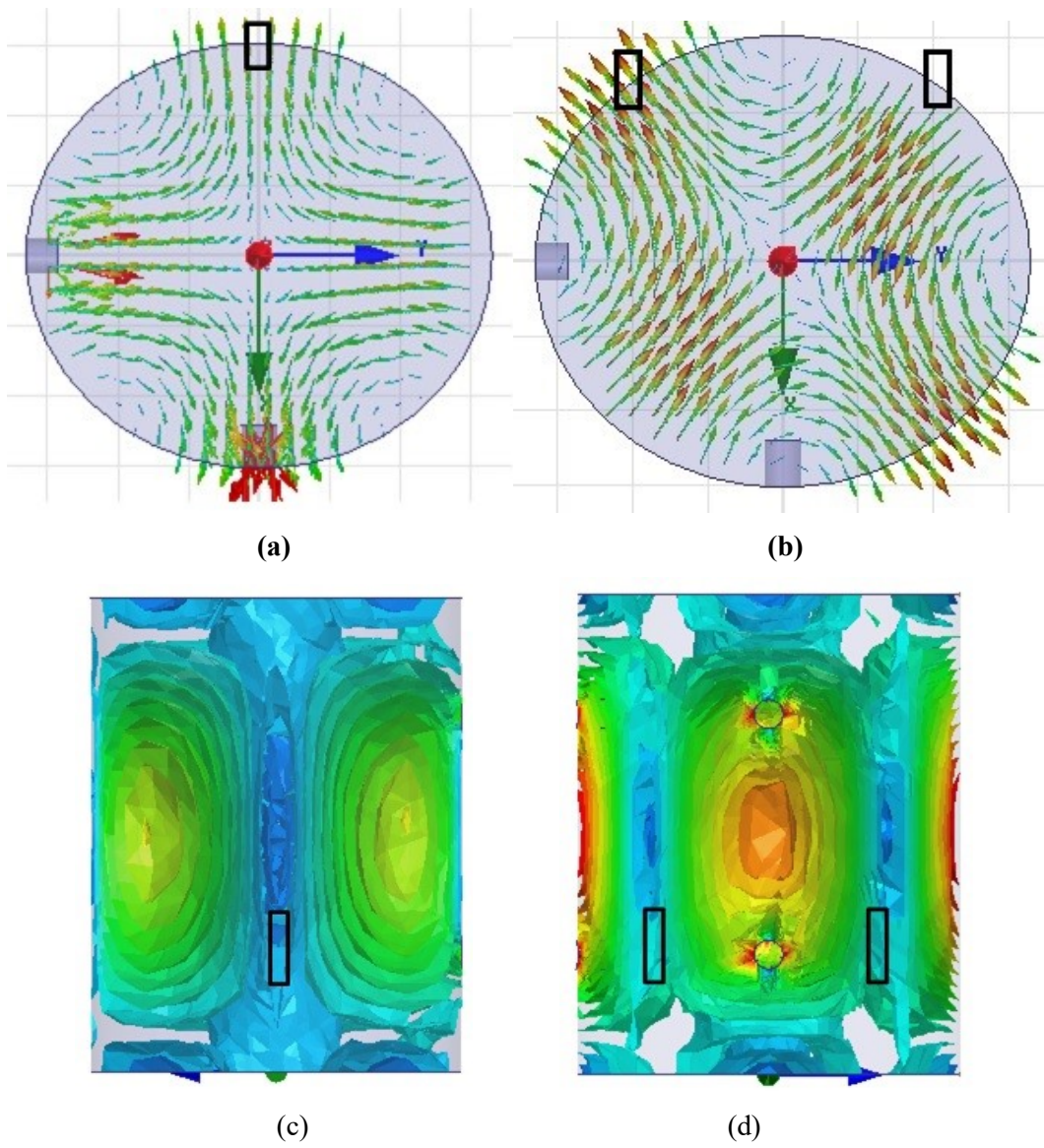
Figure 5.3.6.3. (a) E-field vector of TE$_{221}$ mode 1, (b) E-field vector of TE$_{221}$ mode 2, (c) H-field of TE$_{221}$ mode 1, and (d) H-field of TE$_{221}$ mode 2.
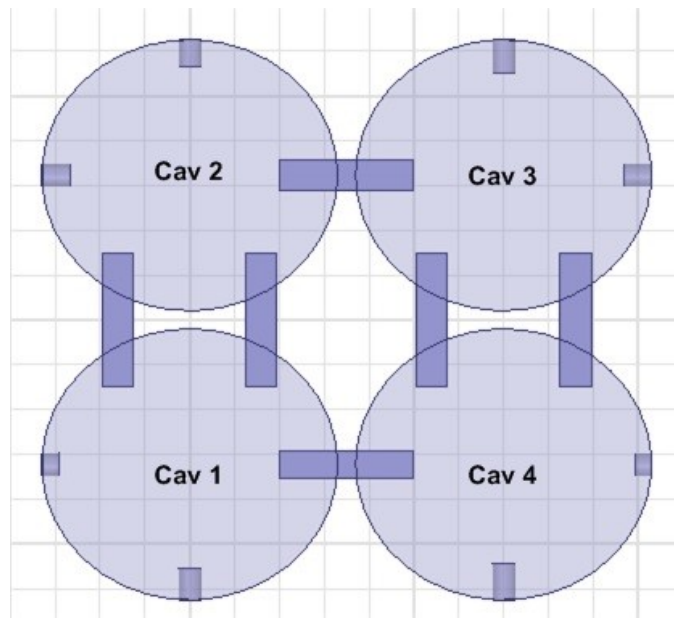
Figure 5.3.6.4. Proposed iris configuration to suppress the *TE*$_{211}$ spurious modes
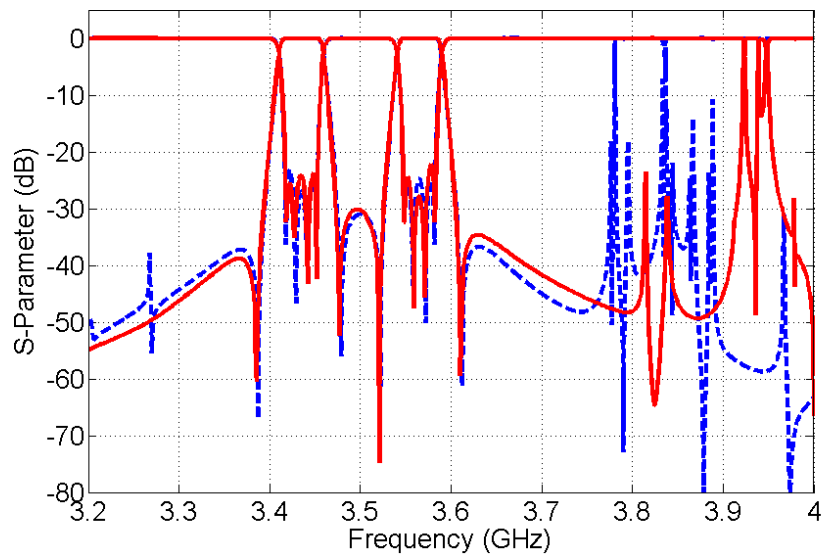
Figure 5.3.6.5. Comparison of out-of-band responses of the 8-pole dual-band cavity filters (red fixed line: with spurious suppression fixture; blue dash line: without spurious suppression fixture).

5.3.7   Analysis of Bandwidth Realization of the side-coupled configuration

The proposed all-iris design simplified the filter structure thus reducing the cost from machining and tuning; however it is observed the magnetic coupling provided by the horizontal iris near the cavity center is considerably weaker compared to the electric coupling provided by the metallic probe. This results in a limitation of bandwidth realization from the all-iris design.

As a baseline, Figure 5.3.7.1 demonstrated the relationship between the probe length L and the electrical coupling while the probe is located at one quarter or three-quarter height of the cavity. The longer the probe, the stronger electric coupling can be achieved. It is worth noting that the probe also generates an over-mode locating at the high side of the passband. The frequency of the over-mode decreases, (i.e. moves towards the passband) when the length of the probe increases. It is recommended to maintain the frequency of the "probe over-mode" close to other high-side over-modes from the cavities. In this case, when the length of probe is 33.5 cm, the "probe" spurious mode is at 3.82 GHz, close to the spurious TE_{221} mode at 3.83 GHz.
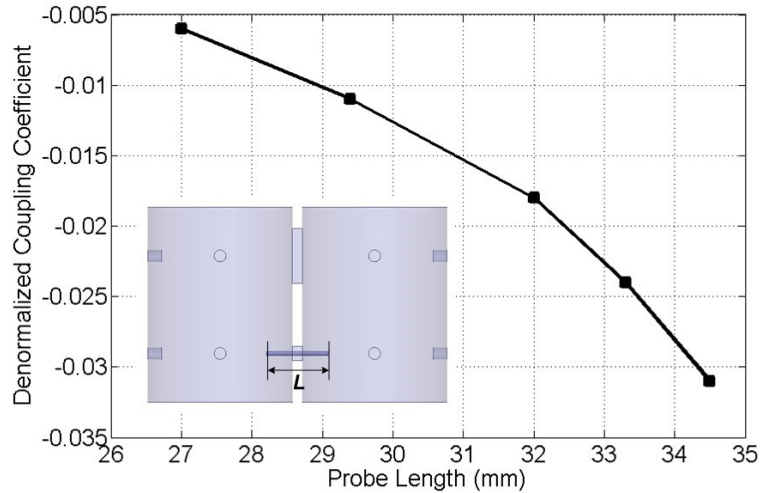
Figure 5.3.7.1. Denormalized coupling coefficient vs. metallic probe length *L*.

The horizontal iris located at the half height of the cavity is aiming to replace the metallic probe. The relationship between the length X of the horizontal iris and the magnetic coupling is illustrated in Figure 5.3.7.2. When X approaches to half of the free space wavelength, the phase of the magnetic (positive) coupling flips by 180 degrees, acting as a pseudo-electric (negative) coupling. From an *EM* eigen-mode

simulation, when the iris length gets around 45.7cm, two magnetic modes (when magnetic wall applied on the symmetric plane) are observed on either side of the electric mode (when electric wall applied on the symmetric plane). The electric-field and the corresponding frequency of each mode is shown in Figure 5.3.7.3. Two coupling coefficients can be calculated respectively as per (5.6),

$$k_1 = \frac{f_e^2 - f_{m1}^2}{f_e^2 + f_{m1}^2} = 0.038, \qquad k_2 = \frac{f_e^2 - f_{m2}^2}{f_e^2 + f_{m2}^2} = -0.038 \qquad (5.6)$$
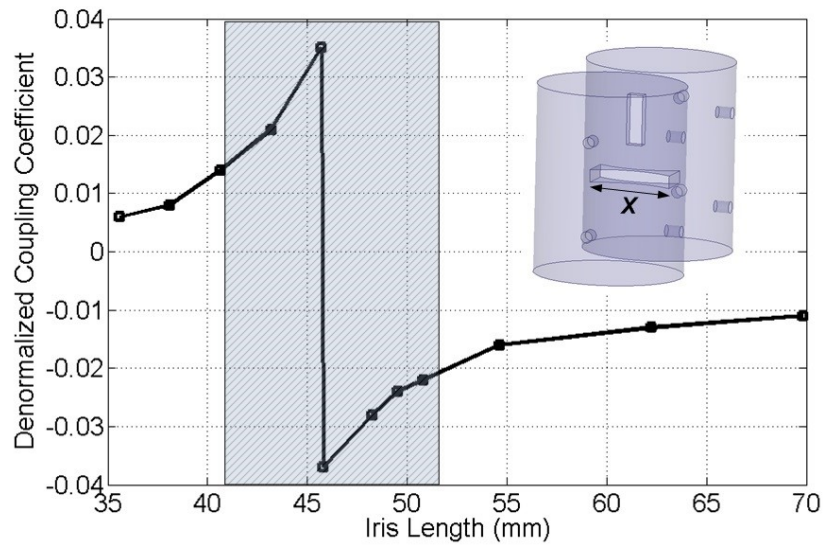
Figure 5.3.7.2. Denormalized coupling coefficient vs. horizontal iris length X (▨ mutation area)
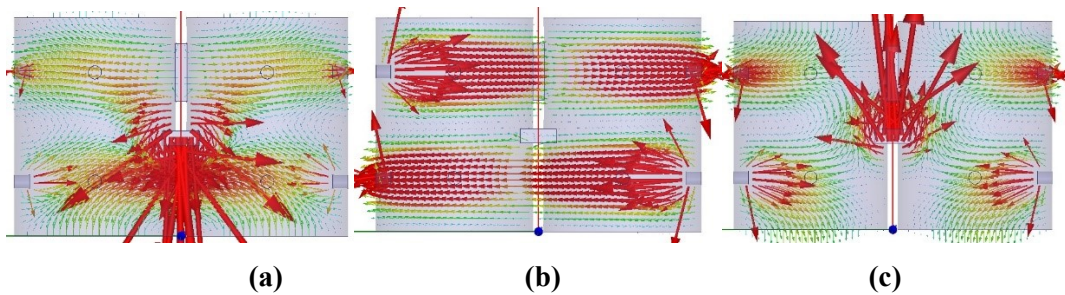
Figure 5.3.7.3. (a) Low side magnetic mode f_{m1} @ 3.421 GHz, (b) electric mode f_e @ 3.552 GHz, and (c) high side magnetic mode f_{m2} @ 3.689 GHz.

The two couplings k_1 and k_2 have different sign thus tend to cancel each other. This results in a mininum (null in theory) overall coupling between the two cavity modes. In practice, the iris length is suggested to be chosen considrablely far from the mutation area to avoid a high sensitivity of the coupling amount. As shown in Figure 5.3.7.2, when the iris length is longer than half of the wavelength, the magnitude of the pseudo-electric coupling is inversely proportional to the iris length. In this case, the maximum achievable coupling (outside the mutation zone) from the horizontal iris is around -0.020, smaller than what can be achieved from probe.

The width of the horizontal iris also affects the coupling and their relationship is shown in Figure 5.3.7.4. The coupling strength is proportional to the iris width W however the slope gradually decrases with the increase of the iris width. The relationship between the height of the iris and the coupling is shown in Figure 5.3.7.5. It indicates the coupling has the maximum strength at the half height of the cavity and decreases when the location offsets from the center.

For the 8-pole all-iris design expressed by the coupling matrix in (5.5), it has been observed from the simulation that the maximum realizable percentage bandwidth is around 1.2% (<42 MHz @ 3.5 GHz). The threshold parameter is the center horizontal iris as analyzed above.
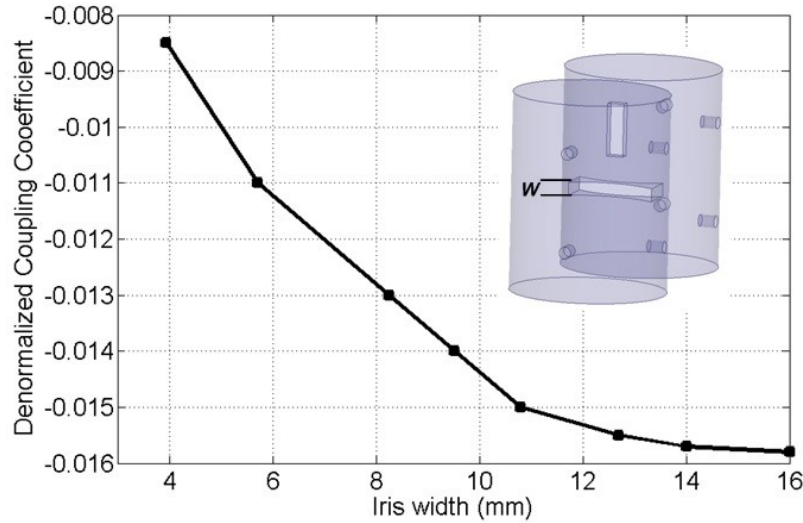
Figure 5.3.7.4. Denormalized coupling coefficient vs. horizontal iris width W.
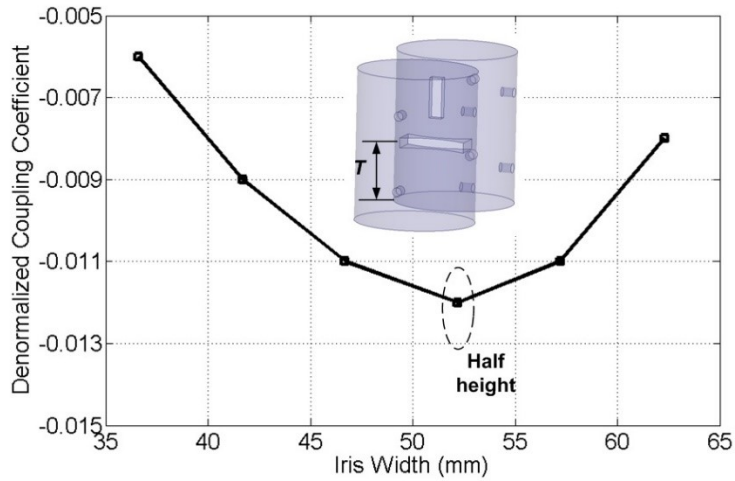
Figure 5.3.7.5. Denormalized coupling coefficient vs. horizontal iris height *T*.

5.3.8 All Iris Dual-band Filter with Wide BW

Compared to the side-coupled iris, the end-coupled iris is capable to produce stronger coupling thus becomes a solution for the dual-band design with a wide bandwidth. Figure 5.3.8.1 shows the relationship between the denormalized coupling coefficient and the length X of the end-coupled iris. A considerably higher coupling can be achieved by the end-coupled iris compared to that from the side-coupled iris. Another advantage of using end couplings is they do not generate extra over-modes close to the passband. This also benefits the wide band design.

The target bandwidth for the wide-band design is 60 MHz and the channel center frequencies are 3.4 and 3.6 GHz. Figure 5.3.8.2 shows the internal layout of the 8-pole wide-band dual-band filter. The structure uses a combination of end-coupled and side-coupled resonators implementing of the block diagram in Figure 5.3.1.1. The end-coupled irises featuring stronger coupling are employed to realize M_{12} and M34 for two channels, while the side-coupled irises are realizing M_{14} and M_{23} for both channels.
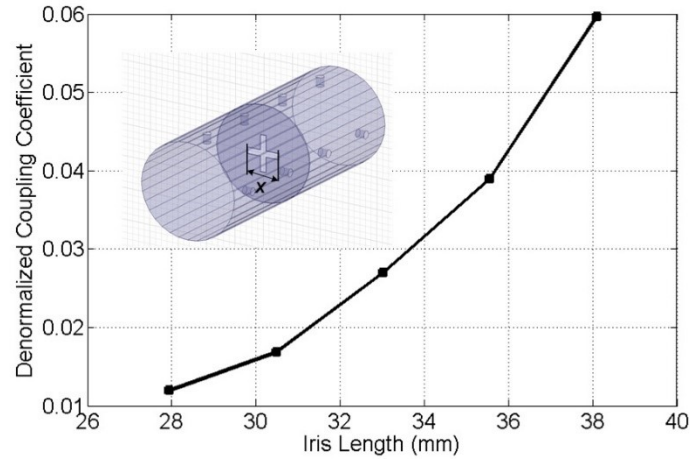
Figure 5.3.8.1. Denormalized coupling coefficient vs. end-coupled iris length *X*.
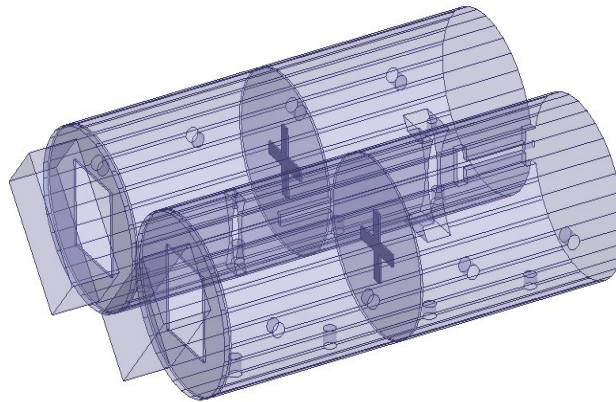
Figure 5.3.8.2. Internal layout of the proposed wide-band 8-pole dual-band filter.

The designed wide-band dual-band filter assembly is comprised of 6 parts (including 3 irises) and was manufactured with aluminum material as shown in Figure 5.3.8.3. Figure 5.3.8.4 shows the measured out-of-band responses of the proposed filter compared with the *HFSS* simulation. The measured *RL* is around 25 dB. The measured *IL* at center frequencies of the two channels is 0.35 and 0.42 dB worse than the simulated *IL* 0.15 and 0.20 dB. The degradation of *IL* is mostly due to the imperfect surface finishing and the use of un-plated housing and screws. The measured rejection is over 30 dB between

the passbands and is over 35 dB at the low side of the passbands. The high side rejection is worse than that from simulation due to the spurious TE_{211} mode at 3.78 GHz.

(a)   (b)
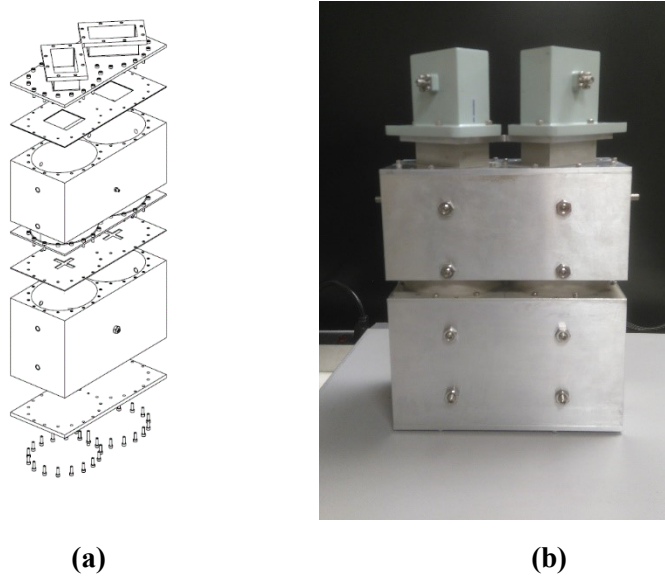
Figure 5.3.8.3.   (a) Explosive view of the wide-band dual-band filter assembly and (b) manufactured wide-band dual-band filter assembly.
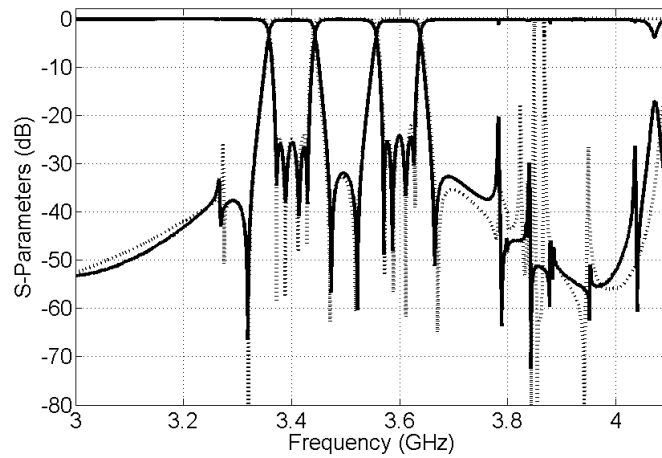
Figure 5.3.8.4. Out-of-band responses of the 8-pole wide-band dual-band cavity filter (fixed line: measurement; dash line: simulation).

As shown in Figure 5.3.8.5, the elliptical cavity of the wide-band dual-band filter is also modified to improve the spurious-free window. Figure 5.3.8.6 illustrates the improvement of out-of-band performances after implementing the cavity modification. The low side TM_{011} spurious disappears and the high side TE_{211} spurious starts to rise at 3.84 GHz. The measured spurious level is expected to be even lower than the simulated responses due to the limited Q of the spurious modes.
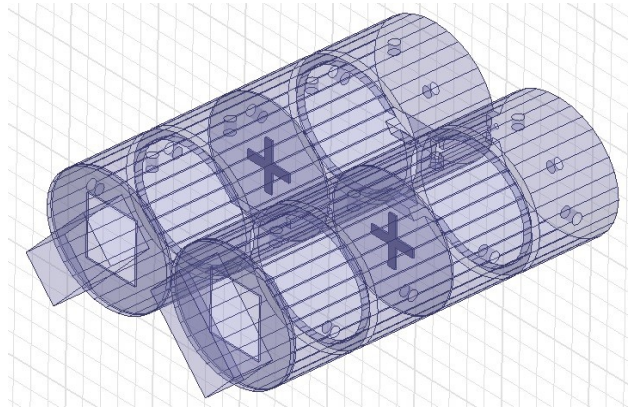
Figure 5.3.8.5. Internal layout of the proposed wide-band 8-pole dual-band filter with cavity modification.
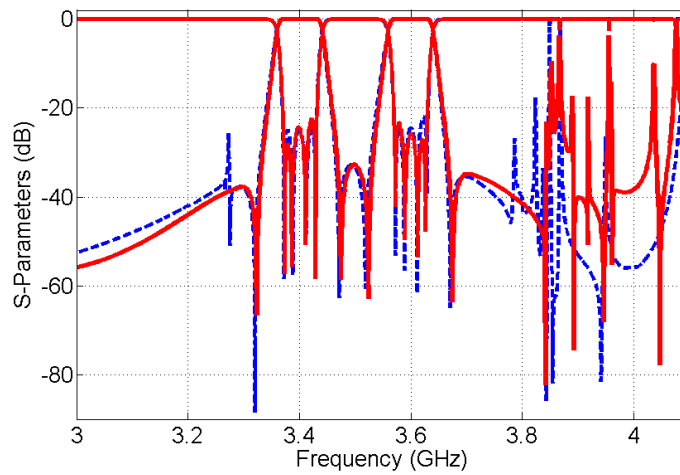
Figure 5.3.8.6. Comparison of out-of-band responses of the 8-pole wide-band dual-band cavity filters (red fixed line: with cavity modification; blue dash line: without cavity modification).

5.4　Conclusion

The chapter has first presented a unique dual tri-section structure consists of dual-band and single-band rectangular waveguide cavities that result in dual-band filter and diplexers of compact size, high Q, multiple transmission zeros and improved spurious response. All features have been experimentally validated by an 8-pole Ku-band diplexer. Secondly, a novel folded configuration of dual-band bandpass filter based on dual-mode elliptical cavity resonators has been presented. The dual-quadruplet module offers a further reduced footprint compared to many previous reported structures and generates a pair of transmission zeros for each of the passband by only inductive iris. Approaches to improve the out-of-band spurious response and bandwidth limitation have been discussed and considerable improvement has been observed from the *EM* simulation. The design concept has been validated by two 8-pole C-band prototypes. The proposed filter configuration can be easily extended to higher order-filters while still maintaining a compact size.

Chapter 6

Waveguide Triple-Band Bandpass Filters

6.1   Introduction

In this chapter the previous design concept of dual-band filter is extended to triple-band filter within a similar waveguide cavity structure. The design complexity dramatically increased from the following aspects:

- The triple-mode cavity resonator is more difficult to design because the three modes need to be managed operating in three different designated frequencies and the mutual-coupling between any modes need to be as small as possible for this application.

- The spurious-free window of triple-mode resonator is more challenging to maintain because of the employment of more higher-order modes.

- The coupling mechanism is more difficult to realize for the triple-mode resonator because the configuration need to feed three signal paths simultaneously and have the capability to control the power distribution to the three modes.

- The realization of transmission zeros in the triple-band filter become extremely challenging because of the difficulty to establish cross-coupling paths respectively for each channel besides the sequential-coupling paths.

-

6.2   Triple Band Filter with Elliptical Resonator

6.2.1   Elliptical Triple-mode Resonator

In chapter 4 and 5, elliptical cavities have been used to realize dual-mode resonator for the applications of dual-band bandpass filter. In this chapter, the elliptical cavity is employed to realize a triple mode resonator for the first time. The operating modes in the elliptical cavity are the degenerated TE_{111} modes and the TM_{010} mode as shown in Figure 6.2.1.

(a)   (b)

(c)   (d)   (e)
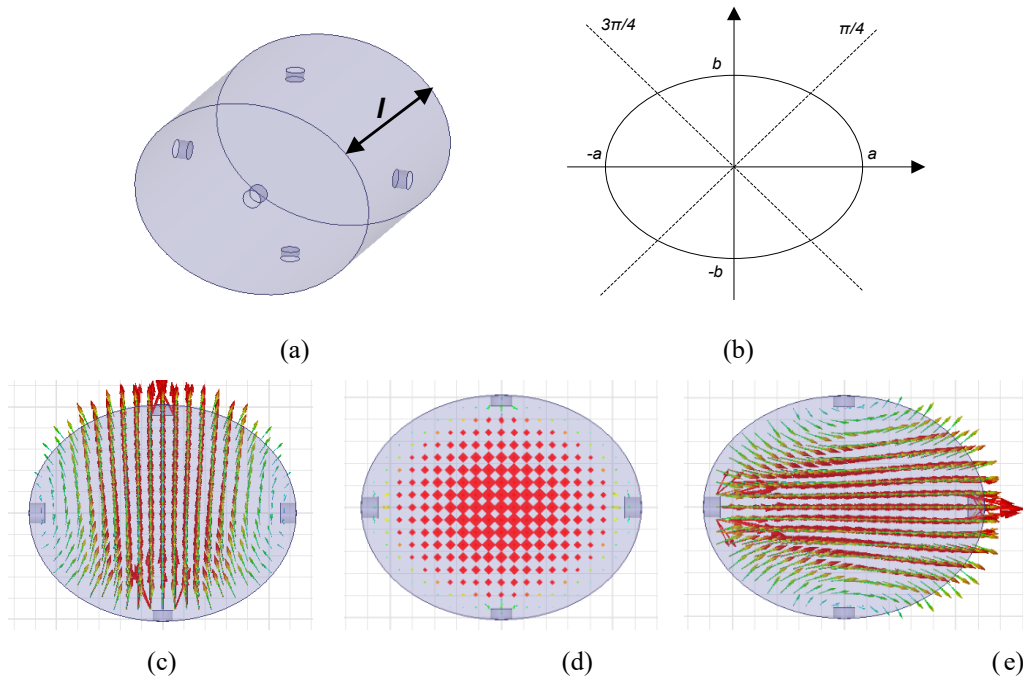
Figure 6.2.1. (a) Elliptical triple-mode resonator layout, (b) transversal cross-section of the elliptical cavity, and (c, d, e) electrical field vector of TE_{111_V}, TE_{111_H}, and TM_{010} modes.

The triple resonators in each cavity can be tuned at specified frequencies by a proper combination of two diameters a, b along the two elliptical axes and the cavity length l. The three polarized modes are orthogonal resulting extra degree of isolation and to be designed to carry three passband signals. The resonant frequencies of the three modes in the elliptical resonator can be approximately calculated by equations (6.1) ~ (6.3),

$$f_{TE_{111\_V}} \approx \frac{c}{2\pi} \sqrt{(\frac{p'_{11}}{a})^2 + (\frac{\pi}{l})^2} \,, \tag{6.1}$$

$$f_{TE_{111\_H}} \approx \frac{c}{2\pi} \sqrt{(\frac{p'_{11}}{b})^2 + (\frac{\pi}{l})^2} \,, \tag{6.2}$$

$$f_{TM_{010}} \approx \frac{c}{2\pi} \frac{p_{01}}{\sqrt{ab}} \,, \tag{6.3}$$

where c represents the speed of light, and p'_{11} and p_{01} represent the first roots of Bessel functions for TE_{11} and TM_{01} modes respectively. From the equations, the frequency differentiations among the three polarized modes are generally determined by the ratio of a, b and l. Tuning screws along corresponding polarized directions can be added to provide extra degrees of controlling the three polarized frequencies.

By performing an eigenmode analysis with full-wave *EM* software, resonant modes can be calculated in the elliptical triple-mode cavity. For cavity dimensions of a = 1.26", b = 1.02", and l = 2.45", and considering a structure made of copper, the resonant frequencies and the unloaded Qs are listed in Table 6.1. In our case the first three modes are of interest. The adjacent modes TM_{010} and TM_{011} are nearly 550 MHz higher, yielding an acceptable spurious-free window. In the elliptical cavity in Figure 6.2.1(a), tuning screws are located along vertical, horizontal and zenith axes, providing the flexibility to adjust the resonant frequencies of each band. The three modes in the elliptical triple-mode cavity are considered to be not coupled (A weak coupling does exist when frequencies of the three modes are close). Intra-coupling only happens between adjacent cavities by modes with the same *E*-field orientation. For instance, the horizontal TE_{11m} in cavity *1* will only couple with the horizontal TE_{11m} in cavity *2*. For the first and last cavities, the input and output waveguides excite the three quasi-orthogonal modes in these cavities simultaneously.

Table 6.1 Resonant modes in the elliptical triple-mode cavity

Mode	Frequency (GHz) from Eigen-mode Simulation	Frequency (GHz) from Equations (6) to (8)	Unloaded Q
TE_{111_V}	**3.675**	**3.656**	**18479**
TM_{010}	**4.065**	**3.991**	**18319**
TE_{111_H}	**4.168**	**4.158**	**19963**
TM_{011}	4.728	-	15127
TE_{211}	5.462	-	19264

6.2.2   Inter-Cavity Coupling

The signals in the proposed triple-band filter configuration in Figure 6.2.2.1 are transmitted along three parallel non-interacting paths; hence, inter-cavity coupling only occurs between resonant modes with the same orientation. In this case, a hybrid structure composed of a horizontal iris, a vertical iris and an electrical probe (see Figure 6.2.2.2) is developed to couple three polarizations with minimum interaction and is thus suitable for designs with relatively small guard-band. The horizontal iris, vertical iris and electrical probe are used to couple the TE_{111_V}, TE_{111_H} and TM_{010} modes respectively. The dimensions of the irises and probes are determined by the coupling matrix parameters from all channels. Using Eigen-mode simulation by placing an electric and magnetic wall along the symmetry plane, six eigen-mode frequencies are calculated as shown in Table 6.2. The de-normalized coupling coefficients k_i are then computed by the equations (6.4),

$$k_i = \frac{f_{2i}^2 - f_{2i-1}^2}{f_{2i}^2 + f_{2i-1}^2}, \quad i = 1, 2, 3 \tag{6.4}$$

The ideal coupling mechanism for the triple-band design needs to include adjustable parameters sensitive to only one particular mode / passband. Figs. 6.2.2.2 (a)-(c) show the relationship between each subsection of inner coupling structure and the denormalized coupling coefficients. The results indicate that the horizontal iris is sensitive to the TE_{111_V} mode and the vertical iris is sensitive to the TE_{111_H} mode, while the electrical probe dominates the coupling to the TM_{010} mode. Thus the proposed configuration has a capability of controlling the coupling along the three signal paths individually. It is worth to note that the accuracy of equations (6.4) decreases when the frequencies of the three bands are close to each other's, due to a non-negligible coupling between the three modes in one cavity. The iris openings are designed in a long rectangular shape, aiming to minimize the cross-talk between the polarized modes.

85
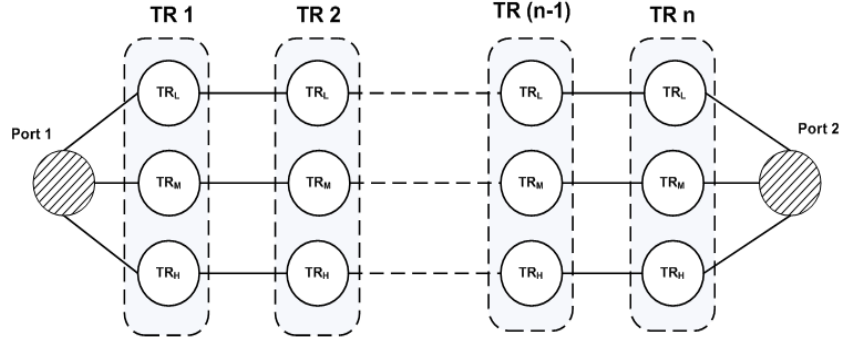
Figure 6.2.2.1. Equivalent circuit of the proposed tri-band filter. (TR: triple-mode resonator).

(a)

(b)

(c)
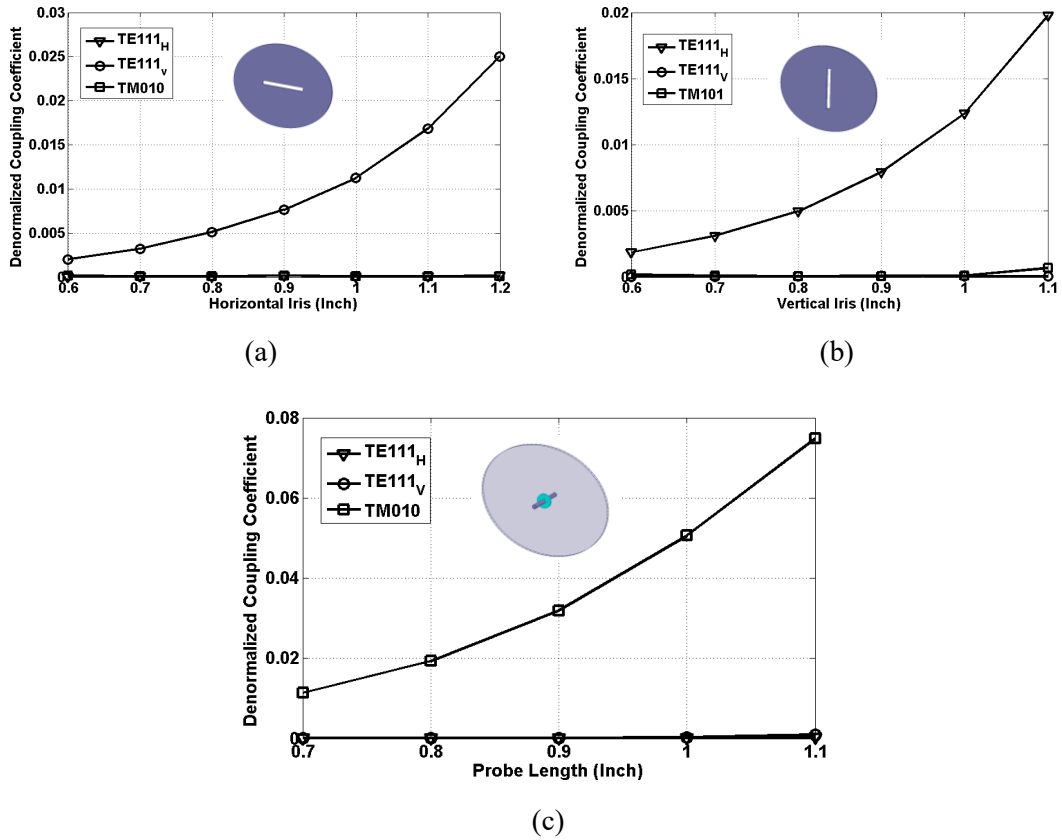
Figure 6.2.2.2. Relationship between inter-cavity coupling coefficients and (a) the horizontal iris L_1, (b) the vertical iris L_2 and (c) the probe length L_3.

Table 6.2

Eigenmode simulation results for inter-cavity Coupling when L_1=0.99 inch, L_2=1.04 inch and L_2 = 0.73 inch

Mode	Eigenmode Frequencies (GHz)	Coupling Coefficients by Equation (6.4)
TE_{111V_Cav1}	$f_1 = 3.615$	$k_1 = 0.0145$
TE_{111V_Cav2}	$f_2 = 3.668$	
TM_{010_Cav1}	$f_3 = 3.972$	$k_2 = 0.0134$
$TM_{010\ Cav2}$	$f_4 = 4.031$	
TE_{111H_Cav1}	$f_3 = 4.082$	$k_2 = 0.0147$
TE_{111H_Cav2}	$f_4 = 4.137$	

6.2.3   Input / Output Coupling

The excitation of multiple modes in a single cavity has always been a significant challenge, especially when the number of passbands exceeds two. Recent reported dual-band cavity filter structures [24] [25] have both modes excited by a tapped probe or a rectangular iris. These coupling structures provide limited independent control of the external Q when dealing with two modes.

A common option of excitation in a rectangular cavity is to use a coaxial cable penetrating perpendicularly inside the cavity to provide coupling to a single mode. For the proposed triple-band filter, a novel "L-shape" coaxial probe is devised, as shown in Figure 6.2.3.1. In this mechanism, four parameters L_1, L_2, ΔL and θ can be tuned to determine the input coupling strength and distribution to the degenerated TE_{111} and TM_{010} modes. Figs. 6.2.3.2 (a)-(d) show the relationship between the parameters and the reflected group delay. In general, L_1 mainly determines the coupling to TE_{111_H} mode, L_2 mainly determines the coupling to TM_{010} mode, ΔL determines the overall coupling to the TE_{111_V} and TE_{111_H} modes, while θ controls the distribution of overall coupling to the two modes. Such a configuration is capable to fully control the input coupling for the three operating modes while keeping the structure simple. In Figs. 6.2.3.3 (a) and (b), three balanced group delay peaks corresponding to the three input couplings are designed with different values at the desired frequencies, which proves an dedicate and flexible control of the external couplings by the proposed structure in Figure 6.2.3.1.

(a) **(b)**
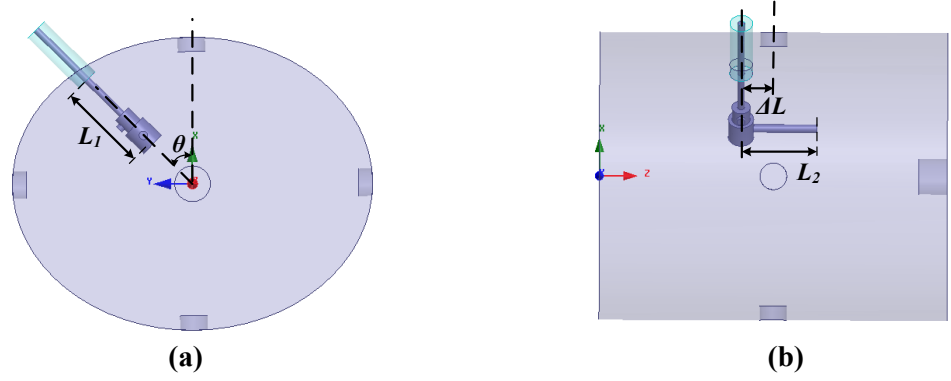
Figure 6.2.3.1. (a) Front and (b) side view of external coupling structure of the elliptical resonator.

(a) **(b)**

(c) **(d)**
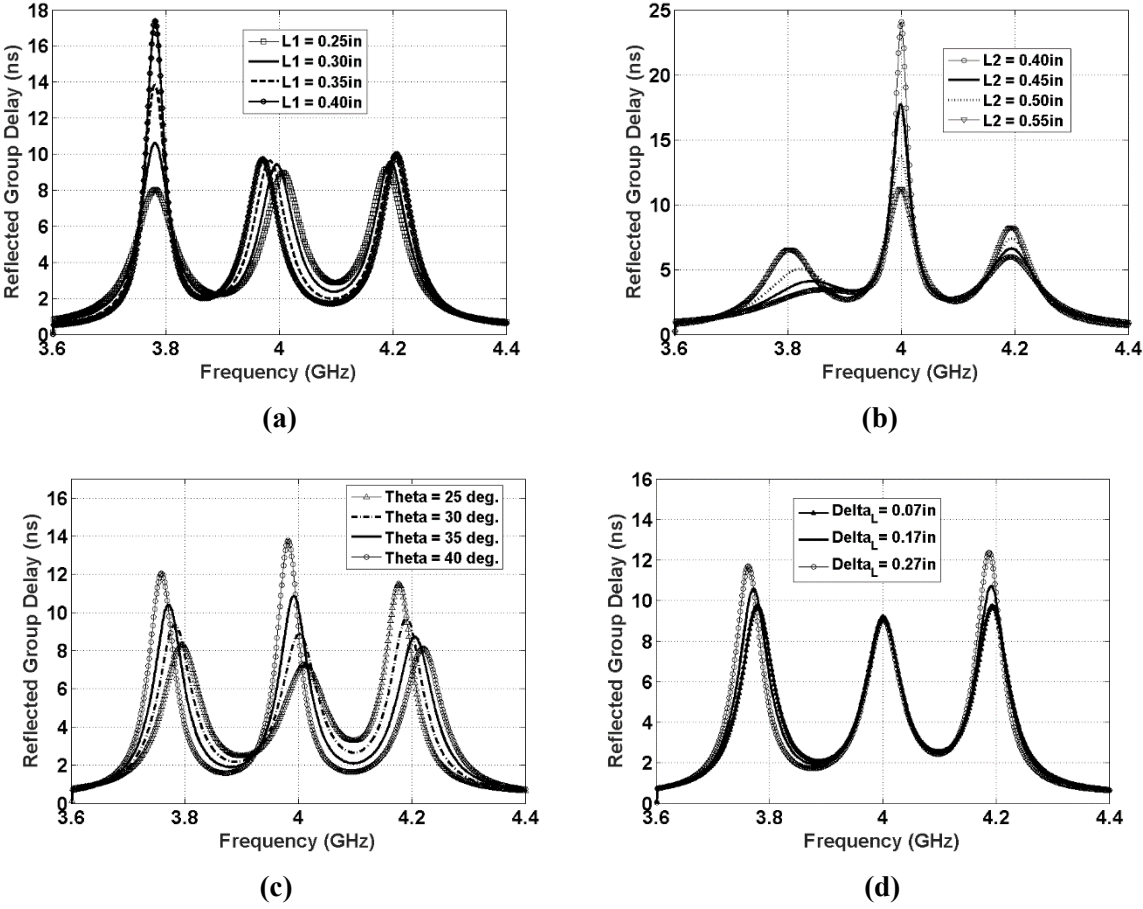
Figure 6.2.3.2. Relationship between reflected GD and (a) L_1, (b) L_2, (c) θ, and (d) ΔL of the probe.

(a)   (b)
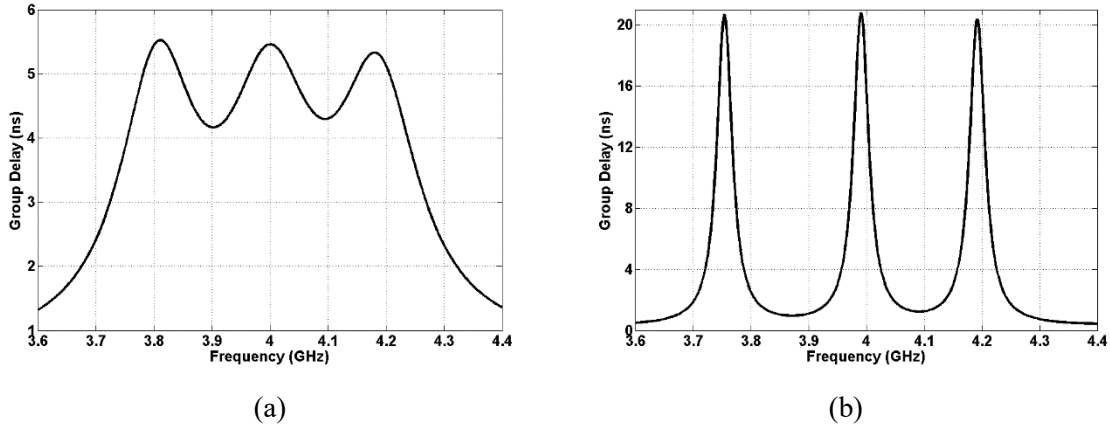
Figure 6.2.3.3. Reflected group delay of (a) 5.5ns and (b) 21ns for the triple-band filter.

6.2.4   Elliptical-cavity Triple-band Filter Design

In order to prove the feasibility of the proposed approach, a 9-pole C-band triple-band filter is designed. Following the procedure in chapter 3, the $3N+2$ ($N=3$) coupling matrix is achieved in (6.5) with a $CF = 4.0$ GHz and $BW = 36$ MHz.

$$M = \begin{bmatrix} 0 & 1.434 & 0 & 0 & 1.331 & 0 & 0 & 1.387 & 0 & 0 & 0 \\ 1.434 & 11.88 & 1.537 & 0 & 0 & 0 & 0 & 0 & 0 & 0 & 0 \\ 0 & 1.537 & 11.41 & 1.537 & 0 & 0 & 0 & 0 & 0 & 0 & 0 \\ 0 & 0 & 1.537 & 11.88 & 0 & 0 & 0 & 0 & 0 & 0 & 1.434 \\ 1.331 & 0 & 0 & 0 & -0.00 & 1.421 & 0 & 0 & 0 & 0 & 0 \\ 0 & 0 & 0 & 0 & 1.421 & 0.00 & 1.421 & 0 & 0 & 0 & 0 \\ 0 & 0 & 0 & 0 & 0 & 1.421 & -0.00 & 0 & 0 & 0 & 1.331 \\ 1.387 & 0 & 0 & 0 & 0 & 0 & 0 & -11.30 & 1.424 & 0 & 0 \\ 0 & 0 & 0 & 0 & 0 & 0 & 0 & 1.424 & -10.83 & 1.424 & 0 \\ 0 & 0 & 0 & 0 & 0 & 0 & 0 & 0 & 1.424 & -11.30 & 1.387 \\ 0 & 0 & 0 & 1.434 & 0 & 0 & 1.331 & 0 & 0 & 1.387 & 0 \end{bmatrix}$$

(6.5)

89

Figure 6.2.4.1 shows the layout of triple-band filter with elliptical cavities based on the above inter-cavity and external coupling concepts. The initial dimensions of each sub-section are achieved by the method introduced in the previous sessions. The initial overall responses (*i.e.* *S*-parameters) of the full passband are then divided into three sub-bands (*e.g.* low: 3.6-3.9 GHz; mid: 3.9~4.1 GHz; high: 4.1~4.4 GHz). Each of the sub-band response can be optimized to the ideal response from its corresponding *N*+2 coupling matrix individually with *EM* / numerical optimization methodologies [70]-[71]. The final *EM* responses are compared with the responses of coupling matrix as shown in Figure 6.2.4.2. The in-band performance matches well. The difference of transmission zero locations are due to the frequency dispersion of the *TE* and *TM* waveguide mode. The dispersion effect will get improved if using a higher order filter or decreasing the design bandwidth.
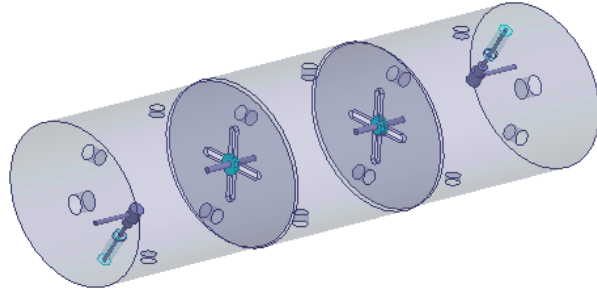
Figure 6.2.4.1. Layout of elliptical cavity triple-band filter.
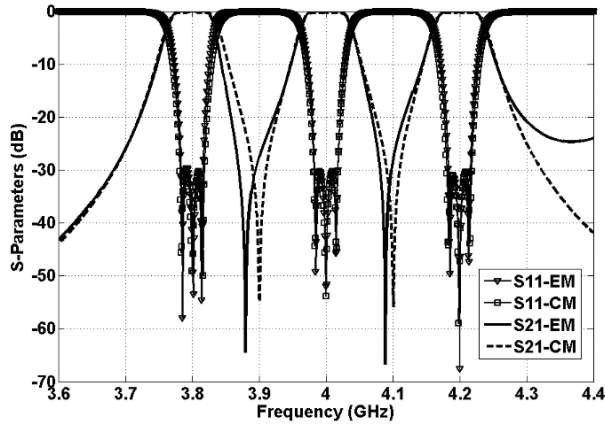
Figure 6.2.4.2. EM simulation response vs. coupling matrix response of the triple-band filter with elliptical cavities.

90

As mentioned earlier in chapter 3, the sign of particular coupling matrix parameters of the proposed triple-band filter affects positions of the transmission zeros between the passbands. In Figure 6.2.4.1 the two connectors are 180° apart in the first and last cavity, resulting 180° phase difference of the same mode in the first and the last cavity. This results in "out-of-phase" condition at the two frequencies between passbands leading to the generation of two transmission zeros as shown in Figure 6.2.4.3. The phase calculation along each path can follow the approach in Table 3.1. Figure 6.2.4.3 shows different distributions of transmission zeros with different locations of input and output probe.

(a)

(b)

(c)
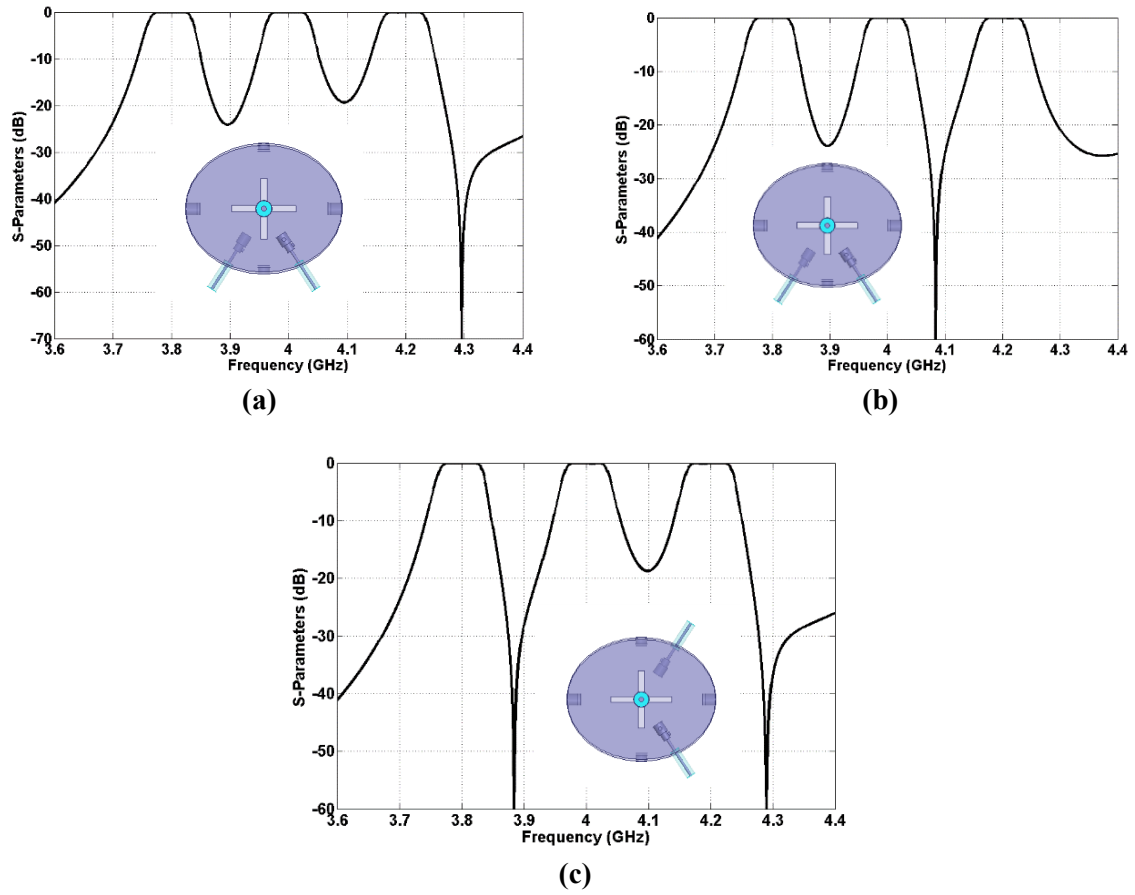
Figure 6.2.4.3. S_{21} **responses with two coaxial ports in parallel (*circle*), symmetric with short axis (*plus*), and symmetric with long axis (*triangle*)**

91

The designed triple-band filter was manufactured from copper as shown in Figure 6.2.4.4. Figure 6.2.4.5 shows the tuned near-band responses of the manufactured filter compared with the simulation responses. The measured *RL* is better than 20 dB and rejection between adjacent channels is more than 50 dB. The measured *IL* is 0.22 to 0.25 dB reflecting a loaded *Q* in the range of 6500 to 7000. The achieved loaded *Q* is lower than expected likely due to the imperfect surface finishing and parts contact. The tuned frequencies of the low-band and mid-band are lower compared to the simulation due to limited tunability of the TM_{010} mode.

Figure 6.2.4.4. Manufactured triple-band filter with elliptical cavity.
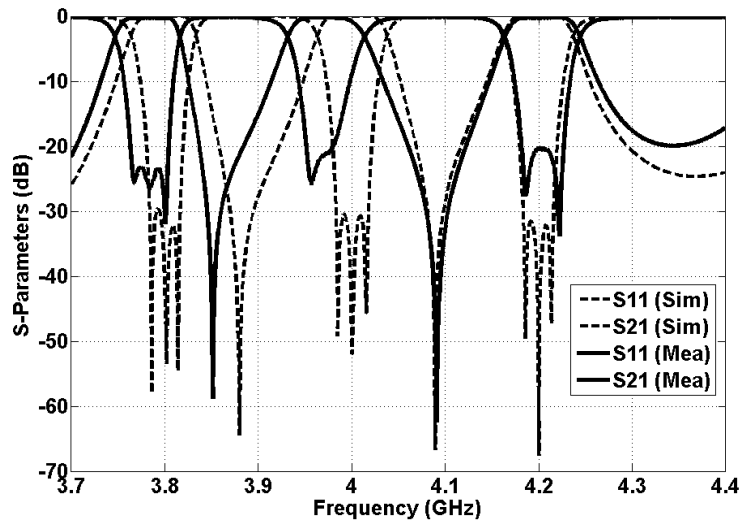
Figure 6.2.4.5. Measurement vs. simulation of the triple-band filter with elliptical cavities.

The triple-band filter with elliptical cavity provides very compact layout and high Q. However the following drawbacks have been noticed during the design, manufacturing and tuning:

1) Due to the in-line configuration, tuning screws for the TM_{010} mode can be added only to the first and last cavities. This reduces the overall tunability of the triple-band filter to overcome the unavoidable tolerances during manufacturing, especially at higher frequencies.

2) The stray coupling between three modes cannot be completely eliminated particularly when for the cases of narrow channel to channel separation.

3) The next spurious mode at the higher frequency is relatively close to the passband, especially with wider channel bandwidth or wider guard-band. This affects the upper-side rejection of the third channel. Unfortunately the spurious-free window is difficult to be expanded due to the intrinsic mode distribution of the elliptical cavity. A cover filter will have to be added along with the triple-band filter to suppress the close by spurious.

4) The inner-cavity probe is attached with the iris by a support made by dielectric material with low permittivity (*e.g.* Teflon). In each iteration of tuning, the filter has to be first disassembled then the probe can be replaced with different length. After the probe length is determined, the probe, the support, and the iris need to be re-bonded together with RTV silicone glue which complicates the tuning process.

5) High order filter functions lead to a rather long filter that might be restricted by certain layout requirement circumstances.

6.3　Triple-Band Filter with Rectangular Waveguide Resonators

6.3.1　Rectangular Triple-mode Resonator

For a rectangular waveguide structure, the resonant frequency of either the TE_{mnl} or TM_{mnl} modes is uniquely determined by their resonant wave number corresponding to the physical dimensions of the cavity "a", "b" and "d". For instance, the resonant frequency of the TE_{101} mode is determined by the cavity width a and length d; the resonant frequency of TE_{011} is determined by the cavity height b and length d; and the resonant frequency of TM_{110} is determined by the cavity width a and cavity height b, as stated in (6.6)-(6.8):

$$f_{TE_{101}} = \frac{c}{2\pi}\sqrt{(\frac{\pi}{a})^2 + (\frac{\pi}{d})^2} \ , \tag{6.6}$$

$$f_{TE_{011}} = \frac{c}{2\pi}\sqrt{(\frac{\pi}{b})^2 + (\frac{\pi}{d})^2} \ , \tag{6.7}$$

$$f_{TM_{110}} = \frac{c}{2\pi}\sqrt{(\frac{\pi}{a})^2 + (\frac{\pi}{b})^2} \ , \tag{6.8}$$

For a rectangular waveguide resonator with width "a", height "b" and length "d", it is well known that increasing the "b" dimension can effectively improve the quality factor of the TE_{10m} mode. However, the spurious-free window will decrease due to the cut-off frequency of the TE_{01} mode (*i.e.,* the first spurious mode after increasing "b") shifting closer to the pass band. In the proposed structure, the spurious modes TE_{011} and TM_{110} are employed together with the TE_{101} mode to associate with the three pass-band frequencies. Hence, the "b" dimensions are dramatically increased with respect to three polarizations in the triple-mode cavities, resulting in higher Q for all channels. The consequence is that the spurious performance is expected to be degraded as a result of the cut-off frequency of the next resonant mode (*e.g., TE_{111}*) drifting toward the passband.

An Eigen-mode analysis is performed to calculate the resonant frequencies and unloaded Q, as listed in Table 6.3. The first three modes (TE_{101}, TM_{110} and TE_{011}) are used to realize the three passbands respectively in the filter. The next mode (TE_{111}) is nearly 700 MHz higher leading to a significantly improved spurious-free window compared to the elliptical triple-mode resonator described in Section

6.2. The electrical field distribution of the three operating modes is shown in Figure 6.3.1. The intra-coupling only occurs between adjacent cavities by the modes with the same E-field orientation. The intrinsic isolation between the orthogonal modes provides a minimum interaction between the three single paths. Three tuning screws are located on the three adjacent planes of each triple-mode cavity resonator to provide independent control of the three resonant frequencies.

Table 6.3 Resonant modes in the Rectangular triple-mode Resonator

Dimensions (inch)	Mode	Frequency (GHz)	Unloaded Q (Copper)
$a = 2.2$ $b = 1.9$ $d = 2.4$	TE_{101}	3.62	16716
	TM_{110}	3.83	17104
	TE_{011}	4.04	17566
	TE_{111}	4.73	14690

(a)　　　　　　　　　　(b)　　　　　　　　　　(c)
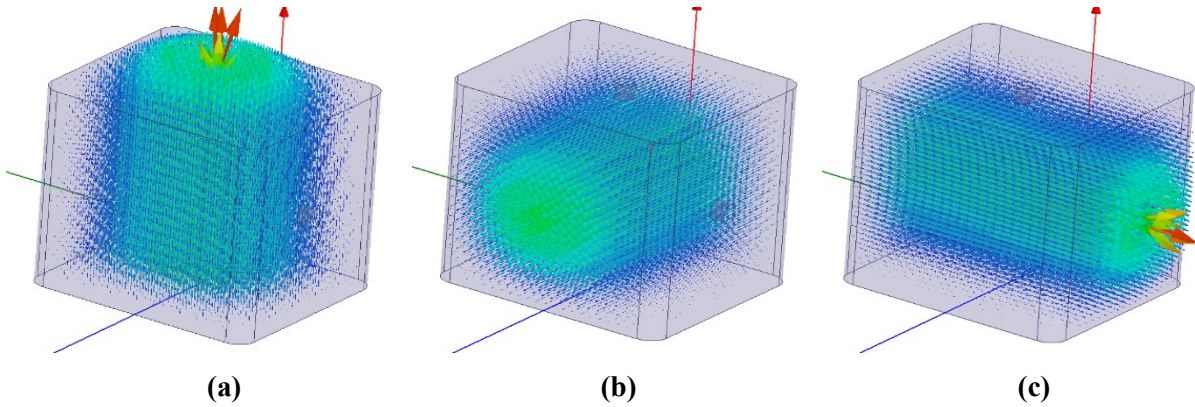
Figure 6.3.1. E-field vector of TE_{101}, TM_{110}, and TE_{011} modes in a rectangular triple-mode resonator.

6.3.2　Intra-Cavity Coupling

The inner coupling structure for the rectangular triple-mode resonator is a combination of a horizontal iris, a vertical iris and an electrical probe for coupling TE_{101}, TM_{110} and TE_{111} modes, respectively. The coupling structure is shown in Figure 6.3.2.1. Different from the inner-coupling structure of elliptical

resonator, the cross iris between the rectangular resonators is closer to the top surface. The electrical probe is crossing at the opening of the vertical iris and can be easily attached with the housing lid open. Such design is more flexible for the tuning adjustment. The dimensions of the irises and probes are determined by the coupling matrix parameters extracted from Eigen-mode simulation. The de-normalized coupling parameters can be calculated as per equations (6.4).
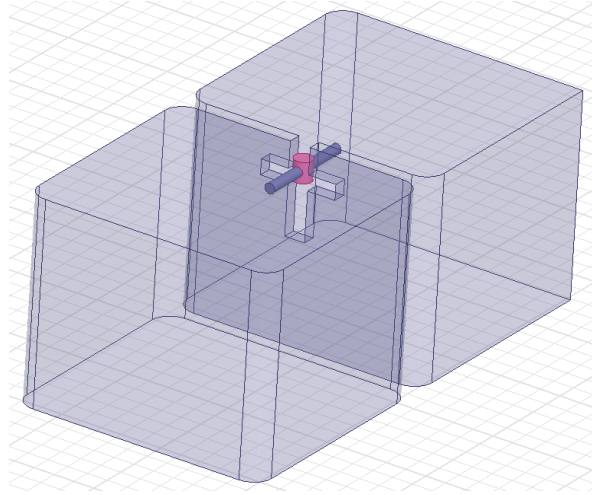
Figure 6.3.2.1. Inter-cavity coupling structure for rectangular triple-mode resonator.

Similar to the elliptical resonator, the inter-resonator coupling of each channel only occurs between adjacent cavities by the modes with the same *E*-field orientation. Therefore, the ideal coupling mechanism needs to include adjustable parameters sensitive to only one particular mode. Figure 6.3.2.2 (a) illustrates the relationship between the denormalized coupling coefficients of the three modes and the length of the probe. The TM_{110} mode can be controlled by the probe length, while the other two modes are not sensitive to the electrical probe coupling. The relationship between the coupling coefficient and the length of the vertical iris is shown in Figure 6.3.2.2 (b). A strong coupling to the TE_{011} mode can be achieved by the vertical iris. Figure 6.3.2.2 (c) illustrates the coupling distribution by the horizontal iris. The horizontal iris provides a strong coupling to the TE_{101} mode as well as a considerable coupling affect to the TM_{110} mode. This is because the horizontal iris is offset from the

cavity center thus parallel with the magnetic field of the TM_{110} mode. Such stray coupling effect can be easily compensated by the electrical probe coupling as shown in Figure 6.3.2.2 (a).

(a)

(b)

(c)
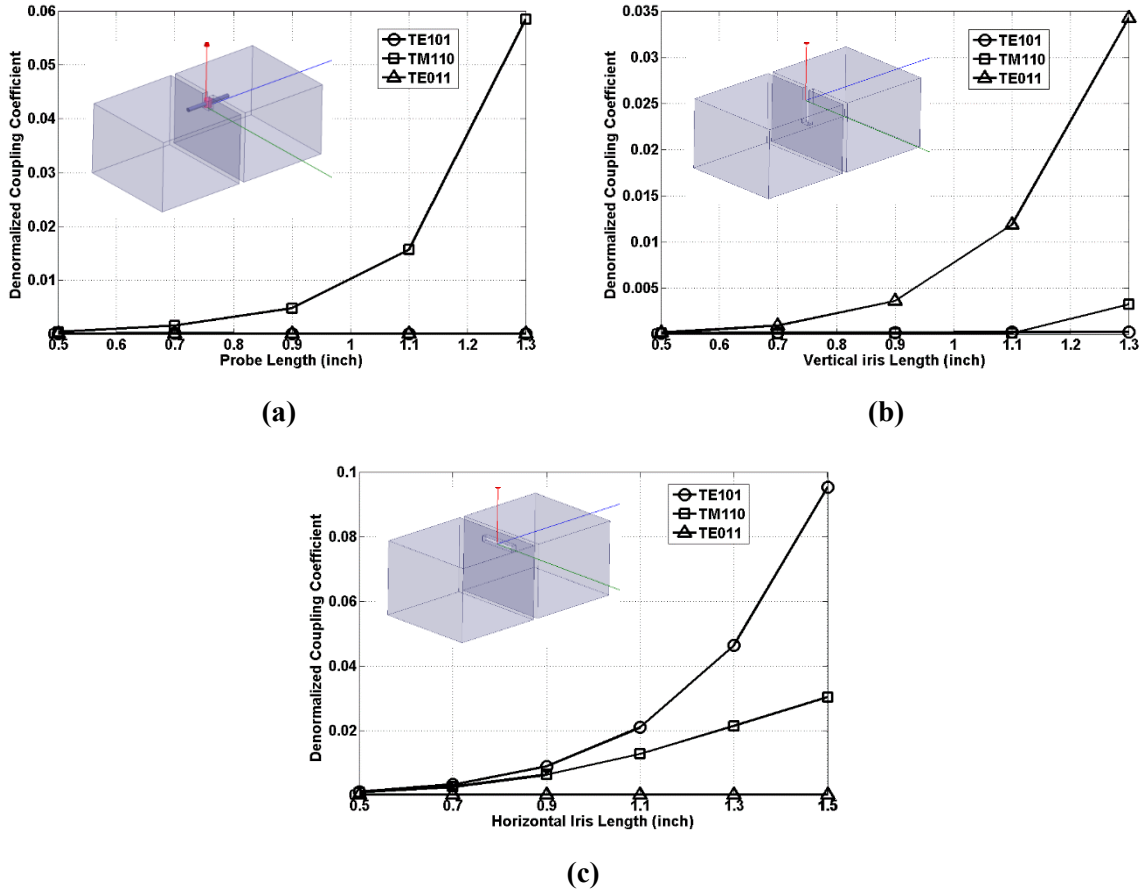
Figure 6.3.2.2. Relationship between inter-cavity coupling coefficients and (a) the probe length, (b) the vertical iris and (c) the horizontal iris.

6.3.3   Input / Output Coupling

The "L-shape" coaxial probe proposed in chapter 6.2.3 can also be used to excite the three orthogonal modes in rectangular triple-mode resonators. In Figure 6.3.3 (a) and (b), the parameters $L_1, L_2, \Delta L$ and θ can be tuned to determine the input coupling strength and distribution to the TM_{110}, TE_{101} and TE_{011} modes. The influence of the four above parameters on the input coupling coefficients is studied and summarized in Table 6.4. In general, L_2 determines the coupling to TM_{110}, ΔL determine the overall

coupling to the TE_{101} and TE_{011} modes, while L_1 and θ controls the distribution of overall coupling to the two modes. It is worth to note that the external couplings achieved in the rectangular resonator is relatively smaller than those achieved in the elliptical resonator case because the coaxial connector is located physically further from the center of the cavity where the maximum E-fields of all the three modes locate. However the coupling strength can be increased by increasing the diameter of the probe L_1 and L_2.

(a)   (b)
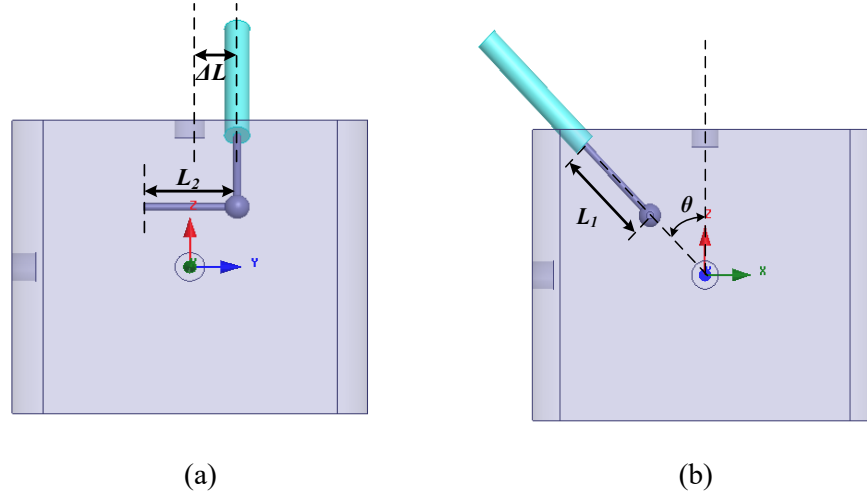
Figure 6.3.3. (a) Right view, and (b) front view of the input/output coupling structure for the rectangular triple-mode resonator.

Table 6.4 Parametric Study of Physical Parameters Relating to the Input /Output Couplings

of the Three Rectangular Waveguide Modes

	TE_{101}	TM_{110}	TE_{011}
L_1 (+)	(+)	(-)	(-)
L_1 (-)	(-)	(+)	(+)
θ (+)	(-)	(-)	(+)
θ (-)	(+)	(+)	(-)
L_2 (+)	(-)	(+)	-
L_2 (-)	(+)	(-)	-
ΔL (+)	(-)	-	(-)
ΔL (-)	(+)	-	(+)

(+): increase; (-) decrease

6.3.4 Folded Triple-band Filter Design with Rectangular Cavities

The proposed structure is illustrated by a 12-pole triple-band filter as shown in Figure 6.3.4.1. Four triple-mode resonators operating in TE_{101}, TE_{011} and TM_{110} modes are connected to form a folded configuration. Compared to the in-line configuration, the folded configuration provides convenience to add tuning screws on all three polarlizations thus improving the tunnablity of the three passbands.
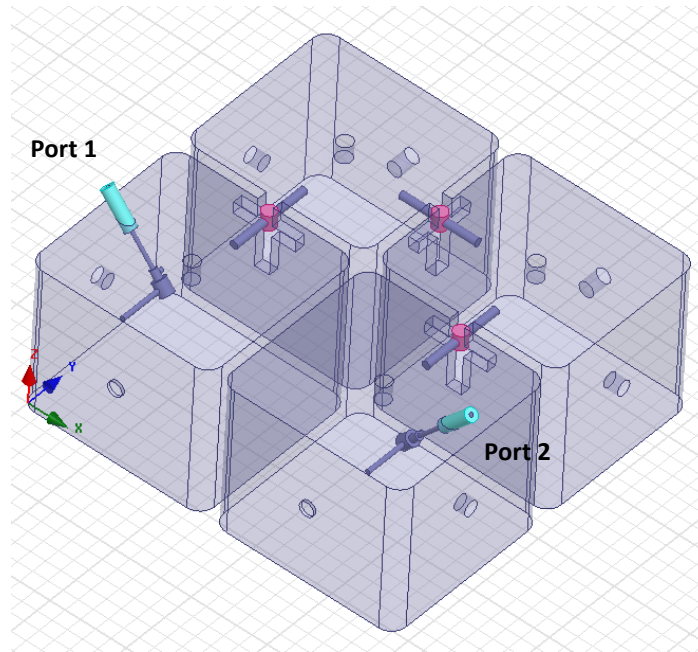
Figure 6.3.4.1. Internal structure of a 4th-order proposed triple-band filter.

The design is based on the coupling matrix in (6.9) with a $CF = 4.0$ GHz and $BW = 20$ MHz, giving the center frequencies of the three pass-bands are at 3.6, 3.8 and 4.0 GHz, respectively. The designed triple-band filter was manufactured with two parts (a housing and a lid), both from copper, as shown in Figure 6.3.4.2. The filter showed an improved tunablity and ease-of-assembly compard with the ellilptical cavity design. Figure 6.3.4.3 shows the measurement near-band response of the proposed filter. The measured RL is better than 23 dB and rejection between adjacent channels is more than 55 dB. The insertion loss is 0.38 to 0.46 dB, reflecting a loaded Q in the range of 7800 to 8500. The tuned frequency of the mid-band is slightly lower compared to the simulation due to the high sensitivity of

electrical probes affecting frequency and coupling of the TM_{110} mode. A transmission zero is observed between the middle and high passbands because of an "out of phase" condition at the frequency between the TE_{011} and TM_{110} paths. In Figure 6.3.4.4, the out-of-band spurious rise at about 4.5 GHz, indicating a wider spurious-free window compard to the design with elliptical cavties.

$$
M = \begin{bmatrix}
0 & 1.317 & 0 & 0 & 0 & 1.266 & 0 & 0 & 0 & 1.250 & 0 & 0 & 0 & 0 \\
1.317 & 20.753 & 1.273 & 0 & 0 & 0 & 0 & 0 & 0 & 0 & 0 & 0 & 0 & 0 \\
0 & 1.273 & 20.552 & 0.9177 & 0 & 0 & 0 & 0 & 0 & 0 & 0 & 0 & 0 & 0 \\
0 & 0 & 0.9177 & 20.552 & 1.273 & 0 & 0 & 0 & 0 & 0 & 0 & 0 & 0 & 0 \\
0 & 0 & 0 & 1.273 & 20.753 & 0 & 0 & 0 & 0 & 0 & 0 & 0 & 0 & 1.317 \\
1.266 & 0 & 0 & 0 & 0 & -0.007 & 1.195 & 0 & 0 & 0 & 0 & 0 & 0 & 0 \\
0 & 0 & 0 & 0 & 0 & 1.195 & 0 & 0.864 & 0 & 0 & 0 & 0 & 0 & 0 \\
0 & 0 & 0 & 0 & 0 & 0 & 0.864 & 0 & 1.195 & 0 & 0 & 0 & 0 & 0 \\
0 & 0 & 0 & 0 & 0 & 0 & 0 & 1.195 & -0.007 & 0 & 0 & 0 & 0 & 1.266 \\
1.250 & 0 & 0 & 0 & 0 & 0 & 0 & 0 & 0 & -19.699 & 1.145 & 0 & 0 & 0 \\
0 & 0 & 0 & 0 & 0 & 0 & 0 & 0 & 0 & 1.145 & -19.505 & 0.825 & 0 & 0 \\
0 & 0 & 0 & 0 & 0 & 0 & 0 & 0 & 0 & 0 & 0.825 & -19.505 & 1.145 & 0 \\
0 & 0 & 0 & 0 & 0 & 0 & 0 & 0 & 0 & 0 & 0 & 1.145 & -19.699 & 1.250 \\
0 & 0 & 0 & 0 & 1.317 & 0 & 0 & 0 & 1.266 & 0 & 0 & 0 & 1.250 & 0
\end{bmatrix}
$$

$$(6.9)$$
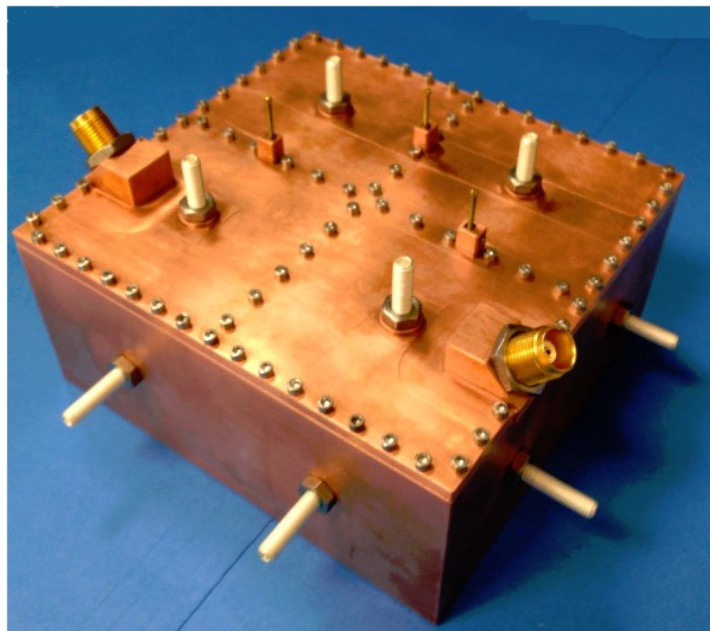
Figure 6.3.4.2. Manufactured triple-band filter with rectangular cavity.
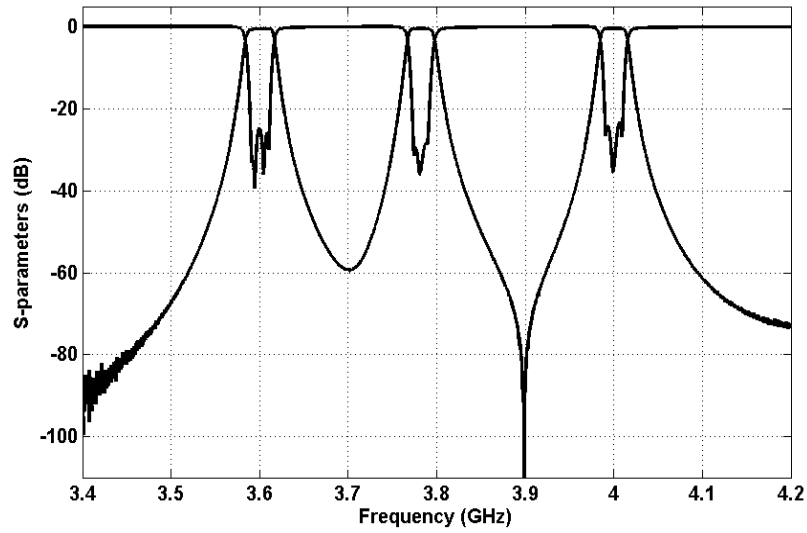
Figure 6.3.4.3. Measurement near-band responses of the 12-pole triple-band filter.
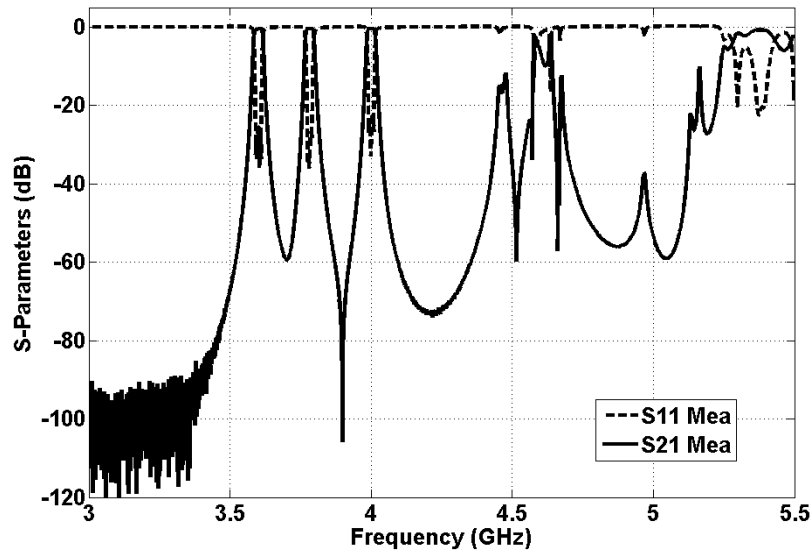
Figure 6.3.4.4. Measurement out-of-band responses of the 12-pole triple-band filter.

The rectangular waveguide design is another triple-band filter solution having a number of advantages and disadvantages compared to elliptical designs.

Advantages:

- The three operation modes TE_{101}, TE_{011} and TM_{110} in the rectangular waveguide have higher degrees of orthogonality than the modes in the elliptical waveguide, generating less stray coupling between either modes. Therefore the rectangular waveguide design are more suitable for the applications with relatively smaller passband separations.

- The rectangular cavity design has a wider spurious free window compared to that of the elliptical cavity. Figure 6.3.4.4 shows the measured out-of-band rejection measurement. The spurious rises at about 4.45 GHz.

- The triple-band filter based on rectangular waveguide is easier to form a folded configuration. This provide accessibility of adding more tuning elements to control the self-coupling and sequential coupling on each channel path.

Disadvantages:

- The external couplings achieved in the rectangular resonator is relatively smaller than those achieved in the elliptical resonator case because the coaxial connector is located physically further from the center of the cavity where the maximum E-fields of all the three modes locate. The bandwidth of each channel could be limited as a consequence.

- The IL will be slightly higher for the rectangular waveguide design due to a lower Q of the operating modes in rectangular waveguide compared to those in elliptical waveguide.

6.4   Conclusion

The triple-band filters have been realized by two different high-Q waveguide resonator structures. Each cavity resonator employs triple-modes with resonant frequencies associated with the three passbands. Such approach provides the most significant size and mass saving while maintaining a high Q. The first design was an elliptical-cavity triple-band filter with an in-line configuration. Each passband

of the filter was controlled by a dedicated polarization and represented by an inline direct-coupled set of resonators. The second design was a rectangular-cavity triple-band filter with a folded configuration. Compared to elliptical cavity design, the three modes in the rectangular resonator have higher degree of orthogonality making it easily to independently control the inter-resonator couplings of three modes. The folded configuration overcomes a number of drawbacks from the elliptical in-line design including an improved tunability and ease of assembly, while has a relatively lower Q and narrower realizable BW.

Chapter 7

Dielectric Triple-Band Bandpass Filters

7.1   Introduction

The waveguide triple-band filters feature high Q however presents a major size constrain particularly when operating at low frequencies. The high permittivity dielectric filters [60] feature high Q and reduced volume, offering a popular solution in narrow-band satellite and wireless commutation systems. In [4], the high permittivity dielectric resonator is modified by cutting a number of slots to improve the spurious-free window. The modified resonator is used to implement a dual-band filter. In this section, a triple-band filter is proposed based on triple-mode dielectric resonators, providing a compact size with enhanced quality factor. The triple-mode resonator is implemented by a high permittivity dielectric of a cuboid shape enclosed by a metallic housing. Such resonator structure supports *TEH*, ½ *HEE* and ½ *HEH* modes, producing three parallel and nearly non-interacting paths. The unique dielectric resonator structure still allows independent control of the center frequencies of three passbands by shaping the dielectric resonator through the introduction of specific slots.

7.2   Triple-mode Dielectric Resonator

The proposed triple-mode dielectric resonator is machined from a single piece of *Trans-Tech* 3500-series ceramic dielectric material with a dielectric constant of 35. The dielectric material is cut to a cuboid shape and machined with four slots (S_1, $2 \times S_2$, and S_3) as illustrated in Figure 7.2.1. Slots S_1 and S_2 are in parallel and are located at center and quarter positions of the top surface. Slot S_3 is located at center of the side surface and perpendicular to S_1 and S_2. This structure supports *TEH*, ½ *HEE* and ½

HEH [60] as operating modes for three designated passbands. Their electric-field distributions are shown in Figure 7.2.2. Such resonator configuration demonstrates a number of characteristics,

1) The use of slots eliminates the degenerated counterparts of the operating ½ *HEE* and ½ *HEH* modes.

2) The slots provide extra degrees to fine-tune resonant frequencies of each mode, *i.e.* S_1 to control *TEH* mode, S_2 to control ½ *HEH* mode and S_3 to control ½ *HEE* mode.

3) The slots help to shift the *TME* mode of original rectangular dielectric resonator to achieve a considerable spurious-free window.

4) They have minimal impact on unloaded Q of each mode.
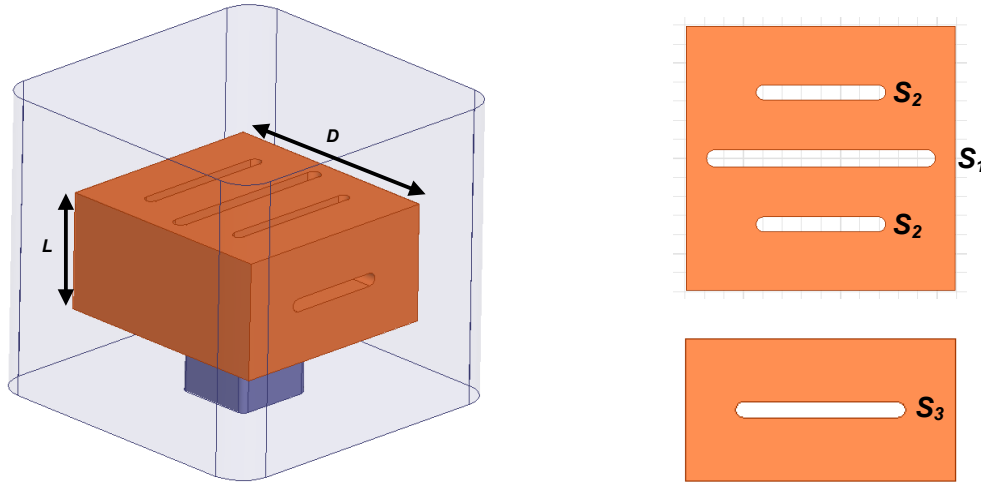
Figure 7.2.1. Triple-mode dielectric resonator.

The unique configuration of the dielectric resonator provides a two-level frequency control for each mode, i.e. a rough control by choosing the *D/L* ratio and a fine control by adjusting the length of the slots S_1, S_2 and S_3 in the dielectric resonator. A mode chart of the proposed dielectric resonator is shown in Figure 7.2.3. The chart demonstrates frequency distributions of the first four resonant modes of the dielectric resonator with different *D/L* ratios. The three modes with lower frequencies (*TEH*, ½ *HEH* and ½ *HEE* modes) are employed to carry the passband signals while the one with the highest resonant

mode is considered as spurious. It might be noticed the *HEH* and *HEE* mode have almost identical frequency spacing over the whole *D/L* range, thus a further degree of frequency controlling of the modes
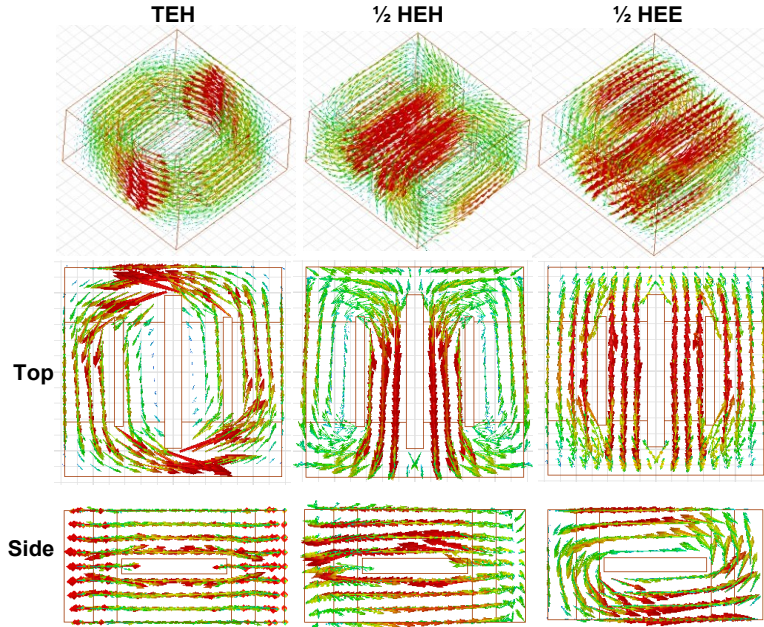
Figure 7.2.2. Views of electrical field distribution of the *TEH*$_{01}$, ½ *HEH*$_{11}$ and ½ *HEE*$_{11}$ modes.
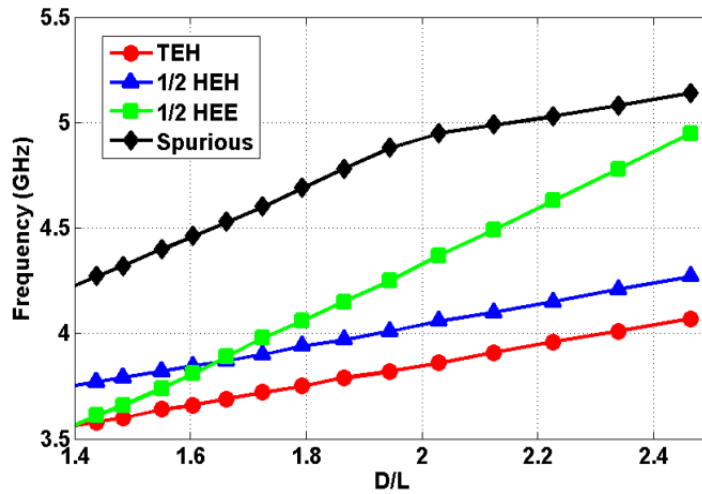
Figure 7.2.3. Mode chart of a triple-mode dielectric resonator with *D* = 0.69 in, *Ɛr* = 35, and 1×1×0.9 in³ cavity.

is required. Figs. 7.2.4 (a)-(c) demonstrate the relationship between the mode frequencies and the slot lengths S_1, S_2 and S_3. The TEH and *HEE* modes can be independently controlled by S_1 and S_3 respectively, while S_2 affects both *TEH* and *HEH* mode.

With a proper selection of *D/L* and the slot lengths S_1, S_2 and S_3, specific combinations of passband frequencies as well as spurious-free window can be achieved. In this case *D/L* is chosen to be 1.9, resulting three passbands at around 3.8, 4.0 and 4.2 GHz with the next spurious mode at around 4.84 GHz as summarized in Table 7.1. The unloaded *Q* of the three dielectric modes is relatively lower than the waveguide modes however consuming a much smaller size. It is worth noting the three operating modes are not fully orthogonal-polarized, resulting in small parasitic coupling between any two modes. Therefore, the proposed resonator is not recommended to applications with small guard-band.
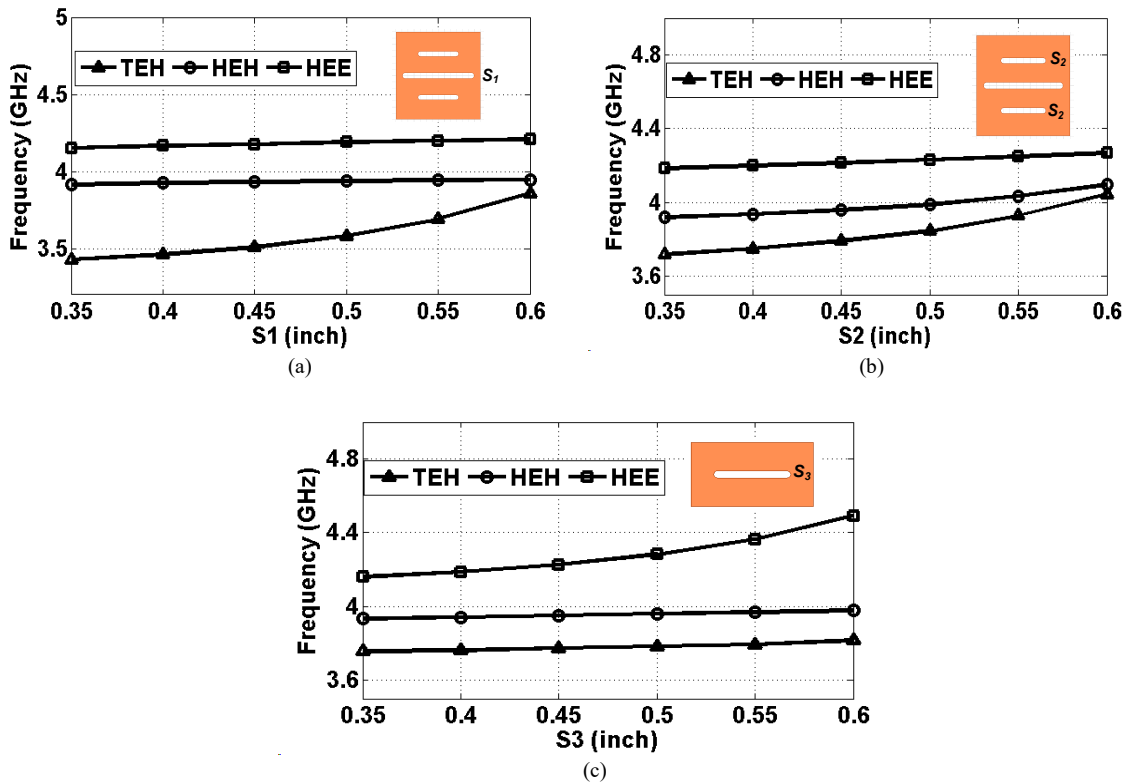
Figure 7.2.4. **Relationship between mode frequencies and slot lengths (a)** S_1 **(top view), (b)** S_2 **(top view), and (c)** S_3 **(side view).**

Table 7.1 Resonant modes in the Dielectric Triple-mode Resonator

Dimensions (inch)	Mode	Frequency (GHz)	Unloaded Q (with copper cavity)
D = 0.69 *L = 0.35* *ε_r = 35*	TEH	3.82	13637
	½ HEH	4.04	15404
	½ HEE	4.24	13566
	Spurious	4.84	15290

7.3   Intra-Resonator Coupling

The inter-resonator coupling is realized by a horizontal iris, a vertical iris and an electrical probe as shown in Figure 7.3.1, coupling *TEH*, *½ HEE* and *½ HEH* modes respectively. The two inner iris branches are designed in a long rectangular shape and the electrical probe can be adjusted vertically crossing the inter-cavity wall. The relationship between each sub-section and the couplings to the three modes are demonstrated in Figure 7.3.2 (a)-(c), proving the configuration is effective to couple the three dielectric modes independently with minimum interactions. Using Eigen-mode simulation by placing electric and magnetic walls along the symmetry plane [12], the sequential coupling coefficients of the three paths can be calculated as per equations (9). The corresponding dimensions of the irises and probes are then determined accordingly.
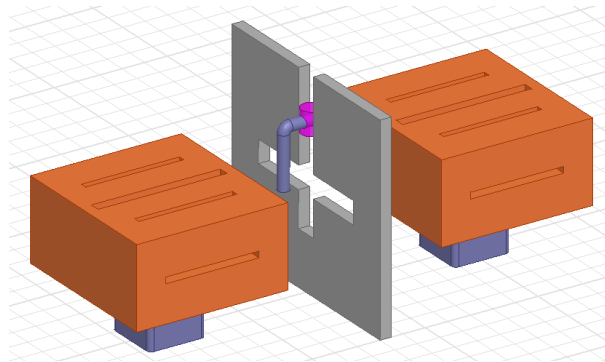
Figure 7.3.1. Intra-cavity coupling configuration of the dielectric triple-band filter.

(a)   (b)

(c)
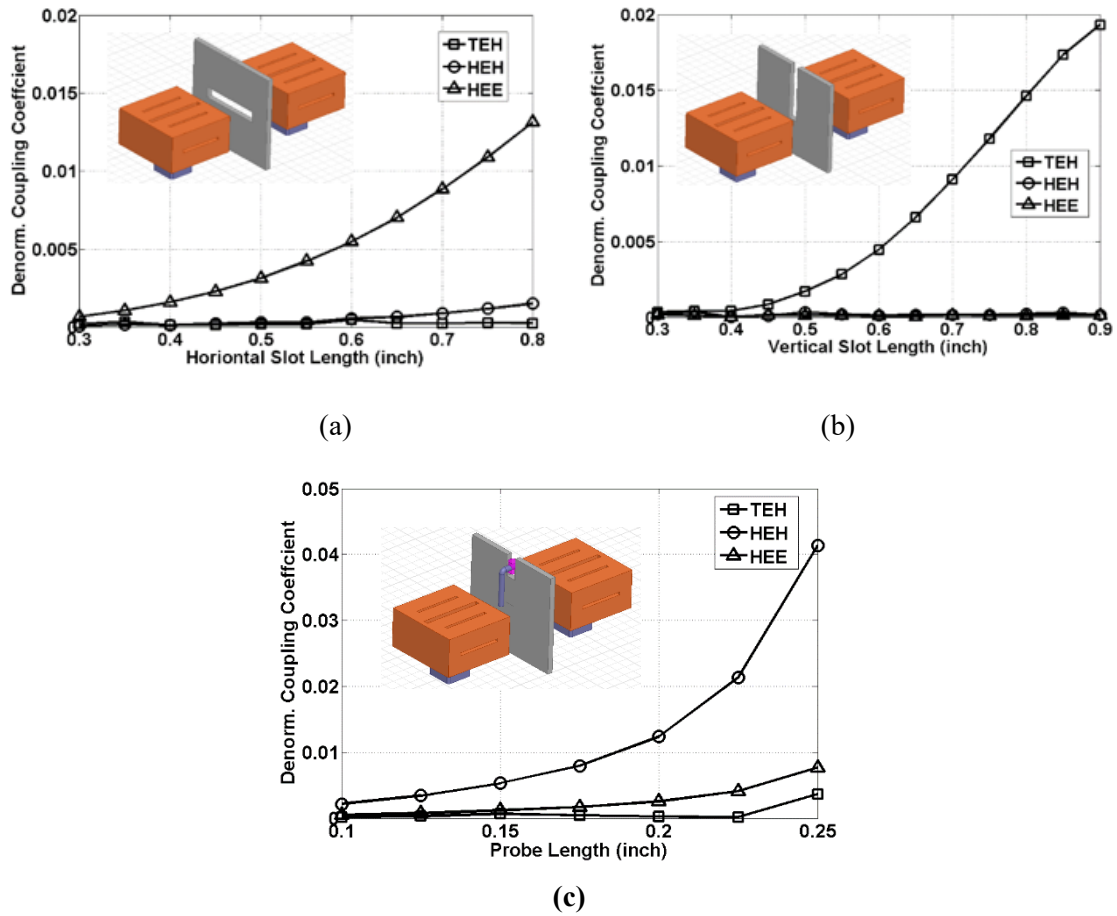
Figure 7.3.2. Relationship between inter-cavity coupling coefficients and (a) the horizontal iris, (b) the vertical iris and (c) the probe length.

7.4   Input/output Coupling

For the dielectric triple-band filter, the input/output coupling can be realized by a probe located parallel to one edge of the dielectric resonator as shown in Figure 7.4.1. The field distribution of the dielectric loaded resonator is more complicated than waveguide resonator and large percentage of electric field is stored inside the high permittivity dielectric puck. A change of the relative location (X_1, L_1 and D_1) of the probe would affect all three operating modes simultaneously but with different degrees. In Table 7.2, the distance X_1 has a major impact on the coupling to the ½ *HEE* and ½ *HEH* mode but less sensitive to *TEH* mode. Probe length L_1 has a major impact on the coupling to the *TEH* and ½ *HEH*

mode, with a minor effect on ½ *HEE*. Moving the probe further/closer (increasing or decreasing D_1) from the resonator decreases/increases the coupling to *TEH* and ½ *HEE* mode. An interactive process might be required to design the specified input couplings for each mode. Examples of reflected group delay distributions to the three modes at around 3.8, 4.0 and 4.2 GHz are shown in Figure 7.4.2. Such configuration is capable to fully control the input/output coupling for the three dielectric modes while maintaining a simple structure.

(a)   (b)
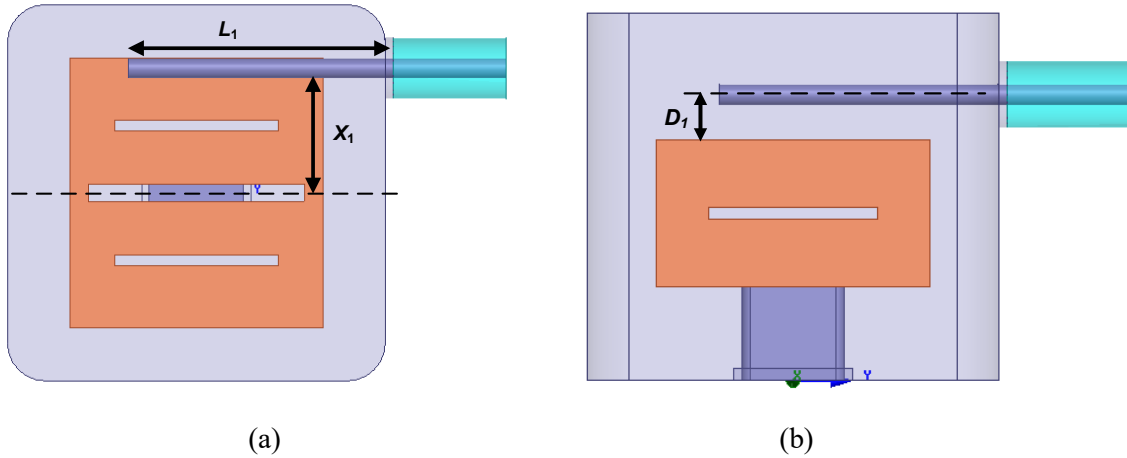
Figure 7.4.1. (a) Top view, and (b) front view of the input/output coupling structure for the dielectric triple-mode resonator.

Table 7.2 Parametric Study of Physical Parameters relating to the Input /Output Couplings of the Three Dielectric Modes

	TEH	*½ HEH*	*½ HEE*
X_1 (+)	Minor (+)	(-)	(-)
X_1 (-)	Minor (-)	(+)	(+)
L_1 (+)	(-)	(-)	Minor (-)
L_1 (-)	(+)	(+)	Minor (+)
D_1 (+)	(-)	Minor (+)	(-)
D_1 (-)	(+)	Minor (-)	(+)

(+): increase; (-) decrease
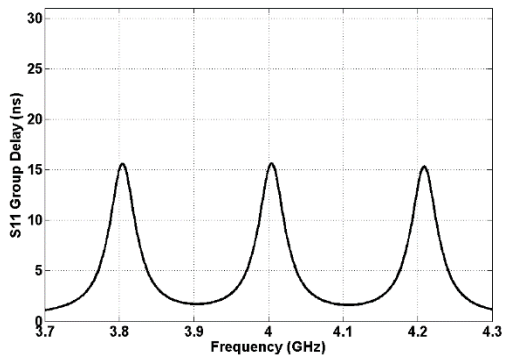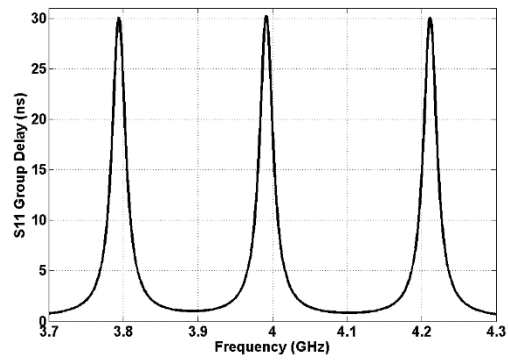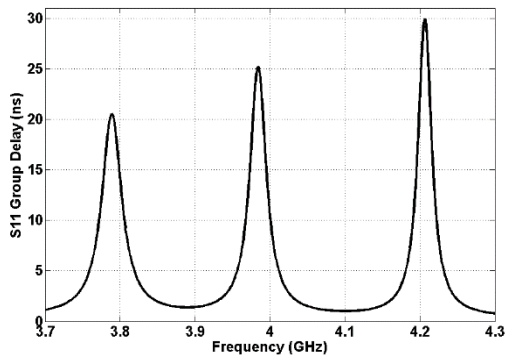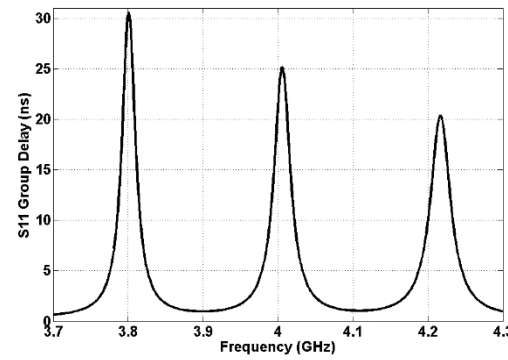
Figure 7.4.2. Input reflected group delay of (a) balanced 15 ns, (b) balanced 30 ns, (c) 20-25-30 ns, and (d) 30-25-20 ns for the dielectric triple-band filter.

111

7.5   Dielectric Triple-band Filter Design

A 9-pole C-band triple-band filter is demonstrated to prove the feasibility of the proposed approach. The design layout is shown in Figure 7.5.1. The coupling matrix is in (7.1), with $CF = 4.0$ GHz and BWs are all 20 MHz.

$$
M = \begin{bmatrix}
0 & 1.426 & 0 & 0 & 1.351 & 0 & 0 & 1.353 & 0 & 0 & 0 \\
1.426 & 20.77 & 1.568 & 0 & 0 & 0 & 0 & 0 & 0 & 0 & 0 \\
0 & 1.568 & 20.50 & 1.568 & 0 & 0 & 0 & 0 & 0 & 0 & 0 \\
0 & 0 & 1.568 & 20.77 & 0 & 0 & 0 & 0 & 0 & 0 & 1.426 \\
1.351 & 0 & 0 & 0 & -0.01 & 1.438 & 0 & 0 & 0 & 0 & 0 \\
0 & 0 & 0 & 0 & 1.438 & 0.00 & 1.438 & 0 & 0 & 0 & 0 \\
0 & 0 & 0 & 0 & 0 & 1.438 & -0.01 & 0 & 0 & 0 & 1.351 \\
1.353 & 0 & 0 & 0 & 0 & 0 & 0 & -19.77 & 1.409 & 0 & 0 \\
0 & 0 & 0 & 0 & 0 & 0 & 0 & 1.409 & -19.51 & 1.409 & 0 \\
0 & 0 & 0 & 0 & 0 & 0 & 0 & 0 & 1.409 & -19.77 & 1.353 \\
0 & 0 & 0 & 1.426 & 0 & 0 & 1.351 & 0 & 0 & 1.353 & 0
\end{bmatrix} \tag{7.1}
$$

The filter is manufactured with a copper housing as shown in Figure 7.5.2. The resonators are supported in the cavities using Ultem material with a dielectric constant of 3.5. The measurement near-band and out-of-band response of the proposed filter is shown in Figure 7.5.3 and Figure 7.5.4. The measured return loss is better than 17 dB and good rejection is achieved between adjacent channels, reaching 60 dB. The in-band insertion loss for the three channels is between 0.36 to 0.41 dB, reflecting a loaded Q in the range of 7500 to 8000 at ambient temperature. The tuned frequencies of the passbands are slightly shifted from the simulation due to the machining tolerances and the variation of dielectric permittivity. Phase reversal between two adjacent paths results in two transmission zeros, located between adjacent channels. A thermal test with the operating temperature from -20°C to 60°C was performed to show the stability of the dielectric filter. As can be seen in Figure 7.5.5 the low and high channel are very stable while a very minor deviation in return loss is observed in the middle channel. The extracted coefficient of thermal expansion is 2.1 ppm/°C, comparable to that from conventional dielectric filters.
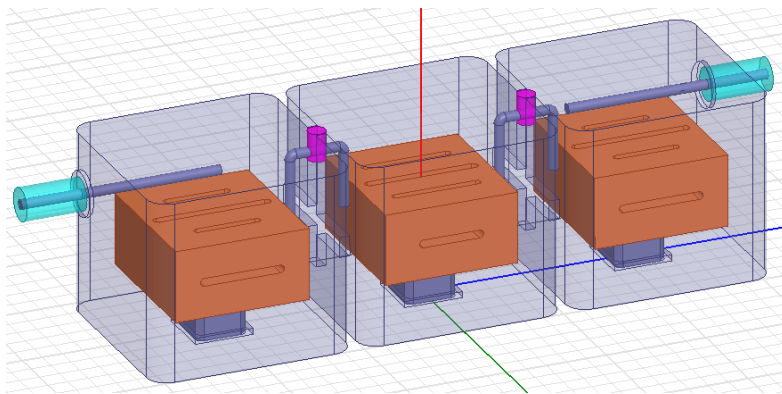
Figure 7.5.1. Structure of a 3rd order dielectric triple-band filter.
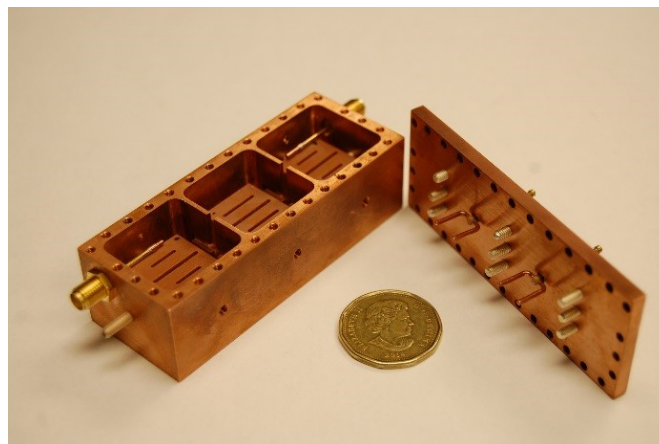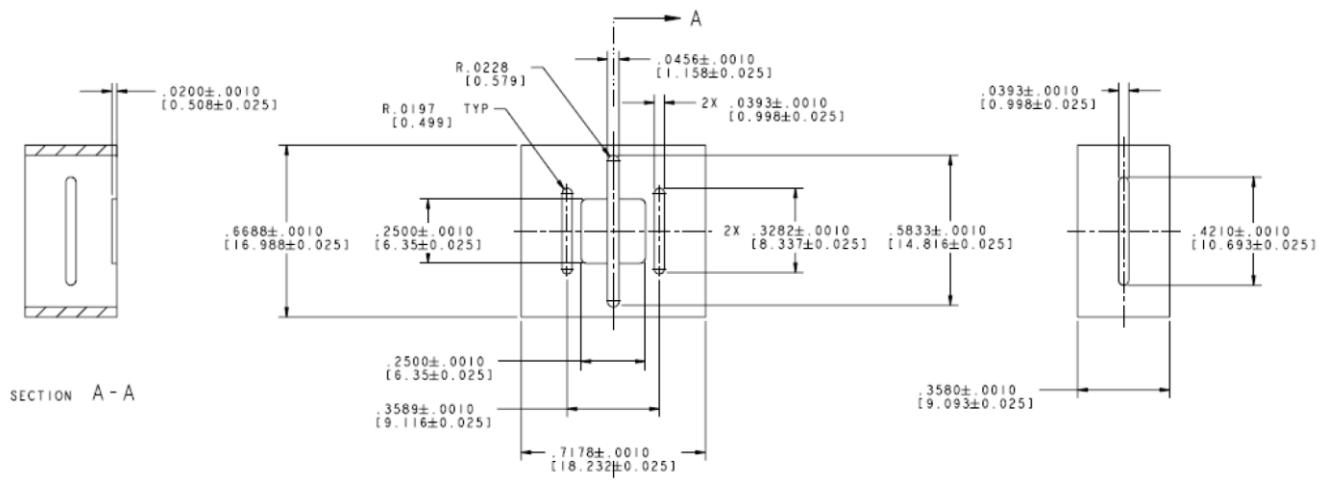
Figure 7.5.2. Layout of the proposed dielectric triple-band filter.
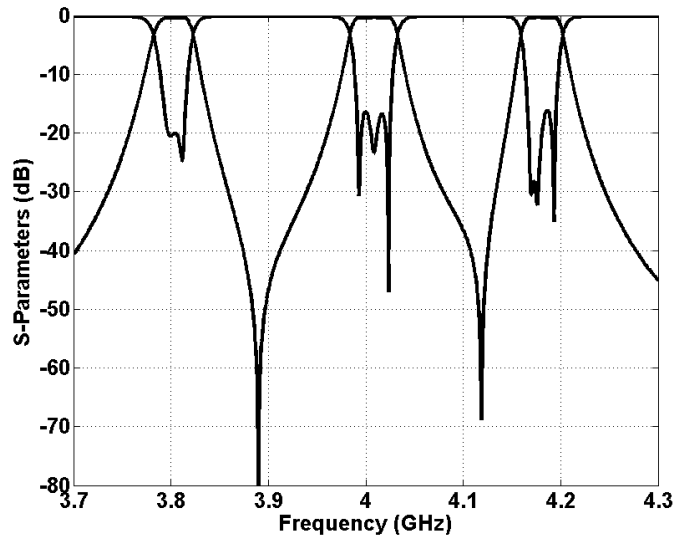
Figure 7.5.3. Measured Near-band *S*-parameter of the dielectric triple-band filter.
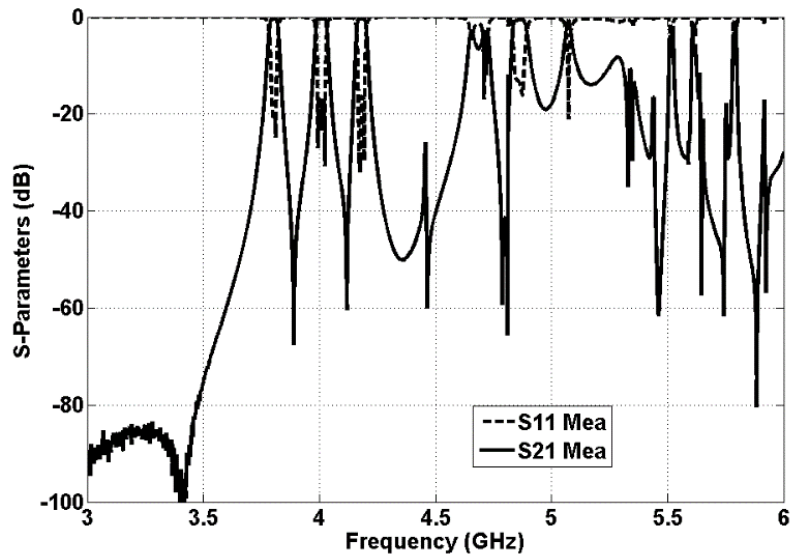
Figure 7.5.4. Measured out-of-band *S*-parameter of the dielectric triple-band filter.
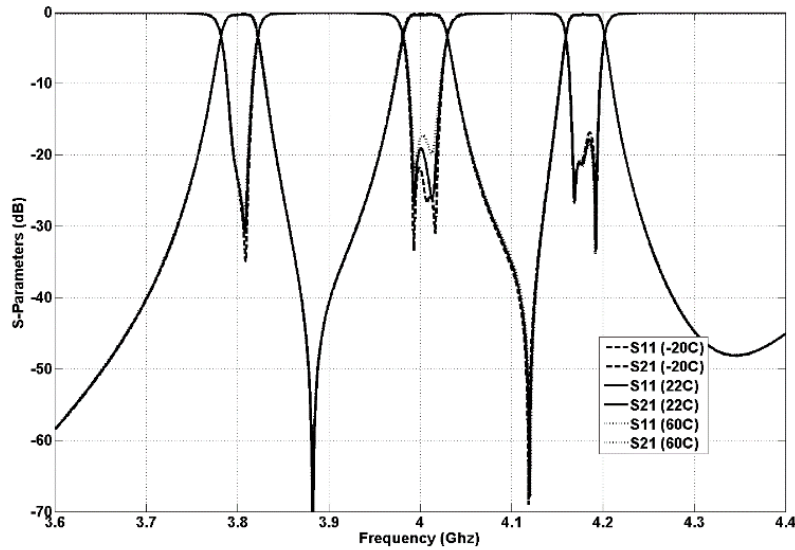
Figure 7.5.5. Measured thermal performances of the dielectric triple-band filter.

7.6 Comparison between the Three Realizations of Triple-Band Filters and Design Procedure

In Table 7.3, the three realizations of the triple-band filtering configuration are compared in terms of RF parameters, volume, design/manufacturing complexity and tunability. The design with dielectric resonators offers the most efficient Q over size, but require more sophisticated design and tuning iterations.

Table 7.3 Comparison of the Realizations of Triple-band Filter at 4 GHz

	Q_u	Vol. per Res.	Q_u/V	Design Challenge	Tunability
Ellip. WG	~19000	~320 cm^3	59.3	Medium	Medium (+)
Rect. WG	~17000	~300 cm^3	56.6	Medium	High
Dielectric	~14500	~50 cm^3	290	High	Medium (-)

115

The design procedure of the proposed class of the triple-band filters can be summarized according to the flow chart in Figure 7.6 with the major steps outlined below:

Step 1: Synthesis of coupling matrix of each channel filter. These matrices need then to be normalized to the *CF* and *BW* of the center channel.

Step 2: Combine the three sub-coupling matrices and perform a simple optimization of the coupling matrix to achieve the desired rejection and return loss of each channel. .

Step 3: Define the triple-mode resonator with desired realization (waveguide or dielectric) having three operating resonant modes at the designated frequencies. Make sure sufficient spurious-free window is obtained.

Step 4: Identify the inter–resonator coupling structure that independently yields the coupling coefficients associated with the three resonant nodes. .

Step 5: Identify the input/output coupling configuration to achieve the required reflected group delay peak values of the three passbands.

Step 6: Use EM simulation to realize the physical dimensions of the all inter-resonator and input/output coupling and simulate the overall filter to get the initial response.

Step 7: In the optimization process, treat the triple-band filter as three single-band filters and perform the EM / numerical optimization to each channel filter individually.

Step 8: Fine optimization of filter performance can be done experimentally through the use of tuning screws.

7.7   Conclusion

A triple-band bandpass filter realized using dielectric resonators has been presented in this chapter. The unique dielectric triple-band filter design harness the advantages of very compact size with high *Q*, and allows independent control of each coupling matrix parameters. The concept has been demonstrated and experimentally validated by a 3rd order C-band design.
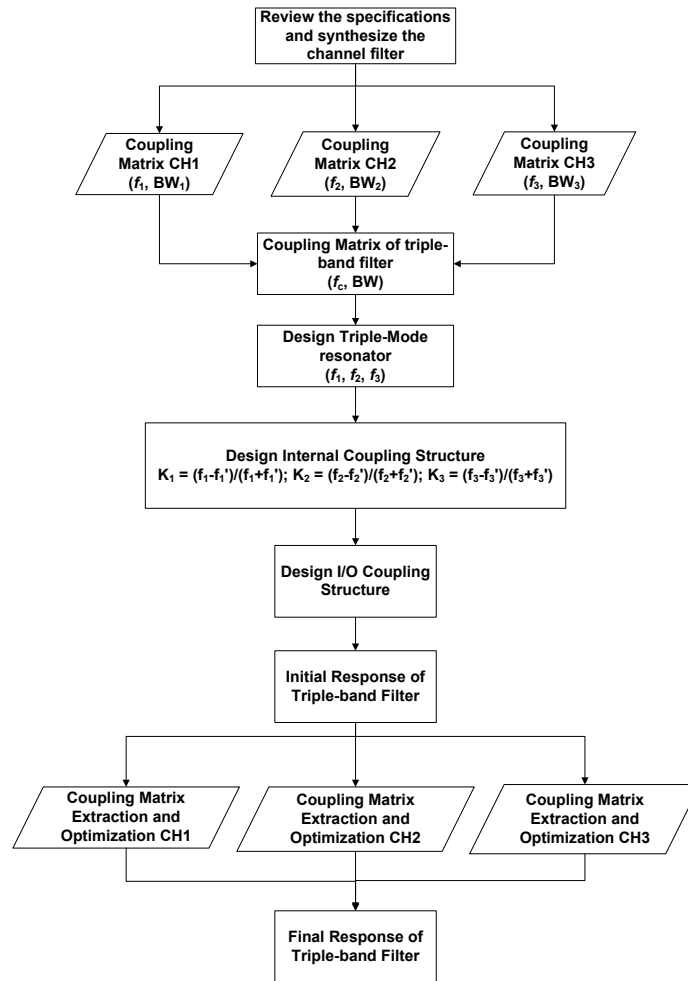
Figure 7.6. A general design procedure of the triple-band filter.

Chapter 8

Tunable Multi-band Filter

8.1   Introduction

As a key building block for any flexible transceiver, tunable filters have been in great demand in a wide range of applications from software defined radios to reconfigurable satellite payloads. The two critical parameters for tunable filters that operate wireless base station and satellite applications are high Q, and consistent selectivity over the entire tuning range. Consistent selectivity is important due to the expensive frequency spectrum of any communication system and high Q is always desired to minimize the system noise figure as well as maximize the output power. For tunable filters, to be used in such applications, they have to exhibit Q values and selectivity comparable to that achieved by the existing fixed filter technologies.

Over the past years, several papers have been reported in literatures employing tuning elements such as semiconductor, MEMS, piezoelectric actuators and motors [26]-[59]. Mechanically tunable cavity filters offer higher unloaded Q compared to the filters with other tuning mechanism. The simplicity and low cost of the mechanically tuned implementation further makes them a strong candidate for the new generations of communication systems. In this chapter, an approach to realize a tunable constant bandwidth with single tuning element is first introduced for a single band filter. The approach is then extended to a multi-band filter. Adding tunability to the multi-band filter will further increase the flexibility of the communication payload system.

8.2 Tunable Filter with Constant Bandwidth

Tunable filters employing tuning elements for the *CF* control have been reported in many literatures [18][72]. A common drawback of those tunable filters is the change in bandwidth and the degrading *RL* and *IL* over the tuning range. This issue is attributed to the changes of the coupling parameters as a function of *CF*s when the filter is driven over the tuning range. The relationship between the coupling parameters and *CF* is shown in (8.1).

$$M_{ij} = K_{ij} \times \frac{f_0}{BW},$$

$$(8.1)$$

where M_{ij} and K_{ij} are the normalized and denormalized coupling coefficients between two resonators respectively. To maintain a constant bandwidth across the tuning range, M_{ij} and *BW* remains constant provided that $f_0 \times K_{ij}$ remains constant as the f_0 changes. Therefore the denormalized coupling coefficient K_{ij} should vary inversely with the change of the tuning frequency.

Another criterion of achieving constant bandwidth is to maintain the normalized input/output impedance *R*, which is related with the filter bandwidth and group delay at the resonance as shown in (8.2). For a constant absolute bandwidth, the group delay peak $\tau(\omega_0)$ [60] of the input/output reflection coefficient should remain constant across the tuning range.

$$R = \frac{4}{2\pi BW \tau(\omega_0)},$$

$$(8.2)$$

Besides the couplings, the resonator of the tunable filter is desired to have a high unloaded *Q* and a wide tuning range. Further, a smooth variation of frequencies with respect to the actions from the tuning mechanism is usually required from the specification.

8.3 Single-band Tunable Filter Design

A 5-pole Ku-band Chebyshev filter with a synthesized coupling matrix is $R_1 = R_4 = 1.027$, $M_{11} = M_{22} = M_{33} = M_{44} = M_{55} = 0$, $M_{12} = M_{45} = 0.865$, $M_{23} = M_{34} = 0.636$ is selected for demonstrating the concept.

8.3.1 Resonators

The basic building block is the combline resonator with square center conductor shown in Figure 8.3.1(a). The square center post contributes relatively less unloaded Q compared to cylindrical post but benefits the intra-cavity coupling. Chamfers are added at the bottom of the center post improving the unloaded Q from 2900 to 3200 observed by Eigen-mode simulation. In Figure 8.3.1(a), a 2-56 screw penetrating from the cavity lid is used to adjust the CF of the resonator. The relationship between the CF and the penetration depth of the screw is shown in Figure 8.3.1(b). It can be observed that a screw penetration of 0.06" is adequate to realize close to 800 MHz frequency tuning.

(a)	(b)
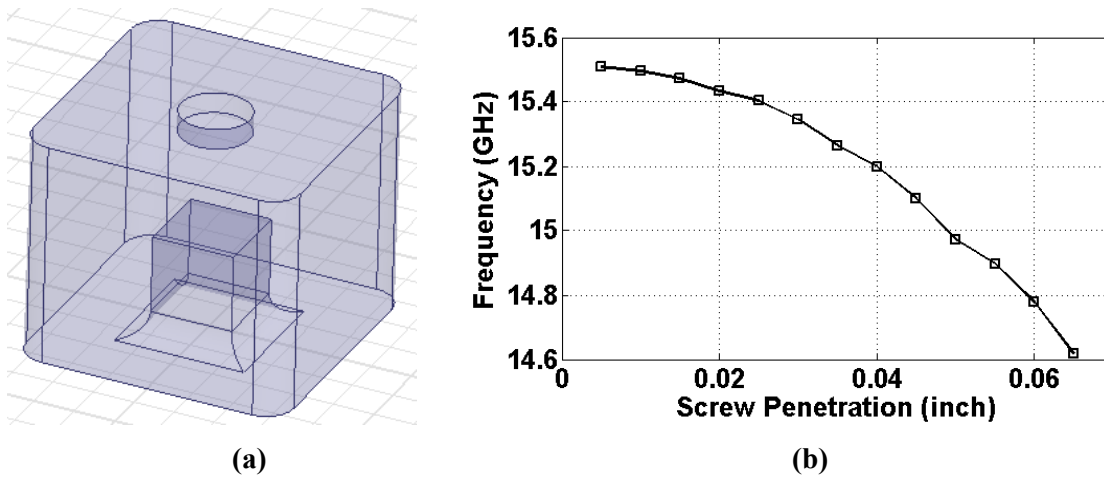
Figure 8.3.1 (a) Layout of combline resonator, and (b) frequency variation over tuning range.

8.3.2 Intra-cavity coupling

Figure 8.3.2(a) illustrates the intra-cavity coupling realization by a vertical iris at the center of the cavity sidewall between the two combline resonators. The coupling between two combline resonators is a combination of inductive and capacitive coupling although the inductive coupling usually dominates with the open-wall iris structure. In the combline resonator, the electric field is more concentrating between the top of the resonator and the tuning screw, while the magnetic field has more focusing near the bottom of the resonators and tuning screws. When the penetration of the tuning screws increases,

the physical gap between center post and the tuning screw gets smaller resulting in an increase of the electric/capacitive coupling. Meanwhile the magnetic coupling also increases because of an increase of overall metallic surfaces. These two coupling variations counter with each other and the overall effect depends on the ratio of height of the center post (P) and height of the cavity housing (H). In this case, the ratio of H and P is around 2. A minimum variation of M_{ij} can be achieved with the change of the tuning screw penetration in two adjacent resonators, as shown in Fig 8.3.2 (b).

<table>
<tr><td>(a)</td><td>(b)</td></tr>
</table>
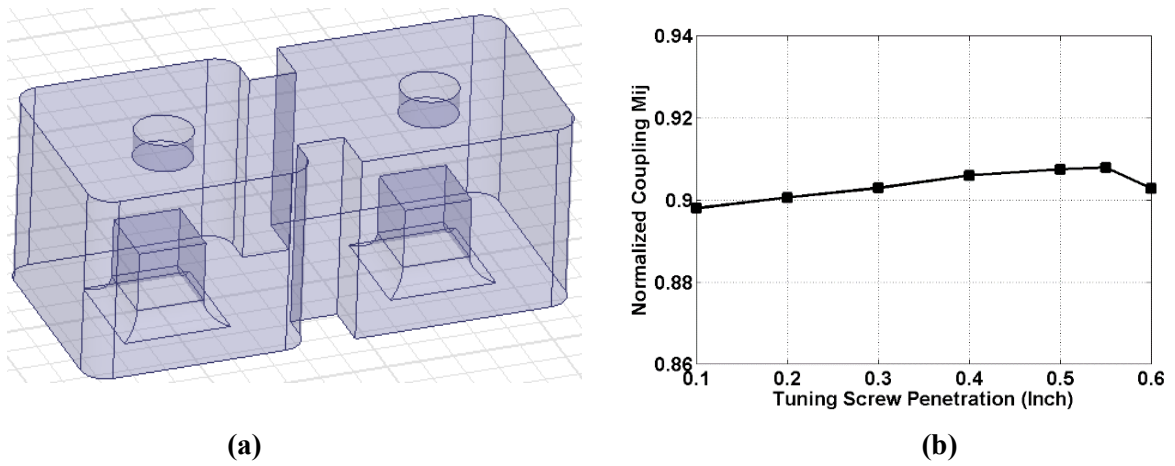
Figure 8.3.2 (a) Sequential coupling, and (b) simulated M$_{ij}$ over tuning range.

8.3.3   Input/output coupling

Based on (8.2), the reflected group delay is required to have a constant peak value during the tuning range to achieve a constant bandwidth. An EM model of the end resonator loaded with a coaxial probe is shown in Figure 8.3.3. Three probe parameters, namely the probe length (L_1), the probe height (H_1), and the distance to the center post (D_1), control the external coupling of the filter. It is observed that the probe length L_1 is critical for maintaining a constant group delay peak over the tuning range. A common approach is to achieve a constant level of group delay peak by only adjusting L_1 , and then adjust other two parameters (H_1 and D_1) to balance the coupling strength. In Figure 3(b), a group of reflected group delay with nearly identical peak of 2ns is achieved with dimensions H_1=0.09", L_1=0.40" and D_1=0.008".
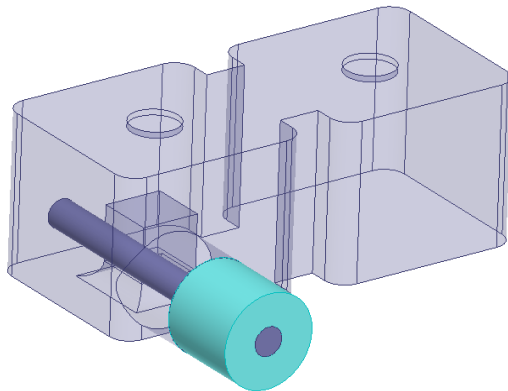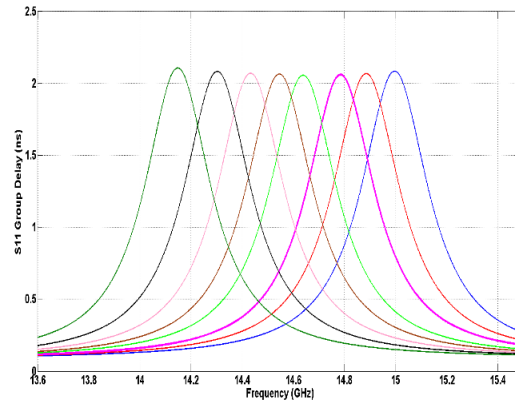
(a)   (b)

Figure 8.3.3 (a) Input coupling, and (b) group delay vs. tuning screw penetration.

8.3.4   Filter Design

Using the above technologies the 5-pole Ku-band filter is designed and swept over the desired frequency range by only adjusting the tuning screw penetrations. The simulated *S*-parameters of the filter over the tuning range are depicted in Figure 8.3.4. The filter achieves a stable RF response over a frequency range of 14 GHz to 14.8 GHz by adjusting penetration of the tuning screws. The *RL* is lower than 18dB, and the bandwidth variation over the tuning range is less than 1%.
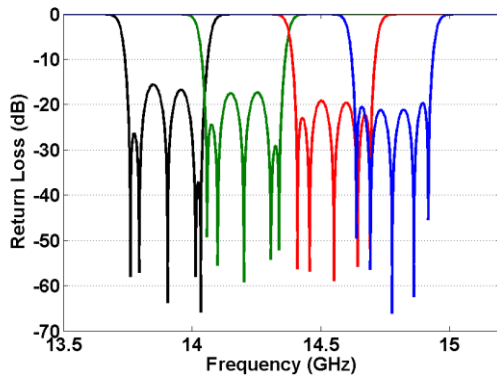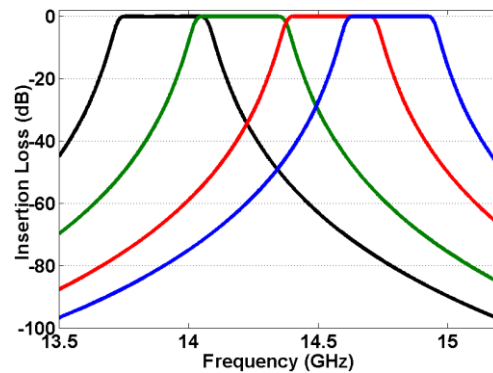
(a)   (b)

Figure 8.3.4 (a) Simulated S_{11} and (b) simulated S_{21} over the tuning range.

122

8.3.5   Tuning Screw Moving Synchronization

The filter response at any tuning stage can be represented by a coupling matrix normalized to the initial stage (e.g. @ the highest frequency corresponding to the minimum penetration of tuning screws). The diagonal parameters M_{ii} of the coupling matrix can be expressed by equation (8.3),

$$M_{ii} = -\frac{1}{FBW} \times (\frac{f_i}{f_0} - \frac{f_0}{f_i}),$$ (8.3)

where f_i and f_0 represent frequencies at current and initial stage respectively, and *FBW* represents the fractional bandwidth at the initial stage. From stage f_0 to stage f_i, all the resonators are shifted by the same electrical amount M_{ii}, which indicates a possibility to realize the tuning by one single element.

Assuming the tuning screw penetration of all resonators at f_i is D_{1i}, D_{2i}, $D_{3i....}$ D_{ni} (n = filter order), and the tuning screw penetration of all resonators at f_j is D_{1j}, D_{2j}, $D_{3j......}$ D_{nj}, the condition for the single-element control is:

$$D_{1j} - D_{1i} = D_{2j} - D_{2i} = D_{3j} - D_{3i} = \cdots \qquad D_{ni}.$$ (8.4)

For each combline resonator, the resonant frequency is mostly determined by the height of the center post H_{nj} and depth of the tuning screw penetration D_{nj}. An Eigen-mode simulation sweeping for different heights of the center post is performed for each resonator, to pursue an identical variation of the tuning screw penetration over any frequency change as stated in (8.4). The procedure can follow three main steps as below:

Step 1: Complete the initial design as per section 8.3.1-8.3.4. The resonators could have the same post height with different screw penetrations, or have the same screw penetration with different post height.

Step 2: Perform Eigen-mode simulation to one reference resonator. It is recommended to choose the center resonator (resonator 3 in this case) reference since most of the filter structures are symmetrical. The variation of the tuning screw penetration (*e.g.* D_{3j} - D_{3i}) versus the variation of the Eigen-mode frequencies (*e.g.* $f_{3j} - f_{3i}$) are recorded as the synchronized target for other resonators.

Step 3: Perform Eigen-mode simulation to other resonators until they are synchronized to the reference resonator. For each of the rest of resonators, the ratio of H_{nj} and D_{nj} is adjusted dynamically until

achieving an identical variation of tuning screw penetration (*i.e.* $D_{nj} - D_{ni} = D_{3j} - D_{3i}$) and frequency change (*i.e.* $f_{nj} - f_{ni} = f_{3j} - f_{3i}$) simultaneously to the reference.

Step 4: Perform a re-simulation as per section III with new resonators, to confirm the coupling parameters unchanged over the tuning range.

The results after the resonator adjustment are shown in Table 8.1, where *Δf* and *ΔD* are the variation of frequency and tuning screw penetration respectively during the tuning stage change. The variations of the screw penetration as well as the frequency shift for all resonators are synchronized with small error. The total tuning frequency range is around 750 MHz.

Table 8.1 Results After the Resonator Adjustment

Items		Resonator 3	Resonator 2,4	Resonators 1,5
Center Post Height (inch)		0.1281	0.1271	0.1243
Stage 1 to Stage 2	Δf_1 (MHz)	32	32	31
	ΔD_1 (inch)	0.008	0.008	0.008
Stage 2 to Stage 3	Δf_2 (MHz)	215	216	215
	ΔD_2 (inch)	0.025	0.025	0.025
Stage 3 to Stage 4	Δf_3 (MHz)	520	520	520
	ΔD_3 (inch)	0.0250	0.0247	0.0253

8.4 Experimental Result of Single-band Tunable Filter

The filter is manufactured with a copper housing. As shown in Figure 8.4.1, the five frequency tuning screws are assembled into a fixed plane mounted with a tuning station, while the filter body is supported by another movable plane of the tuning station. During tuning the supporting plane on the bottom of the filter moves up/down resulting in an increase/decrease of the tuning screw penetration thus shifting the filter. Figure 8.4.2 shows the measured response of the proposed filter. The 300MHz bandwidth is maintained and the *RL* is better than 17 dB over the 700MHz tuning range. The *IL* is higher than expectation due to an imperfect manufacturing of the filter housing especially at the tuning screw area.
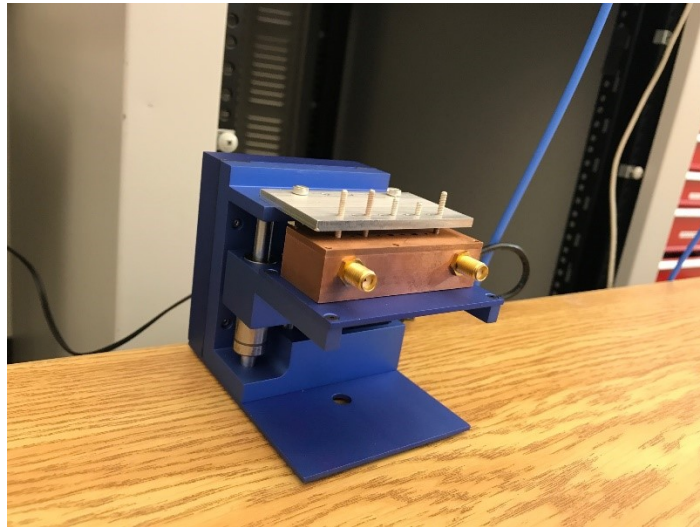
Figure 8.4.1 Setup of the combline filter with tuning station.

(a)

(b)
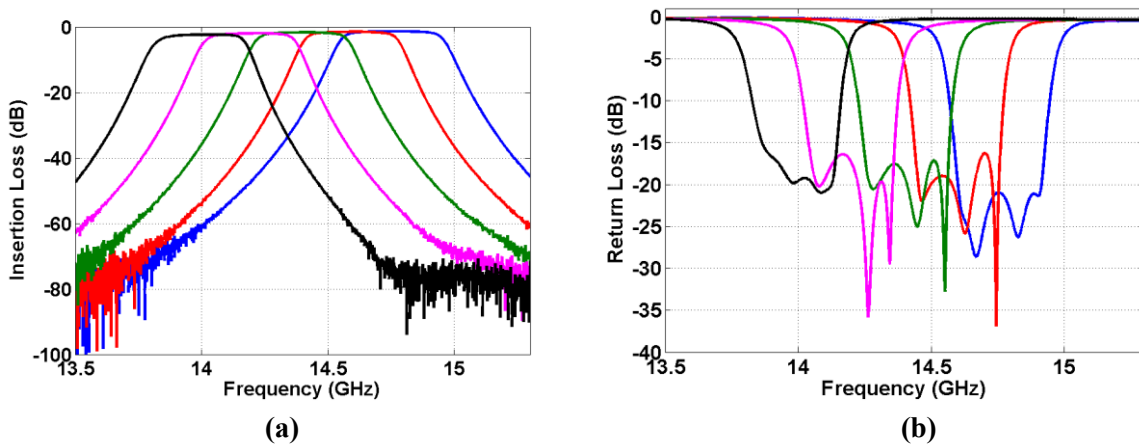
Figure 8.4.2. (a) Measured S21 and (b) measured S11 over the tuning range by adjusting the tuning plate.

8.5   Tunable Multi-band Filter Design

The approach of designing tunable single band filter introduced in previous chapters can be migrated to develop a tunable multi-band filter with a constant bandwidth, however with the following conditions:

1. The multi-band filter need to be representable by a coupling matrix, i.e. not including any non-reciprocal hardware (e.g. circulator) or multiple filters.
2. The multi-band filter need to be realizable by the combline technology with pure iris couplings.
3. The external coupling for the multiple passbands need to be maintained simultaneously.

The three conditions narrow down the multi-band filter topologies to the two structures shown in Figure 8.5.1 (a) and (b). For both cases, there is only single external coupling required for the triple-band design so the condition 3 is satisfied. Meanwhile, both cases are convenient to be represented by coupling matrix and are able to be implemented with combline resonators thus satisfying the conditions 1 and 2. Compared to the configuration in Figure 8.5.1 (b), the configuration in Figure 8.5.1(a) has smaller number of intra-cavity coupling thus benefit the physical realization. The configuration in Figure 8.5.1(a) is chosen in this work to realize a tunable triple-band filter with constant bandwidth.
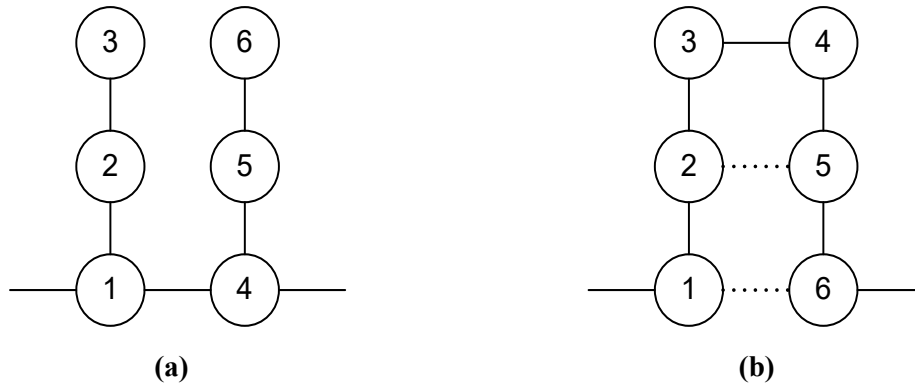
Figure 8.5.1: Triple-band filter realization by inserting in-band transmission zeros (a) bandstop resonator method, and (b) cross-coupling method.

8.5.1   Coupling Matrix

The 9-pole triple-band filter is designed with *CF*s at 2.17, 2.2, and 2.23 GHz and 2 in-band transmission zeros at 2.182 and 2.218 GHz. The block diagram of the triple-band filter is shown in Figure 8.5.1.1. The coupling matrix of the triple-band filter in (8.5) can be synthesized as per the approach in [22].
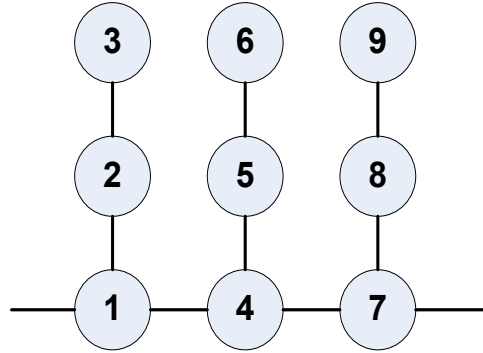
Figure 8.5.1.1: Block diagram of the triple-band filter

$$\begin{pmatrix}
0 & 0.956 & 0 & 0 & 0 & 0 & 0 & 0 & 0 & 0 & 0 \\
0.956 & 0 & 0.457 & 0 & 0.799 & 0 & 0 & 0 & 0 & 0 & 0 \\
0 & 0.457 & 0 & 0.408 & 0 & 0 & 0 & 0 & 0 & 0 & 0 \\
0 & 0 & 0.457 & 0 & 0 & 0 & 0 & 0 & 0 & 0 & 0 \\
0 & 0.799 & 0 & 0 & 0 & 0.457 & 0 & 0.799 & 0 & 0 & 0 \\
0 & 0 & 0 & 0 & 0.457 & 0 & 0.408 & 0 & 0 & 0 & 0 \\
0 & 0 & 0 & 0 & 0 & 0.408 & 0 & 0 & 0 & 0 & 0 \\
0 & 0 & 0 & 0 & 0.799 & 0 & 0 & 0 & 0.457 & 0 & 0.956 \\
0 & 0 & 0 & 0 & 0 & 0 & 0 & 0.457 & 0 & 0.408 & 0 \\
0 & 0 & 0 & 0 & 0 & 0 & 0 & 0 & 0.408 & 0 & 0 \\
0 & 0 & 0 & 0 & 0 & 0 & 0 & 0.956 & 0 & 0 & 0
\end{pmatrix} \quad (8.5)$$

8.5.2   Intra-cavity couplings

Figure 8.5.2.1(a) and (b) illustrate the intra-cavity coupling realization by a vertical iris at the center or at side of the cavity sidewall between the two combline resonators. To maintain a symmetric layout of the filter, the center iris is implemented at the center branch, i.e. between the resonators 4~ 6, while the side iris is implemented at the side branch, i.e. between the resonators 1~3, and 7~9. It is observed that the relative position of the iris has minimum impact on the stability of coupling strength over the tuning range. Figure 8.5.2.2 shows the variation of M_{ij} with the change of the tuning screw penetration.

(a)   (b)
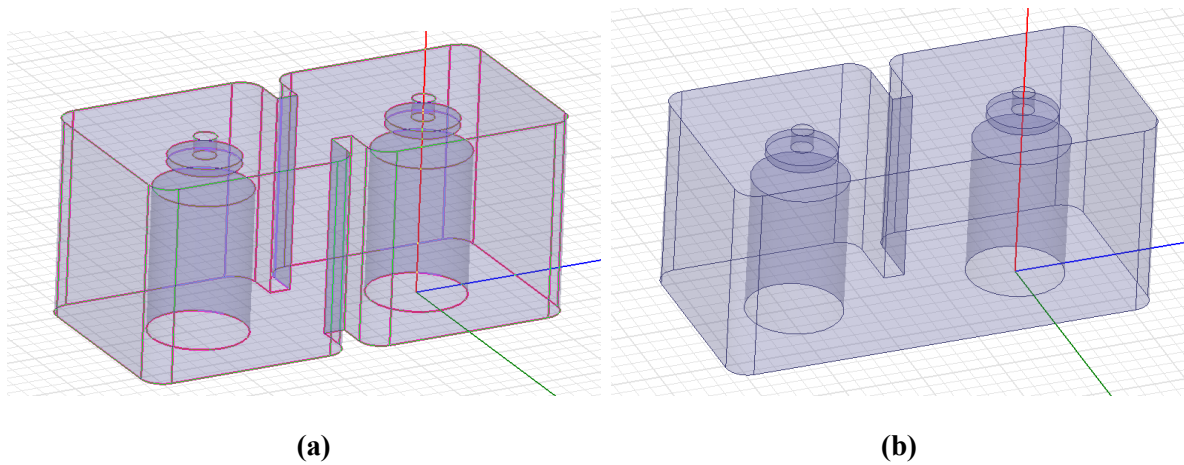
Figure 8.5.2.1: (a) Center iris coupling, and (b) side iris coupling.
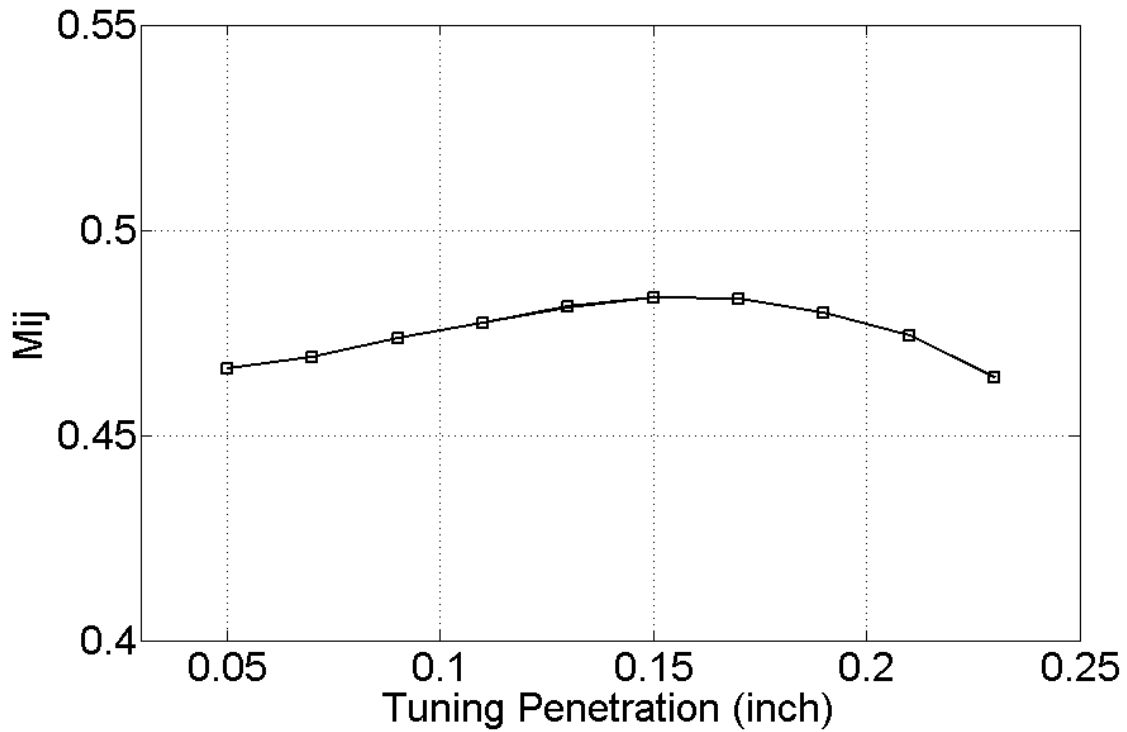
Figure 8.5.2.2: Variation of coupling parameters with the change of tuning screw penetration.

8.5.3   Input / Output couplings

The EM model of the external coupling of the triple-band filter is shown in Figure 8.5.3.1 (a). The external coupling of the filter is controlled by the probe length (L_1), the probe height (H_1), and the distance to the center post (D_1). In this case the probe length L_1 is bended around the first resonator to fit in the cavity while maintaining a constant group delay peak over the tuning range. In Figure 8.5.3.1(b), a group of reflected group delay with nearly identical peak of 21ns is achieved.
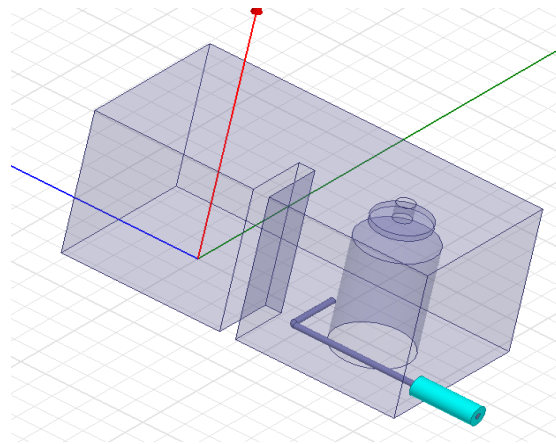
(a)
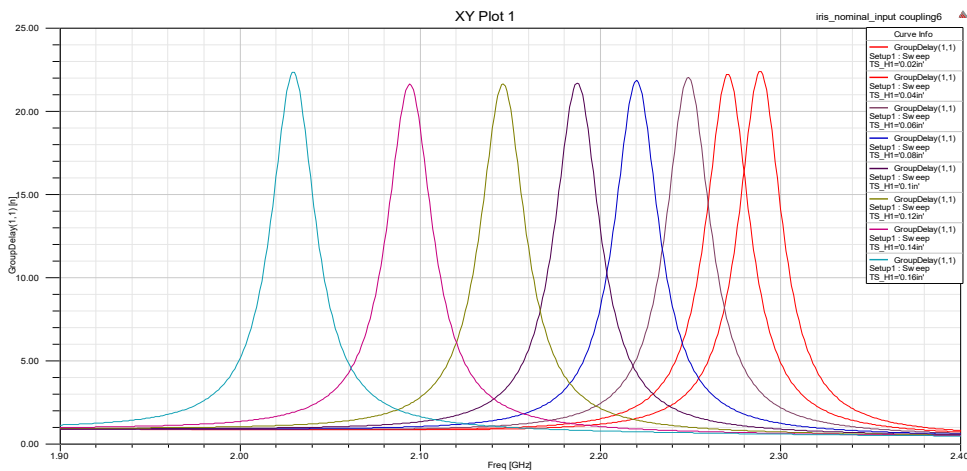
(b)

Figure 8.3.3 (a) External coupling, and (b) reflected group delay vs. tuning screw penetration.

8.5.4 Triple-band Filter Design

The 9-pole C-band triple-band filter is designed and swept over the desired frequency range by only adjusting the tuning screw penetrations. The layout of the tunable triple-band filter is shown in Figure 8.5.4.1. The simulated *S*-parameters of the filter over the tuning range are depicted in Figure 8.5.4.2. The filter achieves a stable RF response over a frequency range of 200 MHz by adjusting penetration of

the tuning screws. The simulated *RL* is lower than 18dB, and the bandwidth variation over the tuning range is less than 1%.
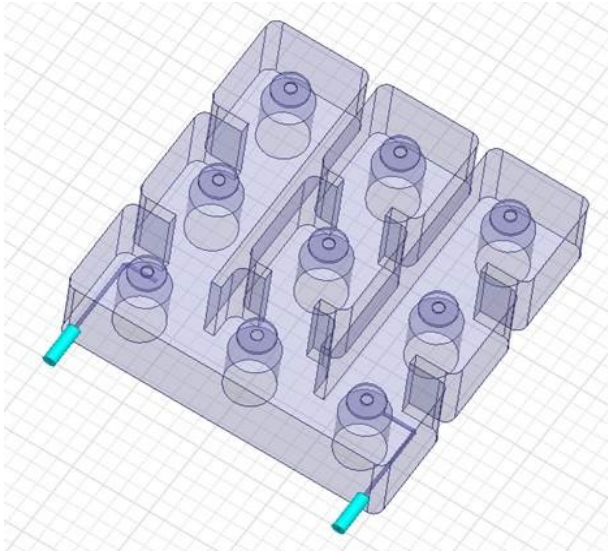
Figure 8.5.4.1. Layout of the C-band triple-band tunable filter.
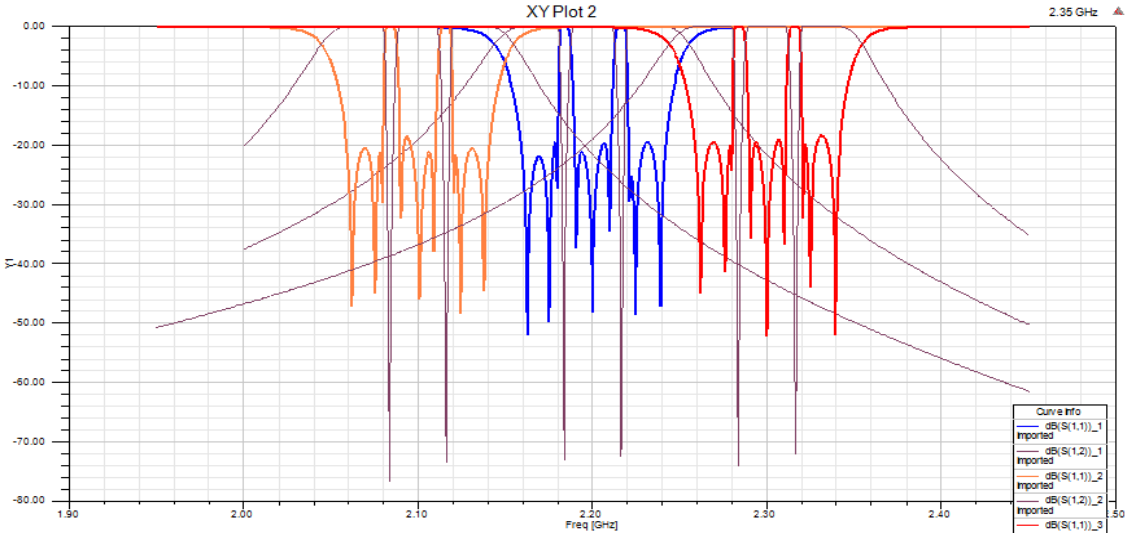
Figure 8.5.4.2. Simulated S-parameters over the tuning range by adjusting the tuning plate.

Similar to the single-band tunable filter, the synchronization process of the tuning screws of the triple-band filter is performed as per section 8.3.5. The summary after the resonator adjustment are shown in Table 8.2, where Δf and ΔD are the variation of frequency and tuning screw penetration respectively during the tuning stage change. The variations of the screw penetration with respect to the frequency shift for all resonators are synchronized with small error, i.e. less than 0.002 inch. The total tuning frequency range is around 200 MHz.

Table 8.2 Results after the Resonator Adjustment (Triple-band)

	Resonator Height (inch)	Stage 1 to Stage 2		Stage 2 to Stage 3	
		Δf_1 (MHz)	ΔD_1 (inch)	Δf_2 (MHz)	ΔD_2 (inch)
Resonator 1, 9	0.925	100	0.056	100	0.036
Resonator 2, 8	0.914	100	0.055	100	0.036
Resonator 3, 7	0.933	100	0.056	100	0.036
Resonator 4	0.822	100	0.054	100	0.036
Resonator 5	0.912	100	0.054	100	0.037
Resonator 6	0.93	100	0.055	100	0.036

8.5.5 Tuning fixture

A special tuning screw fixture is designed to accommodate the movement of the tuning station. As shown in Figure 8.5.5.1 (a) and (b), the fixture has threads on the top half of the post, mounting with the jig plane that attaches with the tuning station in the later step. The non-threaded part of the tuning fixture penetrates through the filter lid so the filter housing can move vertically equivalent to the change of the screw penetration. A further supplement of the tuning fixture is shown in Figure 8.5.5.2, each tuning screw hole on the filter lid is soldered with a copper patch with a number of fingers providing electrical contract to the tuning fixtures. This assembly greatly improves the stability of the filter responses, as well as minimizes the radiation leakage from the tuning screw holes.

45° X .020
Ø.1360 +.0000 -.0005
With threads
No threads
.500
1.000
2X R.015 MAX.
.060
Ø.090
.050

Jig Plane
Filter Lid

(a)   (b)
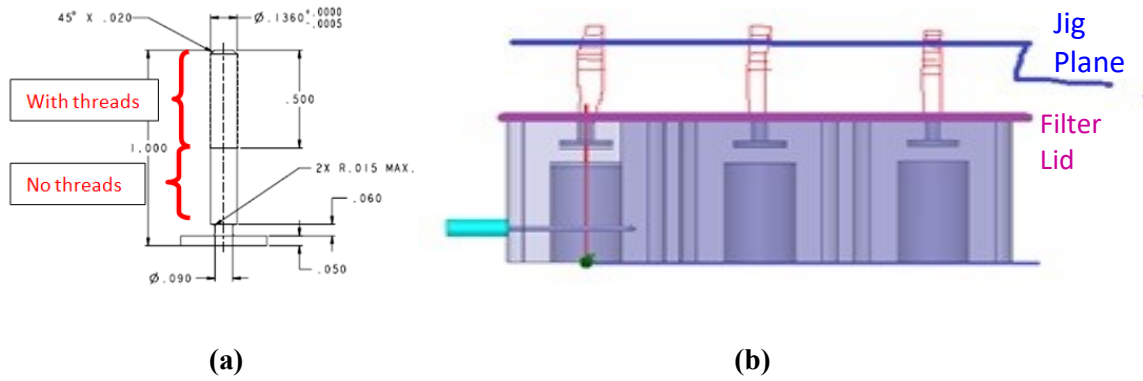
Figure 8.5.5.1 (a) Layout of tuning fixture, and (b) tuning mechanism of the triple-band filter.
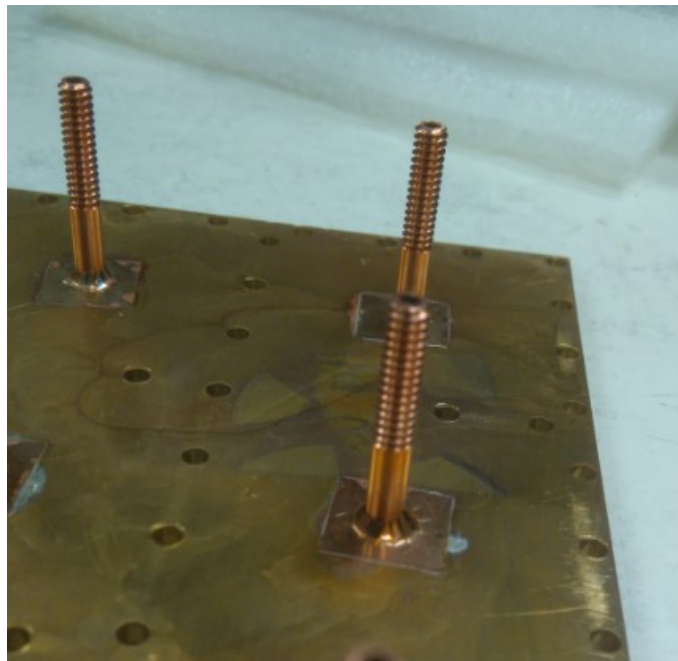
Figure 8.5.5.2 Copper patches with fingers to maintain the electrical contact to the tuning screw.

8.5.6 Experimental Result of Multi-band Tunable Filter

The filter and the jig plane are manufactured with a copper housing. As shown in Figure 8.5.6.1, nine frequency tuning screws are assembled into the jig plane mounted with a tuning station. The filter housing is supported by another movable plane of the tuning station. During tuning the supporting plane on the bottom of the filter moves up/down resulting in an increase/decrease of the tuning screw penetration thus shifting the filter. Figure 8.5.6.2 shows the measured responses at different frequency stages of the proposed filter. A tuning range over 170MHz is maintained with the *RL* better than 15 dB. The *IL* is higher than expectation due to an imperfect manufacturing of the filter housing especially at the tuning screw area.
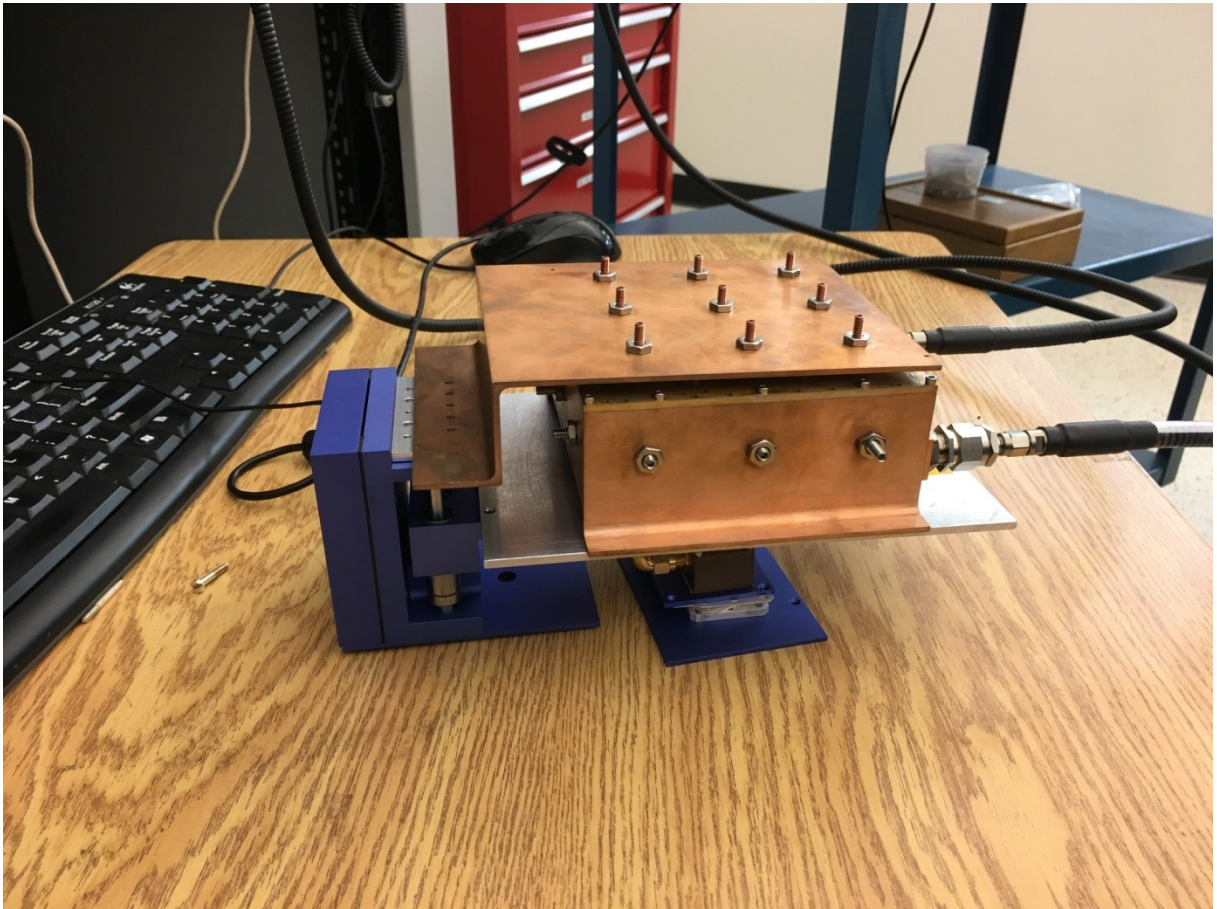
Figure 8.5.6.1 Setup of the combline triple-band filter with tuning station.
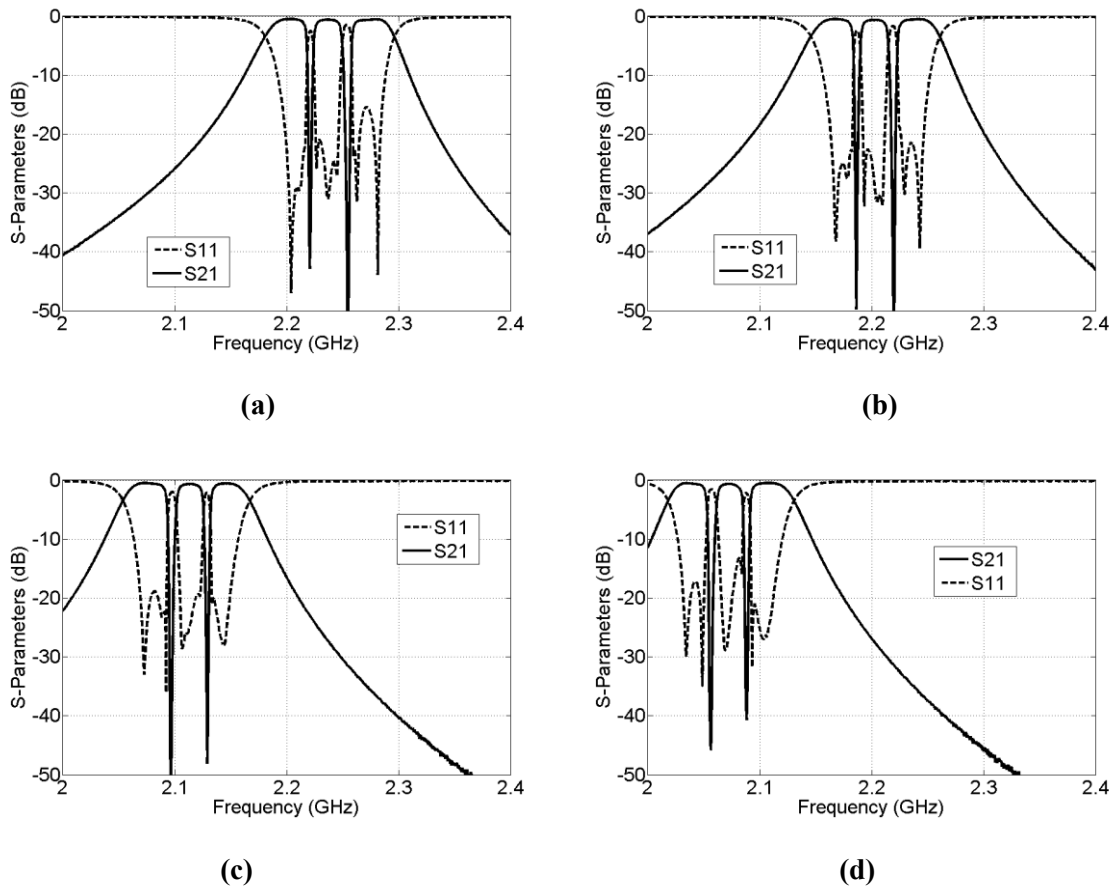
Figure 8.5.6.2 Different tuning stages of the triple-band filter (a) *CF* **2.24 GHz, (b)** *CF* **2.20 GHz, (c)** *CF* **2.11 GHz, and (d) 2.07 GHz**

8.6   Conclusion

Tunable single-band and triple-band filters using combline resonators employing a single tuning element have been presented. A detailed design approach for filter parameters has been presented to achieve a constant bandwidth over the tuning range by a single element control. The concept has been experimentally validated by a 5-pole Ku-band single-band and 9-pole C-band triple-band design. The single and triple band design achieved 700MHz and 170MHz tuning range with constant *BW* respectively.

Chapter 9
Conclusions

9.1   Contributions

In this dissertation, we focused on theoretical and practical aspects of cavity-based multi-band bandpass filters and multiplexers. The major contributions of this research are outlined as follows,

- After reviewing a number of different approaches to realize cavity-based multi-band filter, the approach of using multi-mode resonators has been chosen for all the proposed designs considered in this thesis because of its unbeaten advantages of size saving while not sacrificing the unloaded Q. To facilitate the design of such class of the multi-band filter, a systematic and practical approach to synthesis the multi-band coupling matrix based on the traditional synthesis approach of single-band filter has been presented in chapter 3 [77][80].

- A dual-band filter using elliptical dual-mode resonators is presented in chapter 4 [79]. Each passband of the dual-band filter was controlled by a dedicated TE_{11m} polarization and represented by an inline direct-coupled set of resonators, thereby allowing a simple design process. The detailed design approach for each parameter of the proposed structure was discussed and verified by a 16-pole Ku-band dual-band filter. The dual-band structure can be easily converted to a diplexer structure by modifying the output ports at the last resonators.

- To demonstrate dual-band filters with transmission zeros for each of the passbands, a new dual-band design based on the proposed dual-trisection module has been presented in chapter 5 [73][79]. The unique dual tri-section structure consists of dual-band and single-band rectangular cavities that result in dual-band filter or diplexers of compact size, high Q, multiple transmission zeros and improved spurious response. All features have been experimentally validated by a 4th order Ku-band diplexer. Further, a novel folded configuration of dual-band bandpass filters based on dual-mode elliptical cavity resonators has also been presented [76][81]. The dual-

quadruplet module offers a reduced footprint compared to many previous reported structures and generates a pair of transmission zeros for each of the passband. The first implementation is a side coupled design. The design has a very compact layout and can be realized with pure inductive coupling irises. The second implementation is a combination of side-coupled and end-coupled design aiming for wider bandwidth applications. Approaches to improve the out-of-band spurious response have been discussed and considerable improvement has been observed from the EM simulation. The design concept has been validated by two 8-pole C-band prototypes. The proposed filter configuration can be easily extended to higher order filters while still maintain a compact size.

- The triple-band filters have been realized by three different high-Q cavity resonator structures in chapter 6 and 7 [74][75][77][78][80]. Each cavity resonator employs triple-modes with resonant frequencies associated with the three passbands. Such approach provides the most significant size and mass saving while maintaining a high Q. The first design was an elliptical-cavity triple-band filter with an in-line configuration. Each passband of the filter was controlled by a dedicated polarization and represented by an inline direct-coupled set of resonators. The second design was a rectangular-cavity triple-band filter with a folded configuration. Compared to elliptical cavity design, the three modes in the rectangular resonator have higher degree of orthogonality making it easily to independently control the inter-resonator couplings of three modes. The folded configuration overcomes a number of drawbacks from the elliptical in-line design including an improved tunability and ease of assembly. The last design was a triple-band filter design based on dielectric resonators. The unique dielectric resonator structure results in triple-band filters having a very compact size, high Q, and stable thermal response. The detailed design approach for each parameter of the three proposed triple-band structures was discussed and all features have been validated through the realization and measurement of filter prototypes.

- A tunable single-band filter using combline resonators employing a single tuning element has been presented in chapter 8. A detailed design approach for filter parameters has been presented to achieve a constant bandwidth over the tuning range by a single element control. The approach is then extended to realize a tunable triple-band filter. The triple-band filter achieved over 170MHz tuning range with constant BW. The concept has been experimentally validated by a 5-pole Ku-band and 9-pole C-band design.

9.2   Future work

This dissertation can be followed in different directions, some of which are highlighted as below.

- **Triple-band filter with quasi-elliptic responses**. So far only chebyshev function has been realized in the triple-band filter. An interesting but challenging research could be to invent a cross-coupling mechanism for the triple-band cavity filter. The mechanism requires to have sufficient resolution to identify the relatively small cross-couplings of three individual paths from the inherent mutual-coupling among the triple resonant modes.

- **Individually tunable multi-band filter with constant BW**. So far the presented tunable multi-band filter shift all the passbands at the same time and with the same drifting frequency. It could be interesting to investigate other prototypes of multi-band filter (e.g. multi-mode resonator based), to realize individual controlling of each passband.

References

[1] S. Holme, "Multiple passband filters for satellite applications," *Proc. 20ᵗʰ AIAA Ino. Commun. Satellite Syst. Conf. Exhibit*, 2002.

[2] O. Vidal, G. Verelst, J. Lacan, E. Alberty, J. Radzik, M. Bousquet, "Next generation high throughput satellite system", *Proc. 1ˢᵗ. AESS Euro. Conf. on Satellite Telecommun.*, 2012.

[3] G. Macchiarella and S. Tamiazzo, "Design techniques for dual-passband filters," *IEEE Trans. Microwave Theory Techn.*, vol. 53, no. 11, pp. 3265–3271, Nov. 2005.

[4] R. Zhang, and R. R. Mansour, "Dual-band dielectric-resonator filters," *IEEE Trans. Microw. Theory & Tech.*, vol. 57, no. 7, pp. 1760-1766, Jul. 2009.

[5] S. Amari, and M. Bekheit "A new class of dual-mode dual-band waveguide filters," *IEEE Trans. Microw. Theory Techn.*, vol. 56, no. 8, pp. 1938–1944, Aug. 2008.

[6] P. Lenoir, S. Bila, F. Seyfert, D. Baillargeat, and S. Verdeyme, "Synthesis and design of asymmetrical dual-band bandpass filters based on equivalent network simplification," *IEEE Trans. Microw. Theory Techn.*, vol. 54, no. 7, pp. 3090–3097, Jul. 2006.

[7] M. Mokhtaari, J. Bornemann, K. Rambabu, and S. Amari, "Coupling matrix design of dual and triple passband filters," *IEEE Trans. Microw. Theory Techn.*, vol. 55, no. 11, pp. 3940–3946, Nov. 2006.

[8] B. Chan, T. Shen, and R. Wu, "Design of tri-band filters with improved band allocation," *IEEE Trans. Microw. Theory & Techn.*, vol. 57, no. 7, pp. 1790-1797, Jul. 2009.

[9] X. Chen, K. Wu, and Z. Li, "Dual-band and triple-band substrate integrated waveguide filters with chebyshev and quasi-elliptical responses," *IEEE Trans. Microw. Theory & Techn.*, vol. 55, no. 12, pp. 2569-2578, Dec. 2007.

[10] A. A. Abidi, "The path to the Software-Defined Radio" Receiver," *IEEE Journal of Solid-State Circuits*, vol. 42, no. 5, pp. 954-966, 2007.

[11] J. Hwang, M. Lee, C. Jeong, and C. Yoo, "Active-RC channel selection filter tunable from 6 kHz to 18 MHz for software-defined radio," in *Proc. IEEE ISCAS*, 2005, pp. 4803–4806.

[12] A. Mallet, A. Anakabe, J. Sombrin, and R. Rodriguez, "Multiport amplifier-based architecture versus classical architecture for space telecommunication payloads," *IEEE Trans. Microw. Theory Techn.*, vol. 54, no. 12, pp. 4353–4361, Dec. 2006.

[13] E. Pistono, M. Robert, L. Duvillaret, J. Duchamp, A. Vilcot, and P. Ferrari, "Compact fixed and tune-all bandpass filters based on coupled slow-wave resonators," *IEEE Trans. Microwave Theory Tech.*, vol. 54, no. 6, pp. 2790–2799, Jun. 2006.

[14] Y. Liu, A. Borgioli, A. S. Nagra, and R. A. York, "Distributed MEMS transmission lines for tunable filter applications," *Int. Journal. RF Microw. Comput.-Aided Eng.*, vol. 11, no. 5, pp. 254–260, Sep. 2001.

[15] A. Abbaspour-Tamijani, L. Dussopt, and G. M. Rebeiz, "A millimeterwave tunable filter using MEMS capacitors," in *Proc. 32nd Eur. Microw. Conf.*, Milan, Italy, Sep. 2002, pp. 813–815.

[16] D. Mercier, J.-C. Orlianges, T. Delage, C. Champeaux, A. Catherinot, D. Cros, and P. Blondy, "Millimeter-wave tune-all bandpass filters," *IEEE Trans. Microwave Theory Tech.*, vol. 52, no. 4, pp. 1175–1181, Apr. 2004.

[17] Raytheon Co., "Signal tracking electronically tunable filter," U.S. Patent 5019792A, 1989.

[18] M. Yu, B. Yassini, B. Keats, and Y. Wang, "The sound the air makes: high-performance tunable filters based on air-cavity resonators," *IEEE. Microwave Magazine*, vol. 15, issue 5, pp. 83–93, 2014.

[19] C. Arnold, J. Parlebas, and T. Zwick, "Reconfigurable waveguide filter with variable bandwidth and center frequency," *IEEE Transactions on Microwave Theory and Techniques*, vol. 62, no. 8, 2014, pp. 1663-1670.

[20] L.-C. Tsai and C.-W. Hsue, "Dual-band bandpass filters using equal-length coupled-serial-shunted lines and Z-transform technique," *IEEE Trans. Microwave Theory Tech.*, vol. 52, no. 4, pp. 1111–1117, Apr. 2006.

[21] Airbus Defense and Space Ltd., "Multi-band filter," U.S. Patent 20110254641A1, 2011.

[22] H. Di, B. Wu, X. Lai, and C-H. Liang, "Synthesis of cross-coupled triple-passband filters based on frequency transformation," *IEEE Microw. and Wireless Comp. Letter.*, vol. 20, no. 8, pp. 432–434, Aug. 2010.

[23] R. H. Geschke, B. Jokanovic, and P. Meyer, "Filter Parameter Extraction for triple-band composite split-ring resonators and filters," *IEEE Trans. Microwave Theory Tech.*, vol. 59, no. 6, pp. 1500–1508, Jun. 2011.

[24] J. Ruiz-Cruz, M. M. Fahmi, and R. R. Mansour, "Triple-conductor combline resonators for dual-band filters with enhanced guard-band selectivity," *IEEE Trans. Microwave Theory & Tech.*, vol. 60, no. 12, pp. 3969-3979, Dec. 2012.

[25] U. Naeem, S. Bila, M. Thevenot, T. Monediere, and S. Verdeyme, "A Dual-band bandpass filter with widely separated passbands," *IEEE Trans. Microwave Theory & Tech.*, vol. 62, no. 3, pp. 450-456, Mar. 2014.

[26] K. Entesari and G. M. Rebeiz, "A 12 to18-GHz Three-Pole RF MEMS Tunable Filter," *IEEE Trans. Microwave Theory & Tech.*, vol. 53, , Ed., 2005, pp. 2566-2571.

[27] K. Entesari and K. Obeidat, "A 25 -75-MHz RF MEMS Tunable Filter," *IEEE Trans. Microwave Theory & Tech.*, vol. 55, 2007, pp. 2399-2405.

[28] L. Dussopt and G. M. Rebeiz, "Intermodulation distortion and power handling in RF MEMS switches, varactors, and tunable filters," *IEEE Trans. Microwave Theory & Tech.*, vol. 51, 2003, pp. 1247-1256.

[29] C. L. Goldsmith, Z. Yao, S. Eshelman, and D. Denniston, "Performance of low-loss RF MEMS capacitive switches," *IEEE Microwave and Guided Wave Letters*, vol. 8, pp. 269-271, 1998.

[30] K. Entesari and G. M. Rebeiz, "A differential 4-bit 6.5-10-GHz RF MEMS tunable filter," *IEEE Trans. Microwave Theory & Tech.*, vol. 53, 2005, pp. 1103-1110.

[31] S. J. Park, K. Y. Lee, and G. M. Rebeiz, "Low-Loss 5.15 - 5.70-GHz RF MEMS Switchable Filter for Wireless LAN Applications," *IEEE Trans. Microwave Theory & Tech.*, vol. 54, 2006, pp. 3931-3939.

[32] A. Abbaspour-Tamijani, L. Dussopt, and G. M. Rebeiz, "Miniature and tunable filters using MEMS capacitors," *IEEE Trans. Microwave Theory & Tech.*, vol. 51, 2003, pp. 1878-1885.

[33] L. Sanghyo, K. Jong-Man, K. Jung-Mu, K. Yong-Kweon, and K. Youngwoo, "Millimeter-wave MEMS tunable low pass filter with reconfigurable series inductors and capacitive shunt switches," *IEEE Trans. Microwave Theory & Tech.*, vol. 15, 2005, pp. 691-693.

[34] D. Peroulis, S. Pacheco, K. Sarabandi, and L. P. B. Katehi, "Tunable lumped components with applications to reconfigurable MEMS filters," in *Microwave Symposium Digest, 2001 IEEE MTT-S International*, vol. 1, 2001, pp. 341-344.

[35] K. Hong-Teuk, P. Jae-Hyoung, K. Yong-Kweon, and K. Youngwoo, "Low-loss and compact V-band MEMS-based analog tunable bandpass filters," in *Microwave and Wireless Components Letters, IEEE*, vol. 12, 2002, pp. 432-434.

[36] W. D. Yan and R. R. Mansour, "Compact Tunable Bandstop Filter Integrated with Large Deflected Actuators," in *Microwave Symposium, 2007. IEEE/MTT-S International*, 2007, pp. 1611-1614.

[37] S. Firas and L. Liwei, "A Plastic W-Band MEMS Tunable Filter," in *Microwave Symposium Digest, 2006. IEEE MTT-S International*, 2006, pp. 136-139.

[38] W. D. Yan and R. R. Mansour, "Tunable Dielectric Resonator Bandpass Filter With Embedded MEMS Tuning Elements," *IEEE Trans. Microwave Theory & Tech.*, vol. 55, 2007, pp. 154-160.

[39] F. Huang, S. Fouladi, R.R. Mansour, "High-Q Tunable Dielectric Resonator Filters Using MEMS Technology", *IEEE Transactions on Microwave Theory and Techniques*, vol. 59, pp.3401-3409, 2011

[40] K. Byung-Wook and Y. Sang-Won, "Varactor-tuned combline bandpass filter using step-impedance microstrip lines," in *IEEE Transactions on Microwave Theory and Techniques*, vol. 52, 2004, pp. 1279-1283.

[41] M. Makimoto and M. Sagawa, "Varactor Tuned Bandpass Filters Using Microstrip-Line Ring Resonators," in *Microwave Symposium Digest, MTT-S International*, vol. 86, 1986, pp. 411-414.

[42] A. R. Brown and G. M. Rebeiz, "A varactor-tuned RF filter," *IEEE Transactions on Microwave Theory and Techniques*, vol. 48, 2000, pp. 1157-1160.

[43] Y. H. Shu, J. A. Navarro, and K. Chang, "Electronically switchable and tunable coplanar waveguide-slotline band-pass filters," *IEEE Transactions on Microwave Theory and Techniques*, vol. 39, 1991, pp. 548-554.

[44] X. Jian, L. Xiao-Peng, and K. Shamsaifar, "Full wave analysis and design of RF tunable filters," in *Microwave Symposium Digest, 2001 IEEE MTT-S International*, vol. 3, 2001, pp. 1449-1452, vol.3.

[45] I. C. Hunter and J. D. Rhodes, "Electronically tunable microwave bandstop filters," *IEEE Transactions on Microwave Theory and Techniques*, vol. MTT-30, pp. 1361-7, 1982.

[46] R. Zhang and R. R. Mansour, "Novel tunable lowpass filters using folded slots etched in the ground plane," presented at *2005 IEEE MTT-S International Microwave Symposium*, Long Beach, CA, United States, 2005.

[47] B. S. Virdee, "Effective technique for electronically tuning a dielectric resonator," in *Electronics Letters*, vol. 33, 1997, pp. 301-302.

[48] B. S. Virdee, A. S. Virdee, and L. A. Trinogga, "Novel invasive electronic tuning of dielectric resonators," in *Microwave Symposium Digest, 2003 IEEE MTT-S International*, vol. 1, 2003, pp. 51-54 vol.1.

[49] J. Krupka, A. Abramowicz, and K. Derzakowski, "Tunable dielectric resonator bandpass filter," presented at *MIKON-2000*, Warsaw, Poland, 2000.

[50] J. Krupka, A. Abramowicz, and K. Derzakowski, "Magnetically tunable filters for cellular communication terminals," *IEEE Transactions on Microwave Theory and Techniques*, vol. 54, 2006, pp. 2329-2335.

[51] O. Acar, T. Johansen, and V. Zhurbenko, "A high-power low-loss continuously tunable bandpass filter with transversely biased ferrite-loaded coaxial resonators," *IEEE Transactions on Microwave Theory and Techniques*, vol. 63, no. 10, 2015, pp. 3425-3432.

[52] G. L. Matthaei, L. Young, and E. M. T. Jones, *Microwave Filters, Impedance-Matching Networks, and Coupling Structures*. Norwood, MA: Artech House, INC, 1980.

[53] S. W. Chen, K. A. Zaki, and R. G. West, "Tunable, temperature-compensated dielectric resonators and filters," *IEEE Transactions on Microwave Theory and Techniques*, vol. 38, 1990, pp. 1046-1052.

[54] J. Uher and W. J. R. Hoefer, "Tunable microwave and millimeter-wave band-pass filters," *IEEE Transactions on Microwave Theory and Techniques*, vol. 39, 1991, pp. 643-653.

[55] S. Tao, K. A. Zaki, and W. Chi, "Tunable dielectric resonators with dielectric tuning disks," *IEEE Transactions on Microwave Theory and Techniques*, vol. 48, 2000, pp. 2439-2445.

[56] W. Chi and W. D. Blair, "Tunable high-Q dielectric loaded resonator and filter," Piscataway, NJ, USA, 2002

[57] C. Arnold, J. Parlebas, and T. Zwick, "Reconfigurable waveguide filter with variable bandwidth and center frequency," *IEEE Transactions on Microwave Theory and Techniques*, vol. 62, no. 8, 2014, pp. 1663-1670.

[58] G. Basavarajappa and R. R. Mansour, "Design methodology of a tunable waveguide filter with a constant absolute bandwidth using a single tuning element," *IEEE Trans. Microw. Theory Techn.*, vol. 66, pp. 5632–5639, 2018.

[59] S. Wong, F. Deng, Y. Wu, J. Lin, L. Zhu, Q. Chu and Y. Yang, "Individually frequency tunable dual- and triple-band filters in a single cavity," *IEEE Access*, vol. 5, pp. 11615–11625, 2017.

[60] R. J. Cameron, C. M. Kudsia, R. R. Mansour, *Microwave Filters for Communication Systems*, New Jersey: Wiley, 2007.

[61] J. B. Thomas, "Cross-coupling in coaxial cavity filters – a tutorial overview," *IEEE Trans. Microw. Theory & Techn.*, vol. 51, no. 4, pp. 1368-1376, Apr. 2003

[62] A. E. Atia and A. E. Williams, "Narrow bandpass waveguide filters," IEEE Trans. Microwave Theory Techn., vol. 20, pp. 258–265, Apr. 1972.

[63] X.-P. Liang, K. A. Zaki, and A. E. Atia, "Dual mode coupling by square corner cut in resonators and filters," *IEEE Trans. Microwave Theory Tech*., vol. 40, pp. 2294–2302, Dec. 1992.

[64] L. Accatino, G. Bertin, and M. Mongiardo, "A four-pole dual mode elliptic filter realized in circular cavity without screws," *IEEE Trans. Microwave Theory Tech*., vol. 44, pp. 2680–2687, Dec. 1996.

[65] L. Accatino, G. Bertin, and M. Mongiardo, "Elliptical cavity resonators for dual-mode narrow-band filters," *IEEE Trans. Microw. Theory Techn*., vol. 45, no. 12, pp. 2393–2401, Dec. 1997.

[66] U. Rosenberg, "Multiplexing and double band filtering with common multi-mode cavities," *IEEE Trans. Microw. Theory & Techn.,* vol. 38, no. 12, pp. 1862-1871, Dec. 1990.

[67] B. Yassini, M. Yu, and B. Keats, "A Ka-band fully tunable cavity filter," *IEEE Trans. Microw. Theory & Techn.,* vol. 60, no. 12, pp. 4000-4012, Dec. 2012.

[68] S. Nam, B. Lee, C. Kwak, and J. Lee, "A New Class of K-Band High-Q Frequency-Tunable Circular Cavity Filter," *IEEE Trans. Microw. Theory & Techn.,* vol. 66, no. 3, pp. 1228-1238, Mar. 2018.

[69] M. Yu, D. Smith, A. Sivadas and W. Fitzpatrick, "A dual mode filter with trifurcated iris and reduced footprint," 2002 *IEEE MTT-S Int. Microwave Symp*. Dig., pp. 1457-1460, June 2002.

[70] M. Meng and K. Wu, "An analytical approach to computer-aided diagnosis and tuning of lossy microwave coupled resonator filters," *IEEE Trans. Microw. Theory Techn*., vol. 57, no. 12, pp. 3188–3195, Dec. 2009.

[71] G. Macchiarella and D. Traina, "A formulation of the Cauchy method suitable for the synthesis of lossless circuit models of microwave filters from lossy measurements," *IEEE Microw. Wireless Compon. Lett.,* vol. 16, no. 5, pp. 243–245, May 2006.

[72] B. Yassini, M. Yu, D. Smith and S. Kellett, "A Ku-Band High-Q Tunable Filter With Stable Tuning Response," *IEEE Trans. Microw. Theory Techn*., vol. 57, pp. 2948-2957, 2009.

List of Publications constituting the Ph.D. thesis:

A. Conference Papers

[73] L. Zhu, R. R. Mansour, and M. Yu, "A compact waveguide diplexer employing dual-band resonators," 2014 *IEEE MTT-S Int. Microwave Symp*. Dig., pp. 1-4, June 2014.

[74] L. Zhu, R. R. Mansour, and M. Yu, "Compact triple-band bandpass filters using rectangular waveguide resonators," 2016 *IEEE MTT-S Int. Microwave Symp*. Dig., May 2016.

[75] L. Zhu, R. R. Mansour, and M. Yu, "Triple-band dielectric resonator bandpass filter," 2017 *IEEE MTT-S Int. Microwave Symp*. Dig., June 2017.

[76] L. Zhu, R. R. Mansour, and M. Yu, "A compact quasi-elliptic waveguide dual-band filter," 2019 *IEEE MTT-S Int. Microwave Symp*. Dig., June 2019.

B. Invited Workshop

[77] L. Zhu, R. R. Mansour, and M. Yu, "Synthesis and Design of Multi-band Filters Employing Multi-mode Resonators", *IEEE MTT-S Int. Microwave Symp*., *Workshop* on "Advanced synthesis techniques for reduced filtering networks", June, 2018

C. Patent

[78] L. Zhu, R. R. Mansour, and M. Yu., "Multi-band bandpass filter," U.S. Patent 10205209B2, 2016.

D. Journal Papers

[79] L. Zhu, R. R. Mansour, and M. Yu, "Compact waveguide dual-band filters and diplexers," *IEEE Trans. Microw. Theory Techn*., vol. 65, no. 5, pp. 1525–1533, May. 2017.

[80] L. Zhu, R. R. Mansour, and M. Yu, "Triple-band cavity bandpass filters," *IEEE Trans. Microw. Theory Techn*., vol. 66, no. 9, pp. 4057–4069, Sep. 2018.

[81] L. Zhu, R. R. Mansour, and M. Yu, "Quasi-elliptic waveguide dual-band filter," *IEEE Trans. Microw. Theory Techn*., submitted and under review.